GRADIENT MICROSTRUCTURE CONTROL IN DEFORMATION-BASED SURFACE GENERATION

A Dissertation
Presented to
The Academic Faculty

by

Zhiyu Wang

In Partial Fulfillment
of the Requirements for the Degree
Doctor of Philosophy in the
George W. Woodruff School of Mechanical Engineering

Georgia Institute of Technology
August 2018

GRADIENT MICROSTRUCTURE CONTROL IN DEFORMATION-BASED SURFACE GENERATION

Approved by:

Dr. Christopher Saldana, Advisor
School of Mechanical Engineering
Georgia Institute of Technology

Dr. Thomas Kurfess
School of Mechanical Engineering
Georgia Institute of Technology

Dr. Shreyes Melkote
School of Mechanical Engineering
Georgia Institute of Technology

Dr. Ting Zhu
School of Mechanical Engineering
Georgia Institute of Technology

Dr. Tejas Murthy
Department of Civil Engineering
Indian Institute of Science

Date Approved: August 2018

This thesis is dedicated to my grandfather.

ACKNOWLEDGEMENTS

I would like to express my deepest gratitude and thanks to my advisor, Prof. Dr. Christopher Saldana, for his guidance, advice and patience throughout graduate school. I am privileged to work on this project in his research group. I am indebted to Professor Dr. Tejas Murthy for providing valuable suggestions and seeing me through many technical challenges in my research. Special thanks go to Professors Dr. Shreyes Melkote, Dr. Thomas Kurfess, and Dr. Ting Zhu for serving on my committee. I would also like to acknowledge NSF CMMI 1464853 and 1254818, US Army Research Office W911NF-14-1-0566, and Third Wave Systems DE-EE0005762 for support of this work.

I also want to thank my present and past colleagues: Saurabh, Haipeng, Max, John, Joon, Ryan, Vinh, Patxi, Austin, Rahul, Bhanu for providing immense help for research and life both inside and outside the lab. I am grateful to Steven, Louis, and Nathan in Montgomery Machining Mall for helping me fabricate the experimental setups. I also appreciate the help from staff in Institute for Electronics and Nanotechnology (IEN) for teaching and training me to produce high-quality characterization results.

Most importantly, my most heartfelt thanks go to my parents and grandparents for their blind and unconditional support. In addition, I want to dedicate this work specifically to my fiancé, Tina, for putting up with countless five-hour flights and my frustration with grace beyond measure. Their love, support, and encouragement helped me get through this agonizing period in the most positive way.

TABLE OF CONTENTS

LIST OF TABLES

LIST OF FIGURES

changes. Inset on right shows effect of strain path changes on accelerated microstructure evolution. These zones are identified using the dashed line.

SUMMARY

Fabrication of surface gradient microstructure by surface severe plastic deformation (S^2PD) has been shown as an effective process to enhance functional performance and extend the service life of engineering components. The imposed gradient in strain results in a graded nanostructured material with an average grain size of < 100 nm in the topmost surface layer, while the interior region remains in a state similar to the undeformed bulk. Materials with these graded structures exhibit desirable properties including increased resistance to scratching, fatigue, and corrosion, without sacrificing overall ductility. Various mechanical surface modification (MSM) processes have been studied to fabricate components with gradient microstructure over the past decade. Main classes of MSM-based processes include indentation-type methods which involve impressions made on a work surface and sliding-type methods which involve frictional interaction by a hard asperity on a surface. Although microstructural characteristics and mechanical properties of the processed surface have been investigated, relationships between the spatial and temporal heterogeneity of the mechanics inherited in these processes and the resultant microstructure state has yet to be elucidated. Further, limited studies have been made regarding model-based approaches for design of such processes. This study focuses on understanding the mechanics, microstructure and texture evolution in these processes and quantifying fundamental process-deformation-microstructure linkages during MSM processing so to realize model-driven control of manufacturing configurations for engineering of specific microstructure surface designs. The framework employed in this work involves representation of complex multi-stage processes using process unit models,

so to examine the evolution of surface/subsurface deformation parameters given geometrical constraints of tool and boundary conditions. In this regard, simultaneous characterization of deformation history and microstructure in the surface/subsurface will provide a valuable knowledge foundation to interpret evolution of gradient microstructure in this important class of processes.

CHAPTER 1. INTRODUCTION

1.1 Project Rationale

Surface gradient microstructures have drawn significant attention due to their potential for realizing superior properties in performance applications. Components with the presence of such graded microstructures on their surface exhibit enhanced functional performance and extended service life. In the context of refinement of bulk microstructures, severe plastic deformation (SPD) is an effective mechanical-based approach to refining microcrystalline grain structures into the nanostructured regime, this featuring average grain size < 100 nm, without altering the original chemical composition of the parent material [1]. Depending on the type of refinement resulting from SPD, such grain-refined bulk materials have demonstrated increased resistance to scratching [2], fatigue [3,4], corrosion [5], and reduced thermal instability [6–8]. Unfortunately, these enhanced properties are typically achieved with a typical reduction in overall ductility by as much as 50% of the bulk value, this prohibiting the use of SPD for manufacture of many structural components [9].

The limited ductility of grain-refined bulk microstructures can be partially addressed by use of novel gradient microstructures, which enables retention of the high strength of nanostructured material and increases resistance to plastic instability [10]. The study of gradient microstructures originated from observations of thin “white layers” of refined structures on machined surfaces [11,12], which form due to localized effects of extreme plastic strain and rapid heating and cooling. Gradient microstructures evolve under heterogeneous deformation conditions wherein nanostructured materials are synthesized

on the topmost surface and deep interior regions are left in a state similar to the undeformed bulk, with a deformation gradient imposed in regions between these two extents. Grains in the subsurface region between these extents have been shown to span from nanoscale to microscale [2,5]. Further, a good balance of high strength and ductility [10,13] has been shown in uniaxial tensile tests due to abundant generation of geometrically necessary dislocations (GNDs) in the nano-grained layer during incompatible deformation in the subsurface [14]. The enhanced ductility of materials with gradient microstructure in comparison to their bulk nanostructured counterparts indeed make them more promising for use in a wide range of structural applications.

Various mechanical surface modification (MSM) processes have been studied to fabricate components with gradient microstructure over the past decade. Governed by similar deformation principles, these processes involve heterogeneity in grain refinement resultant from graded deformation caused by imposition of severe plastic deformation (SPD) on work surfaces, this referred to commonly as surface severe plastic deformation (S^2PD). Large plastic strain imposed on the surface, e.g. $\varepsilon \gg 1$, results in the generation of severely refined microstructures formed by the interplay of dislocation storage, generation and annihilation, and possible twinning [15]. In this regard, the dislocation evolution is determined by the complex effects of the surface thermomechanical state ($\dot{\varepsilon}$, ε, T) and deformation history [16]. Two main classes of MSM-based processes are common. The first of these variants are indentation-type methods, which deform the work surface by an impression interaction between tool (or pressure wave) and workpiece. The deformation field and microstructure is a consequence of the tooling, speed, temperature, and friction conditions present during processing. Specific techniques of this variant

include surface mechanical attrition treatment (SMAT) [17–19], ultrasonic peening treatment (UPT) [20,21], cavitation peening [22]. The second class of MSM-based processing are sliding-type methods, which utilize the frictional interaction caused between a sliding asperity and a work surface. Examples of this variant of MSM-based processing are surface mechanical grinding treatment (SMGT) [4,23], sliding friction treatment (SFT) [24], and low plasticity burnishing (LPB) [25].

Although characterization of microstructural characteristics and mechanical properties of the processed surface has received significant attention, a clear correlation between the spatial and temporal heterogeneity of mechanics in these processes and the resulting microstructure state has yet to be elucidated. In this regard, less attention has been paid to developing validated simulation-based methods to predict subsurface deformation given the surface processing conditions. From an experimental perspective, traditionally, strain in the subsurface has been empirically analyzed based on indirect methods based on microhardness response [4,19], curved grid distortion [26] and morphological changes of a single grain [27]. However, none of these methods have proved to be reliable, particularly at the topmost surface, since severe refinement is difficult to measure optically and has been limited to interpolation-based approaches. In addition, such post-mortem estimation methods are not capable of revealing the temporal deformation history, which is critical for understanding the strain path changes occurring in the deformation process as well as the resulting progressive microstructure evolution. The importance of strain path changes on grain refinement is clear given that continuous dynamic recrystallization (CDRX) of FCC material systems occurs at an accelerated rate as a result of imposed shear strain in different directions during equal channel angular pressing (ECAP) [28,29].

1.2 Problem Statement and Objectives

MSM-based methods based on surface severe plastic deformation principles are important for manufacture of functionally graded materials, however model-based approaches for design of such processes are limited. This study focuses on understanding the mechanics, microstructure and texture evolution in these processes and establishing model-based framework for their practical implementation.

The present study presents a fundamental investigation of heterogeneities present in mechanics and microstructure evolution during MSM-based processing. The research effort can be divided into two phases: (1) perform a carefully-planned, systematic experimental/numerical program to understand the mechanical behavior and microstructure response of a model material system, copper, in sliding-type and indentation-type processes; (2) analyze the empirical results within the critical state-framework to allow determination of intrinsic process parameters for creating gradient materials. Furthermore, focus will be placed on leveraging the insights to quantitative linkages between process-deformation-microstructure parameters and responses to optimize manufacturing process design in practical engineering applications.

1.3 Organization

This thesis is organized as follows. As the gradient microstructure materials in the current study are created by MSM-based processes, a brief review of the gradient microstructure response via surface severe plastic deformation (S^2PD) is presented first in Chapter 2, along with the overview of mechanics associated with various MSM processes. This provides the basis for the subsequent fundamental study regarding approaches in

synthesizing gradient materials, the latter of which is the focus of the thesis. The general experimental framework is presented in Chapter 3, this laying the groundwork for the subsequent analysis and discussion for different types of MSM-based processing. Indentation-type MSM methods are considered in unit model configurations and in sequential processing configurations in Chapter 4 and Chapter 5, respectively. Sliding-type MSM methods are then considered in Chapter 6. Finally, future work that follows from the results and insights developed herein are described in Chapter 7.

CHAPTER 2. LITERATURE REVIEW

2.1 Nanocrystalline Materials

Interest in the mechanical properties and corresponding deformation mechanism of nanocrystalline metals has increased significantly since the prominent review of nanostructured materials in the late 1980s [30]. The term nanocrystalline was initially used to refer material with average grain size less than 10 nm, alternative materials were classified into three groups with respect to grain size in the literature: nanocrystalline (NC) metals (< 100 nm), ultra-fined grained (UFG) metals (100 nm – 1 μm), and coarse grained (CG) metals (> 1 μm). Compared with conventional coarser grained materials, experimental observations of nanocrystalline metals have demonstrated enhanced properties including extremely high strength and hardness [23], modest ductility [31] and improved resistance in fatigue [25], friction and wear [32], and corrosion [5]. In general, accumulated plastic deformation in metals produces smaller grain size via dislocation interaction and annihilation, leading to unique properties of these materials with extraordinarily high-volume fraction of high angle grain boundaries [33,34]. Strengthening with grain size refinement in metals and alloys with an average grain size of 100 nm or larger has been well described by the Hall–Petch relationship, where dislocation pile-up along grain boundaries (GBs) and other dislocation mechanisms are the dominant strength-controlling processes. As the average grain size is reduced to less than 100 nm in the nanocrystalline regime, the dislocation activitisses become increasingly more prohibited and effects of grain boundary mediated processes, deformation twinning, and other strain accumulation schemes become more important [35,36].

2.2 Functionally Graded Materials

Even though nanocrystalline materials have been shown to possess excellent mechanical properties, these materials generally exhibit overall reduced ductility. Gradient microstructures, in which the grain size increases from nanoscale at the surface to coarse-grained in the interior region, have been regarded as an effective approach to improving ductility [37–40]. As the optical image shown in Figure 2-1(a), the gradient structured metals contain no sharp interfaces, and the ultra-hard nanocrystalline region is completely coherent, via gradual microstructure variation, with the coarse-grained region. In this regard, the incompatible deformation present across the mixture of refined and coarse grains during loading of the composite gradient material is critical in imparting both high strength and high ductility, as Figure 2-1(b) shows.

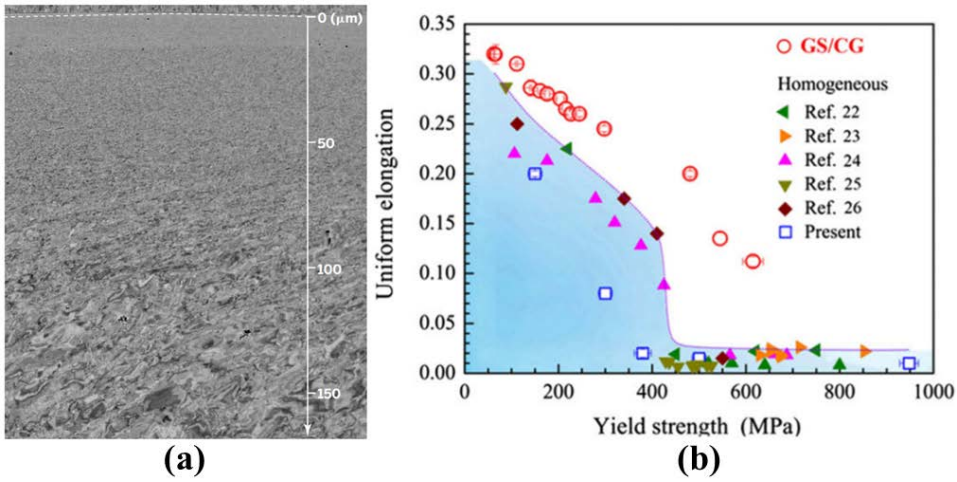

Figure 2-1 (a) Optical image showing the gradient nanograined structured material via surface mechanical grinding treatment (SMGT) to copper [10]. (b) Superior properties with high strength and high ductility in GS/CG material compared with homogeneous counterparts [13].

Theories have been proposed to explain such unique deformation characteristics of gradient materials. The development of the multiaxial stress state caused by the gradient structure was found to cause synergetic strengthening in tensile loading configurations. The strength of gradient microstructures is higher than that predicted by considering the strength of separate layers based on the rule of mixtures. This is due to the generation of more geometrically necessary dislocations by incompatible deformation, which thereby enhance strain hardening within the gradient [13,41]. At low strains in uniaxial tension, only elastic deformations occur in both the nanocrystalline surface and the coarse-grained interior. As the overall deformation level increases, the coarse-grained interior starts to experience plastic deformation, while the surface region remains in the elastic regime. In this regard, the contracted interior region introduces a compressive state in the surface and forms a multiaxial stress state in gradient materials. Finally, necking phenomenon would occur first in the surface layer with large deformation. The multiaxial stress will be reversed with the surface layer being balanced by the stable plastic core. The strain gradient near the interfaces with respect to the thickness direction activates additional slip systems and triggers promoted accumulation and interaction of geometrically necessary dislocations (GNDs) [42,43]. In addition to the effect of multiaxial stress within multiple gradient layers, Lu suggests that strain localization is suppressed due to the released intergranular stress between adjacent grains of different sizes [10]. As the strain delocalization process occurs progressively from the interior region to the nanocrystalline surface with greater deformation, the coarse-grained interior region becomes hardened, while softening occurs in the near-surface. Therefore, simultaneous occurrence of hardening and softening along

with size-dependent plastic deformation mechanisms, including dislocation slip and grain boundary migration, is activated concurrently in gradient materials.

2.3 Deformation-Based Microstructure Evolution

2.3.1 Dislocation Structures

Microstructure evolution is closely related with the formation of dislocation cells at the onset of plastic deformation. Various types of dislocation structure are composed by dislocation cell boundaries, as the schematic of dislocation structure shown in Figure 2-2(a). Dislocation boundaries are classified into two types: incidental dislocation boundary (IDB) and geometrically necessary boundary (GNB). IDBs form by mutual and statistical trapping of dislocations, while GNBs form between regions of different strain patterns to accommodate the accompanying difference in lattice rotation due to activation of slip systems. Progressive formation of IDBs and GNBs results in refinement of microstructure and leads to the formation of cells. The main difference between evolution of dislocation boundaries into IDBs and GNBs is their inherently different scaling behavior and rate of increase in the average misorientation angle across the boundaries with increasing strain [44,45]. Misorientation angles increase for both types of boundaries at low strain, while GNBs can develop into high angle boundaries ($\theta > 15°$) [46]. This leads to form UFG microstructures by repeated imposition of extreme strain.

GNBs are further classified into four categories depending on the microstructure in their neighboring regions: dense dislocation wall (DDW), lamellar boundary (LB), micro band (MB), and sub-grain (SG). DDWs are the dislocation structures that surround cell blocks. Their spatial alignments are dictated by the prevailing macroscopic deformation

geometry. LBs are nearly planar GNBs that outline elongated cell blocks arranged in consecutive rows, as Figure 2-2(b) shows, where their major direction is aligned with respect to the dominant direction of the deformation process with the imposition of large strains ($\varepsilon > 1$) [5]. MBs are plate like regions formed by two closely spaced cell blocks. Finally, SGs refer to dislocation free volumes with boundaries featuring medium to high misorientation with respect to neighbors. A threshold value of 2˚ in misorientation angle is commonly used to distinguish a cell and a sub-grain [47,48].

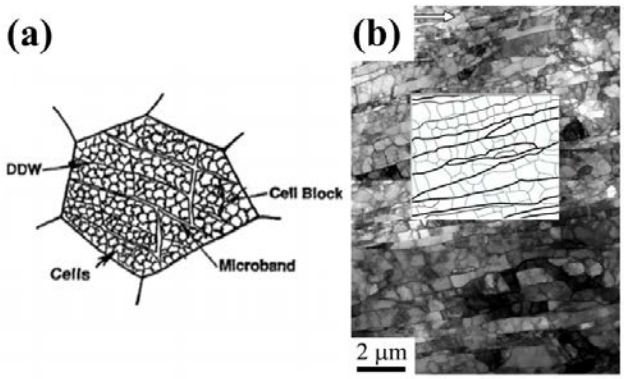

Figure 2-2 Dislocation structures form in (a) small strains and (b) large strains [27]

condition.

2.3.2 Microstructure Refinement

Recrystallization processes have been known to govern the formation of new grains with decreasing grain size. Here, the grain refers to the domains surrounded by high-angle boundaries featuring misorientation angle $\theta > 15^{\circ}$. The recrystallization process without the onset of plastic deformation is classified as static recrystallization (SRX) [49], where the workpiece undergoes high temperature along with moderate deformation. In contrast, the recrystallization process resultant from extreme plastic deformation is classified as dynamic recrystallization (DRX). The key difference between DRX and SRX is that in the

former, energy is continuously imposed into the material system and the ongoing deformation produces recrystallized grains with new dislocations. DRX occurring in a fast and discontinuous manner is called discontinuous dynamic recrystallization (DDRX), whereas that occurring in a slow and continuous manner is termed as continuous dynamic recrystallization (CDRX) [15]. In DDRX, new strain-free grains with high angle grain boundaries (HAGB) evolve in the place of pre-existing grains [50]. CRDX involves low angle grain boundaries (LAGB) that convert into HAGB during deformation.

CDRX contains three commonly known variants. Its simplest form involves progressive formation and evolution of IDBs and GNBs. In this regard, new grains are created by subdivision during imposition of strain, eventually resulting in UFGs. A distinguishing microstructural feature between microstructures resulting from CDRX and DDRX is the more random crystallographic texture from the latter. In fact, this feature can be used to successfully identify whether CDRX or DDRX was active during plastic deformation [51]. A variant of CDRX is geometric dynamic recrystallization (GDRX), which is morphologically driven and depends on the shape of the grains within the volume undergoing deformation. The starting grains of the polycrystalline aggregate flatten with relatively large strain deformation. Interplay of grain boundary tensions arising from neighboring cells, coupled with dynamic recovery of dislocation densities, coaxes serrations in the boundaries of the flat grain. With the progressive imposition of shear, the grains become progressively flatter whereby the serrations on the opposite faces of the grain come close to each other. On reaching a threshold, the long serrated flat grain is pinched due to these serrations whereby several grains are created from one single flattened grain. A consequence of the geometrical nature of this variant of GDRX is that the size of

the grains resulting from the process matches closely the mean cell size. The third variant of CDRX is rotational dynamic recrystallization (RDRX). RDRX involves progressive rotation of sub-grains close to pre-existing grain boundaries whereby a misorientation gradient develops between the center and the edge of a grain. In this manner, a necklace structure occurs due to the formation of small segments close to a grain boundary. The mechanism is believed to be caused by inhomogeneous plasticity and dynamic recovery at grain boundaries [15]. Microstructure resulting from large deformation may result from these variants of DRX. Therefore, identification of any specific mechanism of microstructure evolution to be active during deformation is generally a difficult task.

2.3.3 Crystallographic Texture

Crystallographic textures refer to a non-uniform distribution of crystallographic orientations in a polycrystalline aggregate, where the preferred orientations are developed via thermomechanical history of the material during almost all the stages of material processing. Textures are statistically described by an Orientation Distribution Function (ODF) corresponding to a distribution of points in a 3D orientation space. One may then signify ODF as $f(g)$ where g is a point within the orientation space. The physical volume fraction of orientations containing orientations within a certain region $\Delta\Omega$ of the orientation space is given by [52]:

$$\frac{\Delta V}{V} = \frac{\int_{\Delta\Omega} f(g)dg}{\int_{\Omega_0} f(g)dg} \tag{1}$$

It is customary to use $f(g) = 1 \forall g$ for uniform ODFs whereby $f(g)$ is also called Multiples of Random Distribution (MRD). In addition, a pole figure is the 2D

representation of orientation points in space derived from that drawn in the 3D space with stereographic projection. Pole figures are readily empirically measurable using X Ray Diffraction and facilitate easy representation of crystallographic textures. This makes them an important tool because of ease of sample preparation for XRD when compared with other techniques of crystallographic texture analysis like OIM using Scanning Electron Microscopy (SEM) coupled with Electron Back Scattered Diffraction (EBSD).

Preferred crystallographic textures in polycrystals originate as a consequence of thermomechanical history imposed by plastic deformation [52,53], this concomitantly influencing evolution of microstructure [54,55]. For instance, deformation involving strain histories constituting strain path changes and interfering crystallographic textures are known to result in accelerated microstructure refinement. This phenomenon has been seen in the C route of equal channel angular pressing (ECAP), which involves globally imposed strain path changes. After two passes with $\varepsilon \sim 2$, the C route results in a smaller final grain size compared with rolling to $\varepsilon \sim 2$, the latter featuring a monotonic strain history [54]. Similar variation has also been seen for different ECAP routes. For instance, the B route has been recognized to result in faster grain refinement with more $-ve\frac{\partial \delta}{\partial \varepsilon}$ where δ is the grain size, than other routes during ECAP of pure Al due to global changes in direction of imposed shear [56]. Presumably, the evolution of microstructures and crystallographic textures during indentation also follows complex routes due to heterogeneity in imposed plastic strains [6,7].

2.4 Surface Severe Plastic Deformation

Various mechanical surface modification processes have long been used to endow mechanical components with enhanced properties across an array of technological applications. Functionalization of component surfaces generally involves altering the chemistry, microstructure, topography and stress state—collectively termed as integrity—of the material surface and subsurface. Methods used for surface functionalization are broadly classified as being either additive-based (e.g. coating, deposition, implantation) or deformation-based (e.g. machining [57], burnishing [5], surface impact [23]) treatments. Among these, the latter grouping is inherently more scalable for structural component applications as they are integrable in processing frameworks based on severe plastic deformation (SPD: $\varepsilon \gg 1$) to tailor surface microstructure and stress state. For deformation-based configurations, surface integrity is determined by the deformation field and corresponding strain rate, strain and temperature. In this regard, a fundamental need exists to understand and quantify relationships between deformation mechanics and controllable processing parameters, as well as corresponding effects on various elements of surface integrity. Such process–mechanics–structure frameworks are essential towards optimization of surface severe plastic deformation (S^2PD) methods for engineering high-performance mechanical components.

Surface mechanical attrition treatment (SMAT) is an S^2PD method that has been used to endow metallic components with enhanced structural (e.g. subdued wear [58], increased fatigue life [59]) and functional (e.g. subdued corrosion [5]) response. This process involves repeated surface impact by solid or fluidic shots (e.g. shot peening, cavitation peening) or actuated tooling (e.g. ultrasonic impact treatment [60]). SPD

imposed due to the repetitive deformation results in grain fragmentation, leading to formation of ultrafine-grained (UFG) and nanostructured microstructures in the surface and subsurface [61,62]. The mechanics of microstructure evolution during surface deformation have been studied and effects of thermomechanical conditions (e.g. strain rate, strain, temperature) on resulting microstructures have been delineated in several materials featuring different intrinsic properties in terms of crystallography and stacking fault energy [19]. The second class of S^2PD-based processing are sliding-type methods, which utilize the frictional interaction caused between a sliding asperity and a work surface. Examples of this variant include surface mechanical grinding treatment (SMGT) [4,23], which employs a spherical tool sliding on the surface; and sliding friction treatment (SFT) [24], which utilizes intense "stirring" and bonding of the material by high frictional interaction. All these S^2PD processes are capable of imposing large plastic strains and the plastic flow on workpiece surfaces with quite complicated deformation evolution compared with ones in homogeneous SPD processes, including equal channel angular extrusion (ECAE) [63] and high pressure torsion (HPT) [64]. A machining-based sliding indentation with a tool offers a good model for the unit interaction occurring in these processes. Study of the deformation produced by the sliding indenter can enable improved control of the deformation parameters in these S^2PD-based processes.

CHAPTER 3. EXPERIMENTAL

In this chapter, details of the experimental approach used in the present study, including experimental setup, digital image correlation (DIC) analysis procedure, deformation measurement, microstructure characterization, and crystallographic texture simulation are described.

3.1 Surface Processing Methods

3.1.1 Indentation-Type Process

MSM-based processes utilizing an indentation-type interaction rely on repeated impressions on the processed surface to accumulate higher strain and effect grain refinement. The localized surficial deformation in each impression can be analogously investigated in the framework of the unit indentation model. A schematic of a two-dimensional circular indentation model is shown in Figure 3-1(a). In this model, several processing parameters including depth of indentation (h), indentation rate (v), and circular indenter radius (R) are critical factors that govern the extent and severity of the subsurface plastic field at specific subsurface locations in the polar coordinate system (r, λ). This unit model provides a basic framework for predicting the heterogeneous mechanical deformation and correlated microstructure response occurring in a single indentation interaction.

3.1.2 Sliding-Type Process

The other majority of surface generation and surface deformation processes such as burnishing, grinding, and sliding involve frictional engagement of a hard tool against a

work surface at the micrometer scale and so-called “stirring” of material, akin to fluid-like plastic flow behavior, while advancing of the tool along the workpiece. In this process, the microstructure state evolves by the severe shear strain and dissipated heat imposed by the frictional interaction. This interaction is modelled as a hard 2D wedge-based tool engaging into a workpiece surface in the direction normal to free surface and burnishing the workpiece. Figure 3-1(b) illustrates critical processing parameters for a sliding-type unit model, wherein the tooling geometry (α), engagement depth (h), and sliding rate (v) are critical in determining the extent and severity of the subsurface deformation. Such a model configuration is analogous to the conventional Merchant model used to describe an orthogonal cutting configuration under plane-strain conditions [65].

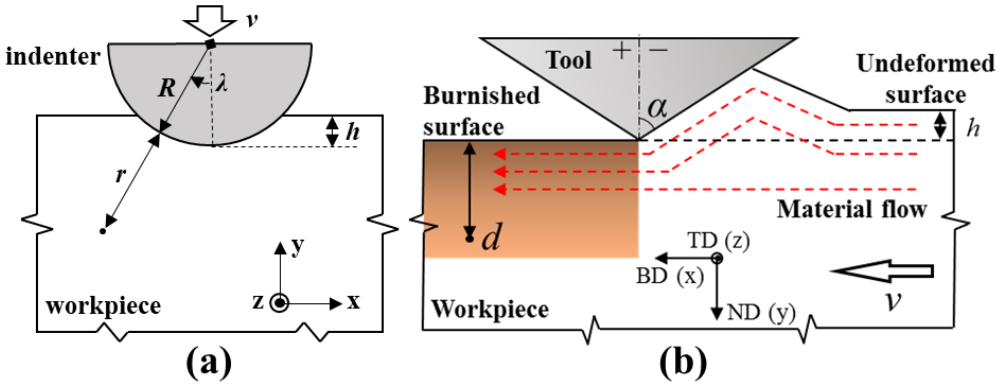

Figure 3-1 Schematic representation of (a) circular indentation and (b) wedge-based burnishing configuration.

In this study, the flow and deformation, in terms of velocity, strain rate and strain, are measured for two model systems under different process parameters. Furthermore, microstructure of the processed surfaces are characterized to complement the deformation

measurement. These results will be used to assess control of gradient deformation and microstructure on material surfaces through control of sliding-type and indentation-type process parameters.

3.2 Flow and Deformation Measurement

3.2.1 Experimental Setup

The experimental setup used for characterizing the deformation level in two model systems is conceptually illustrated in Figure 3-2. Custom setups were manufactured to perform plane-strain deformation, where the tool is fixed stationary and the workpiece is moved linearly against the tool. The imaged side of workpiece is constrained using a glass plate, which helps prevent out-of-plane flow and maintains a state of two-dimensional deformation. A close-die design has been applied for two configurations for minimizing the compliance issues and out-of-plane flow. In Figure 3-3(a), the custom setup is designed to simulate an in-plane circular indentation process, wherein the workpiece deformation is constrained in-plane and the surface is deformed by relative motion of a tool indenter body loaded by a compression load frame. In this case, control of the tool radius is possible by interchanging the indenter body. A tempered glass cover is utilized on the observed work surface to ensure the plane strain condition and to preserve optical transparency. For a unit-scale sliding-type MSM process, another experimental setup is designed and shown in Figure 3-3(b). In this experimental setup, the workpiece is translated relative to a tool body by the motion provided by the compressive load frame. In this case, the tool is a wedge-shaped body constructed of high speed steel with control of the relative angles and edge radii possible by interchanging the wedge-shaped tool. Experiments were carried out using

an Instron uniaxial load frame and material flow was imaged using a high-speed camera (PCO Dimax HD) coupled to an optical micro-lens assembly (Navitar Zoom 6000) as shown in Figure 3-3(c). The size of imaged field is ~ 2000 pixels × 2000 pixels with a spatial resolution of up to 1.5 μm/pixel. To achieve more accurate measurement, asperities are introduced onto the workpiece surface prior to deformation process with ~ 600 grit SiC pads. A sequence of images is obtained for measuring local velocity vectors per pair of consecutive images using digital image correlation (DIC) technique, resulting in a comprehensive and quantitative record of flow in space and time. Deformation parameters including strain rate, strain is computed from the measured DIC-obtained displacement fields. Details of each step in the experiments and the image analysis is explained in the following.

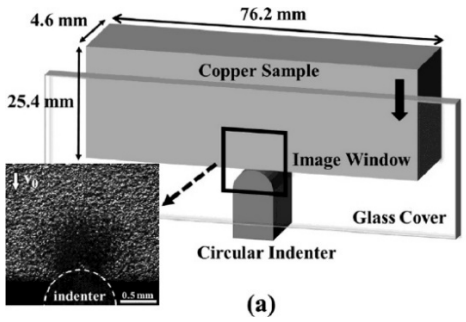

Figure 3-2 Experimental configuration for *in situ* imaging of plane-strain circular indentation with representative optical image inset.

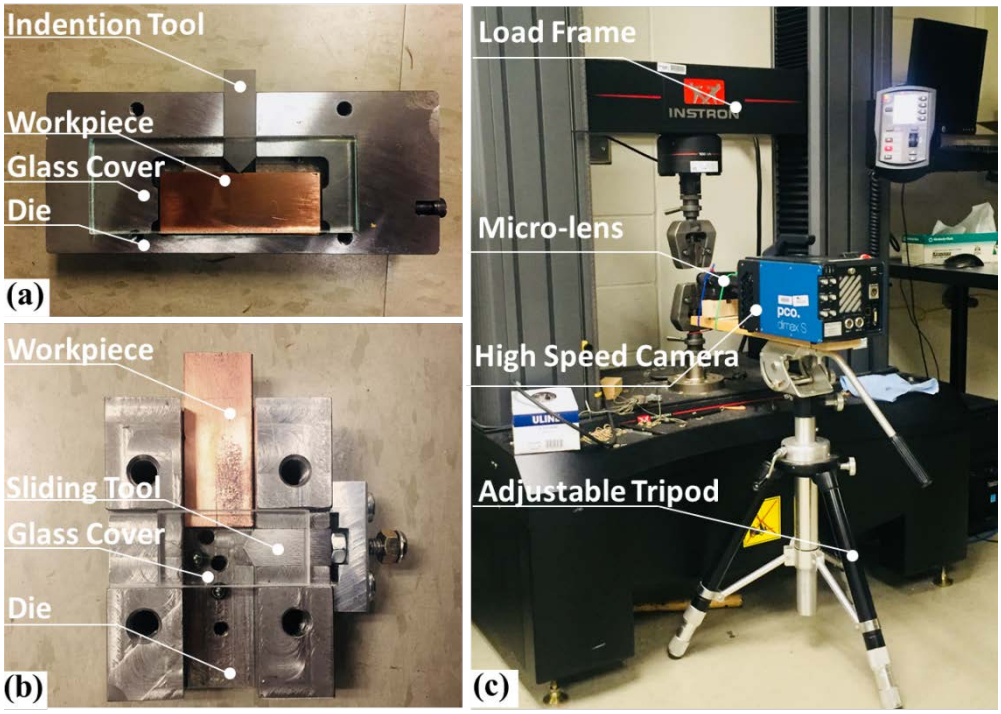

Figure 3-3 Custom setup for unit (a) indentation-type and (b) sliding-type model. (c) Experimental setup for the DIC platform.

3.2.2 DIC Analysis

The procedure of DIC analysis to obtain local velocity vector fields for each pair of two consecutive captured images is illustrated in Figure 3-4. The analysis adopts FFT-based cross correlation and a Newton-Raphson iterative algorithm [66], allowing to resolve high gradient in deformation level. FFT-based evaluation is firstly performed using the interrogation window size of 32 pixel × 32 pixel with grid size of 5 pixel × 5 pixel. The obtained displacement vectors v_x and v_y in x and y direction at sampling positions are used as the initial displacement gradient vectors. An iterative algorithm is used to provide measurement in sub-pixel accuracy, where the correlation coefficient is minimized by

determining six deformation parameters v_x, v_y, $\frac{\partial v_x}{\partial x}$, $\frac{\partial v_y}{\partial x}$, $\frac{\partial v_x}{\partial y}$, and $\frac{\partial v_y}{\partial y}$. During each iteration pass, the interrogation window is updated by deform/shift of the window for the next pass. Sub-pixel accuracy is achieved by modelling the gray level of the image using bicubic interpolation. The usage of the Newton-Raphson method in partial differential corrections significantly reduces the computation time. Given the assumption of continuity in deformation fields, spurious vectors are eliminated using normalized median test and further replaced by the average of surrounding displacements [67]. The final displacement field is smoothed using linear regression with a 3 pixel × 3 pixel filter [68].

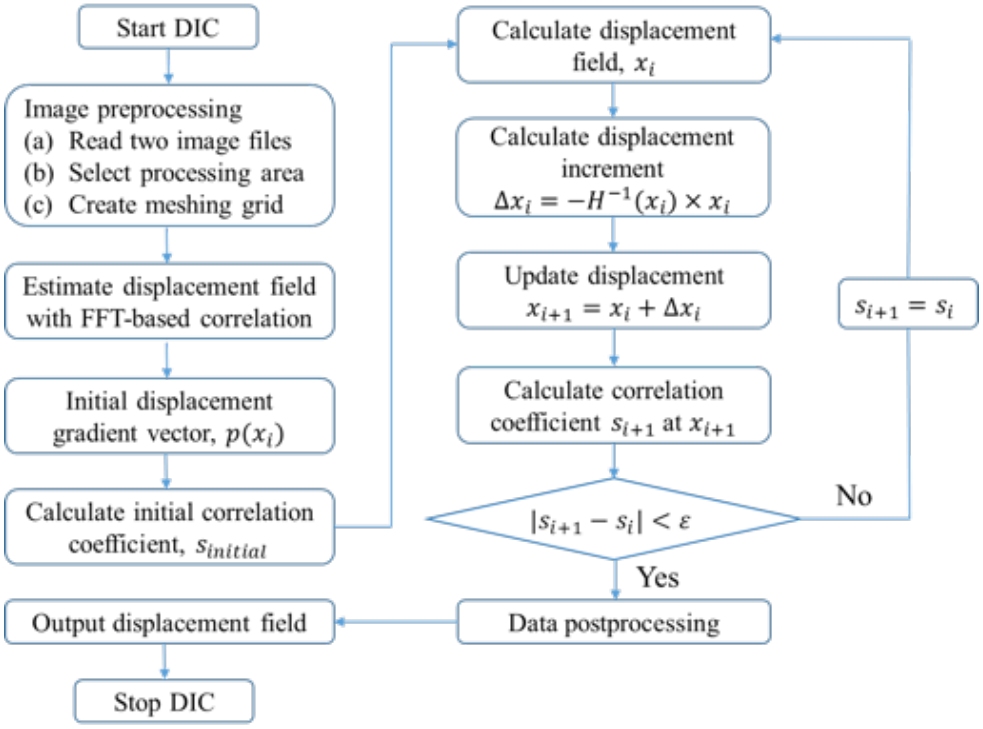

Figure 3-4 Flow diagram of sub-pixel DIC method.

A custom MATLAB program has been implemented based on the procedure of DIC analysis summarized in Figure 3-4. The measured resulted has been validated using artificially simulated image pars with pre-defined displacement [69]. The validation shows that the measurement error of the program is within 0.01 pixel.

3.2.3 Deformation Measurement

The sequence of displacement vector fields contains all the information in describing deformation. Direct spatial differentiation of the velocity field provided the small strain rate tensor as in Eq. 1,

$$\dot{\varepsilon}_{ij} = \frac{1}{2}\left(\frac{\partial v_i}{\partial x_j} + \frac{\partial v_j}{\partial x_i}\right), i, j = 1, 2 \tag{1}$$

where $x_1$and x_2 refer to x and y direction in Figure 3-1. It is assumed that the incremental strain is purely plastic, since the elastic part can be ignored in the large-strain deformation process. Using von Mises criteria, the incremental effective strain rate can be computed as in Eq. 2,

$$\bar{\dot{\varepsilon}} = \sqrt{\frac{2}{3}\dot{\varepsilon}_{ij} : \dot{\varepsilon}_{ij}} \tag{2}$$

The resulting effective strain field was generated by temporal integration of local incremental strain fields along path lines, this given by Eq. 3,

$$\bar{\varepsilon} = \oint \bar{\dot{\varepsilon}} dt \tag{3}$$

A relative error of less than 0.01 is found for the measured displacement and velocity field by evaluation of simulated displacements of real marker fields. Correspondingly, a total strain measurement error of 0.1 has been validated for the images obtained in the present study.

The combined effect of strain rate and strain, as well as temperature, determines the microstructure resulted from thermomechanical history. The strain rate tensor is further applied in determining the crystallographic texture evolution during the deformation process. For instance, the historical trajectory of strain rate tensor components is used as the primary input in simulating texture evolution development with the Taylor model and Visco-Plastic Self-Consistent (VPSC) model [70,71].

3.3 Microstructure Characterization

In the present study, the surface and subsurface microstructure of pre- and post-deformed workpieces are characterized by electron backscatter diffraction-based orientation image microscopy (OIM) on a Mira Tescan 3 thermal field emission scanning electron microscope equipped with an EDAX TSL EBSD detector. The surface is prepared by traditional mechanical polishing down to a 0.05 μm mirror finish using colloidal silica suspension through 6 μm, 3 μm, and 1 μm polishing. Subsequently, vibratory polishing with a VibroMet 2 unit for 30 min. The accelerating voltage used during SEM-based characterization is 25 KV with scan steps ranging from 0.08 to 1 μm. The resulting EBSD micrographs are analyzed by characterizing the average grain and sub-grain sizes (δ_{15° and δ_{2°) defined as domains enclosed by boundaries featuring misorientations > 15˚ and 2˚, respectively. δ_{15° and δ_{2° are calculated by finding area weighted means of grain and sub-grain sizes in the scanned EBSD micrographs. This is done by using the TSL OIM 5.0

software in which δ_{15° and δ_{2° of an individual grain/subgrain is found by calculating the corresponding area enclosed and then finding the diameter of a circle with equal area. Finally, surface crystallographic textures are extracted from the discrete OIM data using MATLAB-based software MTEX.

3.4 VPSC Simulation

Numerical simulation of the crystallographic texture evolution is conducted using a FORTRAN implemented framework of the visco-plastic self-consistent model (VPSC) [72]. The VPSC model treats each grain as a visco-plastic inclusion in a homogeneous effective medium and updates the mechanical state of the medium self-consistently at each simulation step. Herein, the framework relies on the deformation history in the form of the velocity gradient $L_{ij} = \frac{\partial v_i}{\partial x_j}$, which is obtained from the DIC-based characterization of material flow. In addition, performance of the VPSC framework in simulating evolution of crystallographic textures depends on the pristine texture. This was represented by 2000 discrete orientations extracted from the OIM data of the pre-deformed sample specimen. Validation of the simulated textures is facilitated by comparison with the measured textures extracted on the deformed surface. The orientation distribution function (ODF) is quantified by the texture index $T = \int {f_{exp}}^2 dg$ and the normalized texture index $\hat{T}_d = \frac{\int [f_{sim}(g) - f_{exp}(g)]^2 dg}{\int [f_{exp}(g)]^2 dg}$, where g refers to the local orientation in the Euler space (φ_1, Φ, φ_2) [70].

CHAPTER 4. UNIT-TYPE INDENTATION PROCESSES

4.1 Introduction

Comprehensive understanding of the deformation field in indentation configurations is of importance due to the bearing it provides for a deeper understanding of the corresponding load response and microstructure evolution. The deformation field in indentation has been extensively studied using high-fidelity materials characterization methods; most of these investigations have relied on post-mortem assessments involving grid-based measurements [73], microhardness mapping [74] and metallographic observation [75]. While these methods have enabled visualization of the final deformed state, they generally provide limited understanding of the evolving deformation field. In this regard, in situ imaging methods have been applied to elucidate time-dependent characteristics of the flow field during indentation with flat punch [76] and wedge [77] indenter geometries. These direct *in situ* approaches for measuring the deformation are promising as they can provide direct observations of the evolving flow field, which itself is useful to validate assumptions and predictions of various numerical and analytical models.

Analytical approaches to describe mechanical response during indentation must account for two stages present during the development of the deformation zone. At the initiation of contact between the indenter and workpiece, elastic response dominates the deformation field and the plastic zone is constrained within a negligible volume at the indenter tip. In this regime, Hertz's solution for the elastic stress and strain distributions provides for reasonably accurate predictions of the flow field with various indenter

geometries [78]. At increasing indentation load, the workpiece undergoes plastic yielding and elastic-plastic response occurs wherein an expanding zone of plastic flow is constrained in the far field by an overall elastic response.

Expanding cavity models (ECMs) are a relatively popular class of analytical models that provide capability to consider the effects of both elastic and plastic response on deformation field evolution during the indentation process. These models give reasonable approximation of plastic flow and loading response and are based on the modeling of the deformed field as a radially expanding cylindrical or spherical cavity [79,80]. Assumption of a radially symmetric cavity originated from early work of Samuels and Mulhearn [81] and Mulhearn [81], where deformations in the vicinity of a blunt indenter (e.g., wedge-shaped or conical indenter with a large apical angle) were observed to exhibit a compression-type nature with near-radial symmetry, while a localized cutting-type flow field was observed for sharp wedge indenters [82]. Based on these observations, the plastic flow was assumed to be triggered by the expansion of an incompressible hemispherical core of material subjected to internal hydrostatic pressure [79]. In this regard, ECM solutions of loading response and the local deformed state are based on Hill's solution [83] of an internally pressurized spherical shell for an elastic, perfectly-plastic material following von Mises yielding criterion. ECM-based approaches have been extended to model deformation for materials governed by a range of constitutive behavior that include ductile [80,84,85], brittle [86] and pressure-sensitive response [87,88]. More recently, revised ECM formulations have been proposed to account for the effects of locally varying surface morphology on the deformation field during indentation [84,89,90].

While ECM-based approaches have been widely used to describe the deformation field in indentation-type loading, primary assumptions of these models pertaining to the overall deformation field have not been well addressed. In terms of deformation field geometry, experiments and simulations have highlighted inaccuracies in the modeling of the elastic-plastic interface in terms of shape and relative location [91]. These discrepancies likely have an effect on model prediction accuracy, as conventional ECM-based approaches typically underpredict the hydrostatic pressure in the cylindrical or spherical cavity compared with the actual mean indentation pressure [79,84]. Further, few experimental studies have been made to-date that consider the direct validation of the characteristics of the deformation field in terms of deformation geometry and most of these have been post mortem in nature. In this regard, recent advances in the use of in situ imaging methods to study indentation offer significant opportunity to identify time-dependent characteristics of the flow field and validate model assumptions.

Additionally, ease of sample preparation and high throughput make indentation a powerful tool for mapping constitutive behavior of metals [92] and characterization of an array of material parameters such as residual stresses [75], stress-strain relationships [92], scale dependence of material response [93] and critical resolved shear stress . These parameters are extracted from force (P) vs. indentation depth (h) curves representative of the material's mechanical behavior, sometimes supplemented with additional post-mortem characterization [94]. The mechanical behavior of materials during indentation is complicated by heterogeneous deformation [76], orientation dependence of material flow [95,96], anisotropy of yield surfaces [97] and friction effects [98] that render force (P) vs. indentation depth (h) curves equivocal. The influence of these effects complicates

characterization of constitutive behavior as a function of fundamental material parameters. This can be mitigated with a complete understanding of plastic flow during indentation, whereby individual contributions from the effects to the resulting P vs. h curves can be quantified. A parameter that has been shown to play a profound role on the plastic response of metallic materials is crystallographic texture [52]. Presence of textures constituting high concentrations of preferred orientations is known to influence formability by governing the onset of shear banding [99], anisotropy in polycrystal yield strengths [100] and stress-strain relations [101]. Predicting behavior in the presence of crystallographic textures often necessitates modeling their evolution during plastic deformation which can be done using the Visco Plastic Self-consistent (VPSC) framework coupled with image correlation techniques or finite element methods (FEM) explicitly [57] or implicitly [102].

The objective of this chapter is to directly characterize the flow field during indentation in situ and, relative to ECM-based approaches for describing this field, examine the validity of assumptions made regarding the deformation of the hydrostatic core between the indenter and plastic zone that surrounds it. Based on these in situ measurements, a calibrated ECM is formulated to improve prediction of the deformation field and indentation load. The resulting model predictions are directly compared with the in situ experimental observations and estimates made using a conventional ECM-based approach. To complement these mechanics-based investigations, microstructure and crystallographic texture during indentation are investigated to understand the dependence of microstructure in the deformed subsurface on strain path changes during processing. Localized differences in microstructure evolution with respect to indenter positioning are explained in terms of

spatial strain-gradients and strain path changes that contribute significantly to anomalous microstructure and texture evolution within subsurface plastic zones.

4.2 Experimental Platforms

A series of plane-strain circular indentation experiments were conducted using an A2 steel circular indenter of 1 mm diameter loaded against oxygen-free high-conductivity (OFHC) copper and commercial pure lead workpieces, depicted in Figure 3-2. The true strain-stress curve of copper and lead were measured in a standard uniaxial tensile test conducted according to ASTM E8/E8-15. The Young's modulus E, yield stress σ_y and hardening exponent n of the copper were measured as 122 GPa, 132 MPa and 0.1125, respectively. The Young's modulus E and yield stress σ_y for lead were measured as 12 GPa and 7 MPa, respectively. The workpieces were machined into bars with dimensions of 76.2 mm × 25.4 mm × 4.6 mm. A uniaxial testing machine (Instron 5980) was used to move the workpieces at a constant displacement rate (10 μm/s) toward the stationary indenter while simultaneously capturing load information. The deformation process was directly analyzed in DIC-based experimental setup. Characterization of microstructure and crystallographic texture was facilitated by the procedure described in Chapter 3.

4.3 Deformation Evolution

4.3.1 Sinking-in Behaviour

In situ imaging was used to map the morphology of the free surface of copper and lead so to accurately measure the real depth of indentation and to correlate this with the DIC-based imaging analyses. As the schematic in Figure 4-1(a) shows, sinking-in

behavior, commonly observed in indentation of both strain hardening and perfectly plastic materials [103], reduces the theoretical indentation depth (h_t) to some value for the real indentation depth (h_r) and simultaneously decreases the effective contact area between indenter and workpiece. From the figure, h_t is defined as the distance between the workpiece free surface and the indenter tip, whereas h_r is defined by the extent of the contact between the indenter and the workpiece.

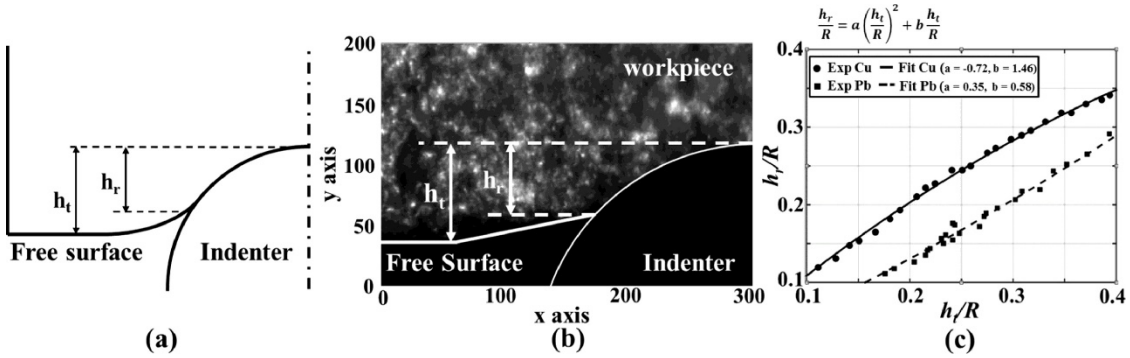

Figure 4-1 (a) Schematic of sinking-in behavior during indentation and dimensional parameters, theoretical depth of indentation (h_t) and real depth of indentation (h_r). (b) Optical image showing nature of the free surface of copper during circular indentation with sink-in response. (c) Correlation between real and theoretical indentation depths for copper and lead.

Digital images were quantitatively mapped, as shown in Figure 4-1(b), to determine the evolution of the sinking-in behavior occurring in the free surface of the copper. The same procedure was also applied to lead. The relationships between h_t/R and h_r/R for copper and lead are summarized in Figure 4-1(c) over the range of indentation depths

investigated. From the figure, the theoretical indentation depths h_t/R increase from h_t/R $\sim$0.1 to h_t/R $\sim$0.4, while the real indentation depths increase up to h_t/R $\sim$0.35 and h_r/R $\sim$ 0.29 for copper and lead, respectively. It is indicative of the greater importance of sinking-in behavior in affecting plastic flow at larger indentation depths. The sinking-in response is modeled by a second order polynomial function as in Figure 4-1(c), wherein the fitting coefficients are determined by experimentally obtained data. Such non-linear response in sinking-in is expected because of the nonlinear increase of the contact area on the circular indenter during the indentation process [104].

4.3.2 Deformation Fields

Local material displacement in the deformation zone during indentation was obtained by DIC-based analysis of the images obtained. The normalized velocity fields (v_i/v_0) are shown in the hybrid quiver-contour plots of Figure 4-2 for a range of indentation depths from the point of initial contact up to a normalized indentation depth of h_t/R = 0.330. The hybrid quiver-contour plots are overlaid on the optical image sequence to enhance visualization of the deformation process. From the figure, the bulk of the material is displaced at a velocity approximately equal to that of the preset indentation velocity ($v_i/v_0 \sim 1.0$). In the regions surrounding the indenter, the velocity distribution is graded with substantial changes in intensity and lateral extent with increasing indentation depth. Further, in the immediate vicinity of the indenter-workpiece contact, a region of material stagnation ($v_i/v_0 \sim 0.1$) is clearly observed, demonstrating a rigid translation relative to the workpiece. The lateral extent of this stagnation region increased with increasing indentation depth, ranging from 0.68R to 1.41R over the range of indentation

depths investigated. The formation of these material stagnation zones is indeed consistent with other direct assessments of deformation occurring in other indentation configurations (e.g., flat punch, large apical angle wedges) [77,105].

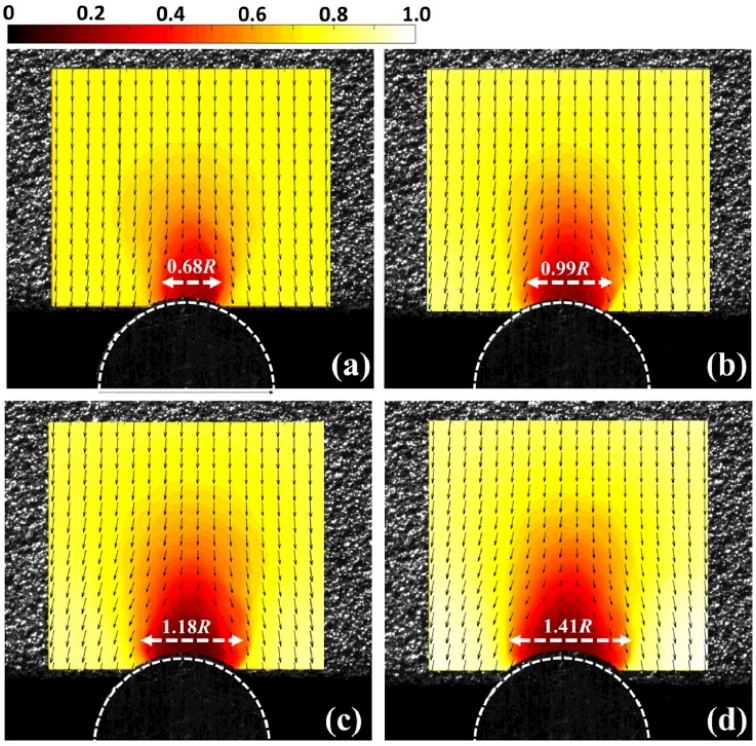

Figure 4-2 Normalized velocity (v_i/v_0) distribution fields at normalized indentation depths of h_t/R = (a) 0.111, (b) 0.165, (c) 0.224 and (d) 0.330 for copper. Vectors in quiver plot indicate direction of local material velocity.

Spatial differentiation of the velocity fields of Figure 4-3 provided measurement of the strain rate in the deformation zone during indentation, with $\dot{\varepsilon}_{ij} = \frac{1}{2}\left(v_{i.j} + v_{j,i}\right)$. The effective strain rate distribution, calculated from the measured strain rate tensor by $\bar{\dot{\varepsilon}} =$

$\sqrt{\frac{2}{3}\dot{\varepsilon}_{ij}\dot{\varepsilon}_{ij}}$ was normalized by indentation strain rate (v_0/R) and is summarized in Figure 4-3(a)–(d) for the same range of normalized indentation depths. From the figure, the evolving fields identify regions of high strain rate in the deformation zone. These high strain rate regions occur as banded segments that are roughly semicircular and originate from the point of contact between the indenter and workpiece. With increasing indentation depth, these high strain rate bands extend to greater subsurface depths and become increasingly diffuse. The lateral extent of the banded region is similar to that observed for the velocity fields, this varying from $0.68R$ to $1.41R$ over the range of indentation depths investigated.

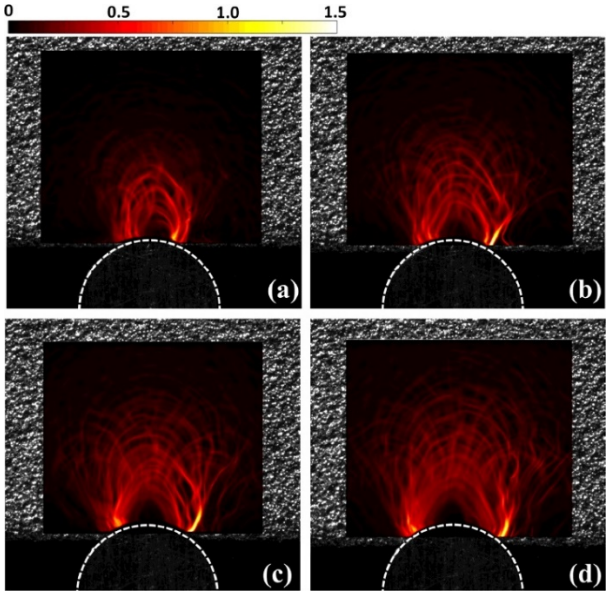

Figure 4-3 Normalized strain rate distribution ($\dot{\varepsilon}R/v_0$) fields at normalized indentation depths of h_t/R = (a) 0.111, (b) 0.165, (c) 0.224 and (d) 0.330 for copper.

In terms of the maximum strain rate imposed on the material, the effective strain rate reaches a maximum of 1.5 times the indentation strain rate within the banded region. Outside of the banded region where the deformation is primarily elastic, the material experiences relatively negligible normalized strain rates less than 0.1. Similarly, the material in the region immediately flanking the indenter also is exposed to low incremental strains, further indicative of deadzone formation at the vicinity of the indenter.

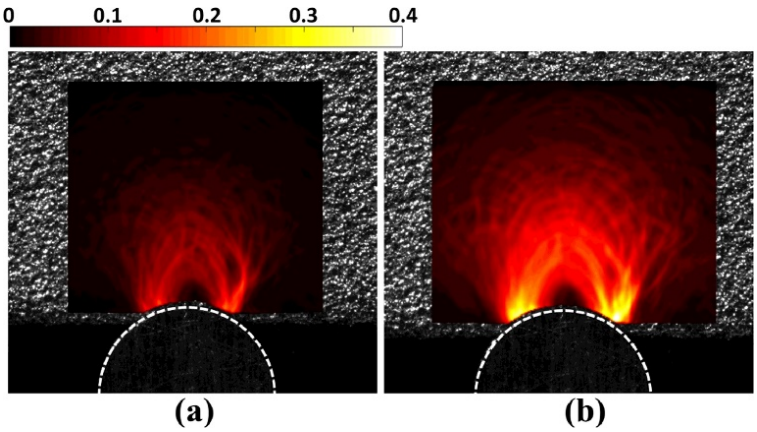

Figure 4-4 Effective strain distribution fields deformed on the top at normalized indentation depths of h_t/R = (a) 0.190 and (b) 0.330 for copper.

The effective strain imposed in the workpiece during indentation was obtained by integration of the effective strain rate fields along discrete material trajectories in the deformation field, as $\bar{\varepsilon} = \int \dot{\bar{\varepsilon}} dt$. Effective strain distributions at indentation depths of h_t/R = 0.190 and h_t/R = 0.330 are shown in Figure 4-4(a) and (b), respectively. From the figure, in the regions immediately underneath the indenter, a region of negligible strain is observed wherein ε < 0.01 at both indentation depths. This observation further confirms that the

deadzone region underneath the indenter has not been exposed to appreciable straining during indentation and undergoes a rigid body translation during the deformation process. Flanking the deadzone region is a banded region of high strain wherein higher strains are observed closer to the indenter-workpiece contact. The maximum effective strain in this region at normalized indentation depths of h_t/R = 0.190 and h_t/R = 0.330 was $\varepsilon \sim 0.23$ and $\varepsilon \sim 0.34$, respectively. Further, greater indentation depths were seen to increase the size of the plastic zone into the subsurface. At greater subsurface depths, the strain level falls below an appreciable level $\varepsilon < 0.01$, wherein elastic deformation is likely more dominant.

4.3.3 Indentation Load

The load response was simultaneously measured during the indentation process and normalized by the workpiece thickness P/t, provided in Figure 4-5. The normalized load also exhibited non-linearity and monotonically increased over the range of indentation depths investigated from 140 to 310 N/mm.

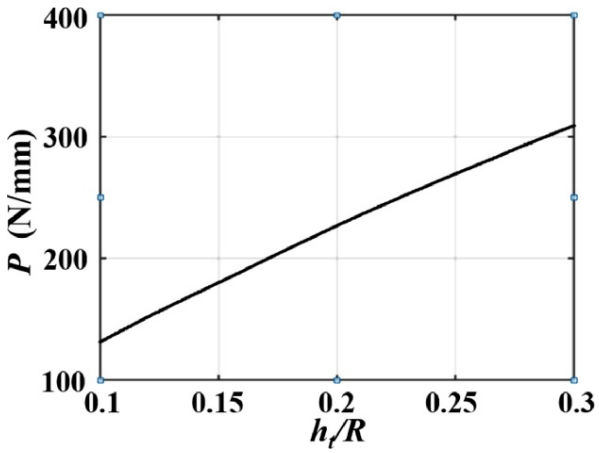

Figure 4-5 Simultaneous *in situ* indentation load measurement for copper.

4.3.4 Expanding Cavity Model

4.3.4.1 Conventional Expanding Cavity Model

The deformation regions occurring in circular indentation for conventional ECM models are shown in Figure 4-6(a). From the figure, three distinct deformation regions are observed in the work material at various depths of indentation h. In direct contact with the indenter is a hydrostatically pressurized deadzone of radius a, where a is given by the distance from the intersection between indenter centerline (Point O') and free surface to the apex of the indenter-workpiece contact.

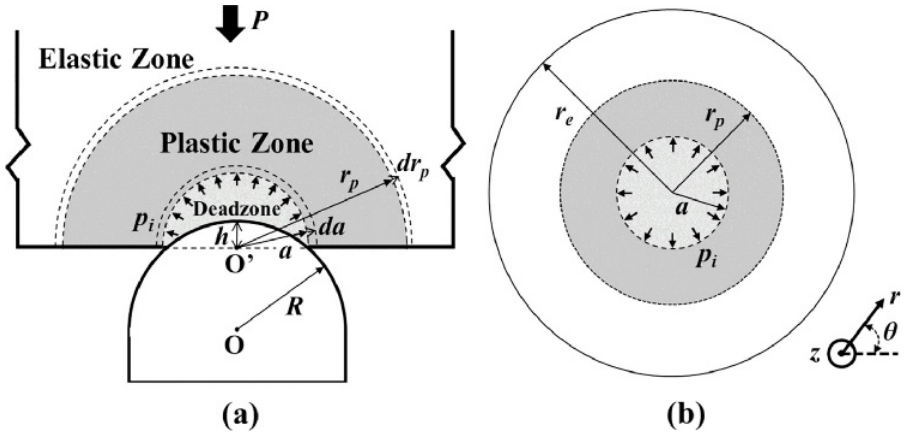

Figure 4-6 (a) Schematic of a standard ECM formulation for a circular indentation configuration. (b) Schematic of a pressurized thick-walled cylinder model.

In the deadzone region, the work material experiences a rigid body displacement equal in direction and magnitude to that of the indenter body. In this regard, an incremental displacement of the indenter dh results in an incremental radial expansion da of the deadzone. Immediately flanking the deadzone region is an incompressible hemispherical

plastic zone located between radial extents of a and r_p. In this region, the work material plastically deforms to an extent dependent on the radial distance from the indenter body. A radial incremental expansion dr_p of the plastic zone results directly from the incremental deadzone expansion da. At distances farther from the indenter, the plastic zone is surrounded by an elastic zone wherein plastic deformation does not occur. The elastic-plastic interface is located at a radial extent of r_p from the indenter centerline.

Indentation pressure is modeled with an equivalent internal pressure p_i acting on the outer boundary of the hydrostatic deadzone core as in Figure 4-6Figure 4-6(a), which can be idealized as an internally-pressurized thick-walled cylinder as in Figure 4-6(b). For the thick-walled cylinder, plastic deformation occurring at the inner wall ($a < r < r_p$) is constrained by elastic deformation occurring at the outer wall ($r_p < r < r_e$) once the internal pressure p exceeds the yield strength. Solutions for an elastic, perfectly-plastic pressurized spherical shell were first provided by Hill [83]. Recent studies by Gao [80] extended these analytical solutions to model deformation in cylindrical shells for incompressible, isotropic strain hardening materials. For a pressurized cylindrical shell, the angular-independent displacement u in the plastic region ($a < r < r_p$) is given by Eq. 4 [80],

$$u(r) = \frac{\sqrt{3}}{2}\frac{\sigma_y}{E}\frac{r_p^2}{r} \tag{4}$$

where σ_y and E are the yield stress and Young's modulus of the work material, respectively, and r, r_p and a are the radial location, the elastic-plastic interface radius and

the hydrostatically pressurized core radius, respectively. The subsurface strain distribution in the plastic region ($a < r < r_p$) is derived from the local material displacement components and is given by Eq. (5) [80],

$$\varepsilon_r = -\frac{\sqrt{3}}{2}\frac{\sigma_y}{E}\frac{r_p^2}{r^2}, \varepsilon_\theta = -\varepsilon_r, \varepsilon_z = 0 \tag{5}$$

where r, θ and z are three directions in the cylindrical coordinate system.

For strain hardening materials following power law hardening, constitutive response is given by $\sigma_e = K\varepsilon_e^n$, where σ_e and ε are the effective von Mises stress and von Mises plastic strain, respectively, and n is the strain hardening exponent. The internal pressure for the cylindrical shell is determined by integration of the stress field from the deadzone to the elastic plastic boundary and is given by Eq. (6) [80],

$$p_i = \frac{\sigma_y}{\sqrt{3}}\left[\left(1 - \frac{r_p^2}{r_e^2}\right) + \frac{1}{n}\left(\frac{r_p^{2n}}{a^{2n}} - 1\right)\right] \tag{6}$$

where r_e, r_p, a and n are, respectively, the outer radius of cylinder, radius of elastic-plastic boundary, radius of inner cylinder and strain hardening exponent. When the size of the deformation zone is negligible compared with the sample size, the outer boundary of the elastic region can be reasonably assumed to be infinite [84]. In this case, the internal pressure is given by Eq. (7),

$$p_i = \frac{\sigma_y}{\sqrt{3}}\left[1 + \frac{1}{n}\left(\frac{r_p^{2n}}{a^{2n}} - 1\right)\right] \tag{7}$$

In the ensuing analysis, the evolution of the deformation field in circular indentation is modeled using an ECM formulation. The ECM formulation is calibrated based on experimental observations of the deformation zone geometry, including the shape and location of the deformation zone and the nature of the free surface during indentation.

4.3.4.2 Calibrated Expanding Cavity Model

The experimentally observed deformation fields of the present study differ from the idealized configuration in Figure 4-6 in terms of the location of the deadzone and the character of the free surface. From the DIC-obtained velocity and strain rate fields for both copper and lead, as in Figure 4-7, the location of the deadzone (highlighted in gray) is centered above the free surface, contrary to that of a conventional ECM formulation wherein the deadzone is centered on the free surface of the workpiece.

The contact angle α between the boundaries of the deadzone and indenter was measured and is defined by two orientations at the contact location, the tangential direction *T* and the deadzone direction *N*, as in Figure 4-8(a) and (b). Figure 4-8(c) shows the evolution of α as a function of normalized indentation depth, where α was shown to remain approximately 90° during the indentation process. This can be compared with modeling predictions of the deformation field made using a conventional ECM, which predicts a decreasing contact angle at greater indentation depth. In the ensuing, we consider the calibration of an expanding cavity model that more closely matches the experimentally

measured deformation fields. The new expanding cavity model is compared with the classical solution based on predictions of the deformation parameters and the indentation load.

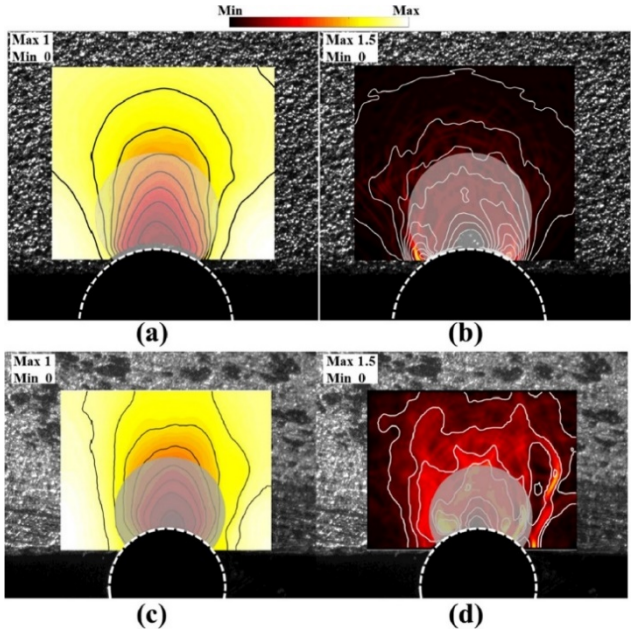

Figure 4-7 (a) Velocity distribution contour and (b) strain rate distribution contour plots measured at normalized indentation depth (h_r/R) = 0.190 for copper. (c) Velocity distribution contour and (d) strain rate distribution contour plots measured at normalized indentation depth (h_r/R) = 0.292 for lead.

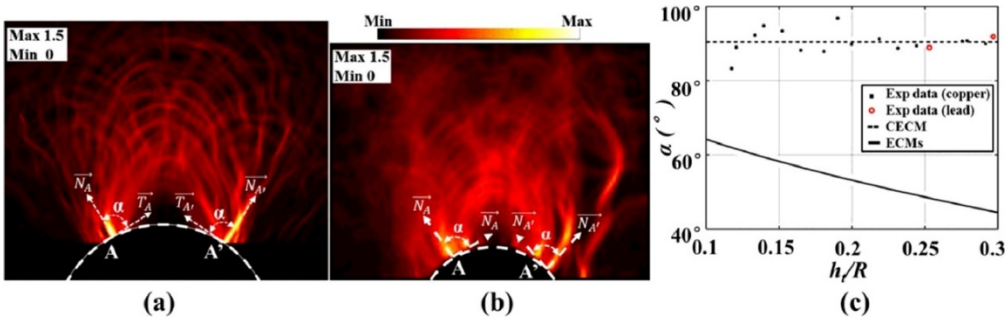

Figure 4-8 Schematic of deadzone contact angle and strain rate field at normalized indentation depth (a) (h_r/R) = 0.279 for copper and (b) (h_r/R) = 0.292 for lead. (c) Comparison of experimental and model predictions of deadzone contact angle as a function of normalized real indentation depth.

The expanding cavity model is modified based on the experimental observations as in Figure 4-7(a). First, the deadzone and elastic-plastic interface are centered at point O', located within the workpiece interior. The position of point O' is defined by the geometric assumption that the deadzone boundary is oriented normal to the indenter surface at point A, such that $AO' \perp AO$, consistent with experiment observations of Figure 4-8. As in conventional ECM approaches, the deadzone expands to accommodate material displaced by the indenter and is bounded by the indenter size ($a < R$). Second, sinking-in of the workpiece surface is incorporated, wherein the theoretical indentation depth h_t is controlled a priori and the material responds to yield an effective indentation depth h_r. The corresponding theoretical and effective projected contact lengths are r_t and r_r, respectively. The latter can be determined from the geometry of the zone in Figure 4-9(a) for $\triangle ABO$ as in Eq. (8),

$$r_r = \sqrt{R^2 - (R - h_r)^2} \tag{8}$$

The radius of the deadzone can be determined similarly from △AOO′ and △AO′B as in Eq. (8),

$$a = |AO'| = \frac{|AO||AB|}{|AO|} = \sqrt{2Rh_r - h_r^2}\frac{R}{R - h_r} \tag{8}$$

where the limiting condition of $a < R$ restricts $h_r < 0.29R$. In comparison, the deadzone size in classical ECM solutions for circular indentation [79,80] is given by the theoretical depth of indentation and the indenter geometry as $a = r_t = \sqrt{2Rh_t - h_t^2}$.

The deformation field is modeled based on the plastic response of an internally pressurized cylinder, as in prior ECM solutions [79,80]. Due to incompressibility of the work material, the volume of material displaced by the indenter is accommodated by a corresponding volumetric radial expansion of the deadzone, which is given by $dV_{indenter} = dV_{deadzone}$. The incremental volume displaced by the indenter is given by the real indentation depth (h_r) and the actual contact length (r_r) as in $dV_{indenter} = 2r_r dh_r$, where r_r is given by Eq. (8). The incremental volumetric increase of the deadzone is determined by the incremental expansion of the deadzone boundary as in Eq. (9),

$$dV_{deadzone} = 2\pi a\frac{2\pi - 2\theta}{2\pi}du|_{r=a} = 2(\pi - \theta)adu|_{r=a} \tag{9}$$

where θ is defined by △AO′B and $du|_{r=a}$ is given by differentiation of Eq. 4 as in Eq. (10),

$$du|_{r=a} = \frac{\sqrt{3}\sigma_y}{E}\frac{r_p}{r}dr_p|_{r=a} \tag{10}$$

Substituting terms and simplifying this expression of $dV_{indenter} = dV_{deadzone}$ can be rewritten as in Eq. (11),

$$\frac{\sqrt{2Rh_r - h_r^2}}{\pi - sin^{-1}\left(1 - \frac{h_r}{R}\right)}dh_r = \frac{\sqrt{3}\sigma_y}{E}r_p dr_p \tag{11}$$

Normalizing length terms in Eq. (11) by indenter radius (R) yields Eq. (12),

$$f\left(\frac{h_r}{R}\right) = \frac{\sqrt{3}\sigma_y}{E}\frac{r_p}{R}d\left(\frac{r_p}{R}\right) \tag{12}$$

where,

$$f\left(\frac{h_r}{R}\right) = \frac{\sqrt{2\frac{h_r}{R} - \left(\frac{h_r}{R}\right)^2}}{\pi - sin^{-1}\left(1 - \frac{h_r}{R}\right)}d\left(\frac{h_r}{R}\right) \tag{13}$$

Integrating both sides of Eq. (12) yields Eq. (14),

$$F\left(\frac{h_r}{R}\right) = \frac{\sqrt{3}}{2}\frac{\sigma_y}{E}\left(\frac{r_p}{R}\right)^2 \tag{14}$$

The left side of this expression can be determined by integration of Eq. (13), as in $F\left(\frac{h_r}{R}\right) = \int f\left(\frac{h_r}{R}\right)d\frac{h_r}{R}$. For this purpose, a numerical integration was used and a power law fit according to $F(x) = ax^b$ yielded the numerical result of $F(hr/R)$, as in Eq. (15),

$$F\left(\frac{h_r}{R}\right) = 0.3556\left(\frac{h_r}{R}\right)^{1.360} \tag{15}$$

This resulted in an R^2 = 0.99 where the terms a and b describe the evolution of the deadzone. Combining terms, the radius of the elastic-plastic interface r_p as a function of normalized real indentation depth h_r/R is given by Eq. (16),

$$r_p = R\sqrt{\frac{E}{\sigma_y}\left[0.4106\left(\frac{h_r}{R}\right)^{1.36}\right]} \tag{16}$$

For copper (E = 119 GPa, σ_y = 125 MPa), the local material displacement can be determined by substituting the new r_p into Eq. 4,

$$u(r) = \frac{R^2}{r}\left[0.3556\left(\frac{h_r}{R}\right)^{1.36}\right] \tag{17}$$

Deformation parameter estimates for the calibrated ECM (CECM) formulation were directly compared with the standard ECM formulation [80] and experimental DIC results for the circular indentation configuration in Figure 4-9(b). As Figure 4-9(b) shows, the standard ECM formulation predicts the normalized maximum strain rate increasing monotonically from 2 to 4 as indentation depth increases. This is not in general agreement with the experimental data which shows that normalized maximum strain rate is relatively constant around 1 for both copper and lead. In comparison, the calibrated ECM produces a clearly better estimate of normalized maximum incremental strain in the subsurface field.

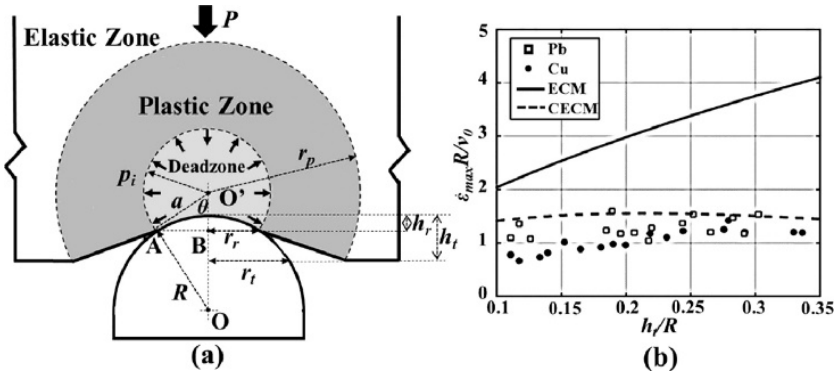

Figure 4-9 (a) Schematic of calibrated expanding cavity model. (b) Comparisons of experimental measurement and ECM-based predictions of normalized maximum effective strain rate as a function of normalized indentation depth for copper and lead.

The loading response during cylindrical indentation is akin to that of a hydrostatically pressurized cylinder at constant pressure, p_i, given by Eq. (6) and uniformly distributed along the deadzone boundary, as is shown in Figure 4-10(a). In this configuration, the indentation load is given by the total resultant force caused by the hydrostatic pressure along the deadzone boundary. Due to the symmetry of the deadzone, only pressure applied along SS′ contributes to the total force as in Eq. (18),

$$F = 2a\int_0^{\theta} p_i \cos(s)\, ds = 2ap_i \sin(\theta) \tag{18}$$

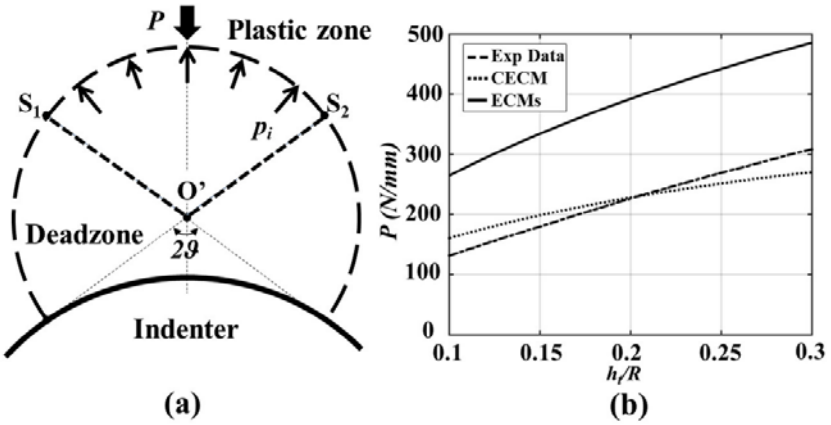

Figure 4-10 (a) Pressure distribution in the hydrostatic pressurized deadzone. (b) Comparisons of experimental and ECM-based predictions of indentation load as a function of normalized indentation depth.

The expected load from the calibrated ECM (CECM) and standard ECM formulations [79,80] are compared with the experimentally measured load response during indentation in Figure 4-10(b). From the figure, the calibrated ECM provided significantly better prediction of the indentation load when compared with the predictions made using the standard ECM formulation which over-predicts the load response. The difference in the predicted response is likely a consequence of the total effect of the traction on the deadzone boundary in the two models. As Figure 4-10(a) shows, in the calibrated model, only the pressure along SS contributes to the load response, while other pressure vectors along the deadzone boundary are ignored due to symmetry along the deadzone. In contrast, the higher expected load in the standard ECM formulations could be explained by the fact that the entire semi-circular deadzone contributes to the load response given the deformation geometry in Figure 4-6(a). The calibrated ECM gives a more accurate prediction of the

deformation occurring during circular indentation for the experimental conditions investigated. Extension of the present approach toward calibration of an ECM for spherical indentation requires direct in situ observation of the three-dimensional deformation field, which is not possible using optical-based imaging analysis. In this regard, in situ loading platforms within tomographic imaging systems may provide utility for mapping deformation and deadzone geometry of compatible material systems.

4.4 Microstructure Evolution

4.4.1 Deformation Trajectory

Strain fields were characterized within a region close to the indenter, demarcated using a white box in Figure 4-11(a). Spatially heterogeneous effective and Lagrangian strain fields developed under the indenter, reminiscent of deformation fields seen during flat punch indentation [106]. Material directly underneath the indenter at (r, λ) with $r < 20$ μm exhibited a local minimum in ε, where Figure 3-1 defines the polar coordinate system (r, λ). This region was surrounded by a zone that featured higher ε, in the vicinity of the dashed line identified in Figure 4-11(b). The intersecting location between the dashed line and the interface of the indenter at (r, λ) = (0 μm, +45°) exhibited global maxima in effective strains: ε_{max} = 4.5. Locations that developed maxima and minima are identified with black and white arrows, respectively, in Figure 4-11(b). Effective strains decayed to negligible levels at greater r.

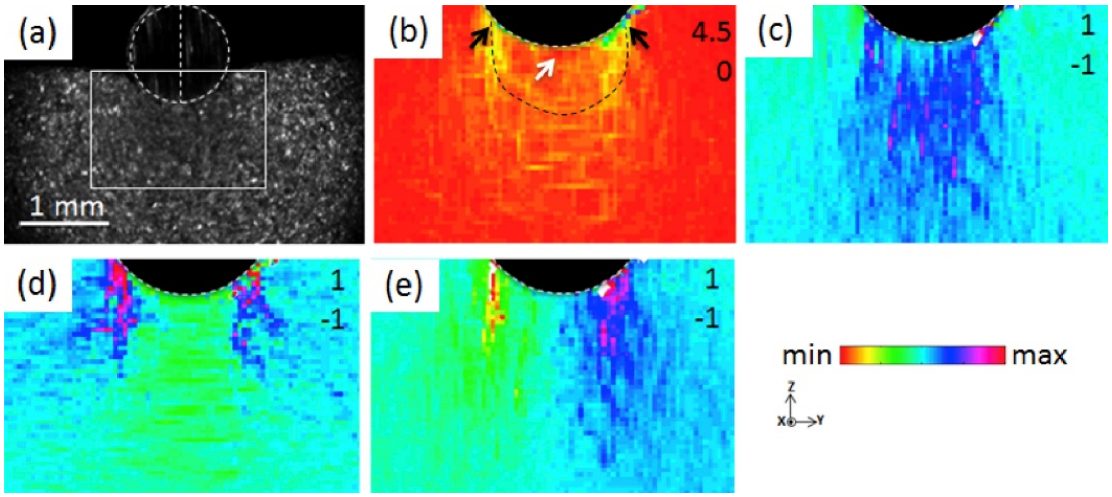

Figure 4-11 (a) Asperities on the workpiece during circular indentation for characterizing deformation history. (b) Effective strain field. Lagrangian strain tensor component fields: (c) E_{11} (d) E_{22} and (e) E_{12}. Refer insets for maxima and minima.

Evolution of Lagrangian strain tensor components with respect to indentation depth h is shown in Figure 4-12 for different locations underneath the indenter. Directly underneath the interface at (r, λ) = (r > 0 µm, 0°), where r > 0 µm, the strain histories generally featured greater shear magnitudes relative to that of tensile/compressive components. This is shown in Figure 4-12(a) in curves i, ii, iii and iv for (r, λ) = (45 µm, 0°), (51 µm, 0°), (57 µm, 0°) and (100 µm, 0°), these featuring (E_{11}, E_{12}) = (0.02, 0.1), (0.1, 0.2), (0.1, 0.1) and (0.3, 0.4), respectively. On the contrary, zones farther away from the interface exhibited comparatively lesser shear magnitudes relative to that of tensile/compressive components.

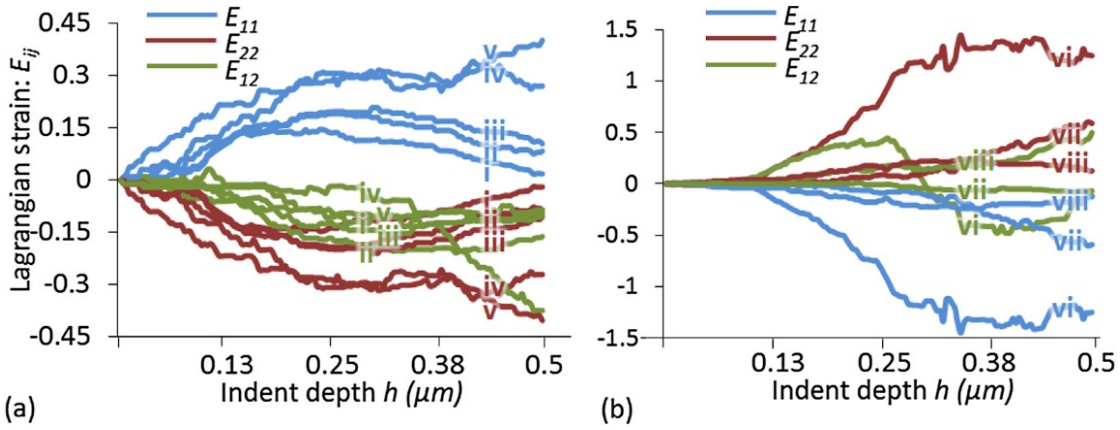

Figure 4-12 Evolution of Lagrangian strain tensor components at (r, λ) = (a) (r > 0 µm, 0°) and (b) (r > 0 µm,45°) at (i) (45 µm, 0°) (ii) (51 µm, 0°) (iii) (57 µm, 0°) (iv) (100 µm, 0°) (v) (450 µm, 0°) (vi) (50 µm, 45°) (vii) (100 µm, 45°) and ($viii$) (200 µm, 45°).

For example, curve v in Figure 4-12(a) shows the evolution of Lagrangian strain components at (r, λ) = (450 µm, 0°) with (E_{11}, E_{12}) = (0.4, 0.1). Additionally, this location featured a monotonic evolution in its strain components in contrast to the other points i-iv studied here that showed global reversals in $E_{11}$and E_{22}. Regardless of the distance from the interface, the zone directly underneath the interface experienced tensile and compressive strains along horizontal Y and vertical Z directions, respectively. Contrary to these observations, zones located along the oblique axis at (r, λ) = (r, +45°), where r > 0 µm, consistently exhibited lesser shear magnitudes in addition to monotonic variation in tensile/compressive components. This is shown in Figure 4-12(b) in curves vi, vii and $viii$ for (r, λ) = (50 µm, 45°), (100 µm, 45°) and (200 µm, 45°), these featuring (E_{11}, E_{12}) = (1.2, 0.1), (0.6, 0.5) and (0.1, 0.1), respectively. Interestingly, this zone featured reversed compressive and tensile components with respect to the zone directly underneath the indenter. The gradation in imposed strains results from heterogeneity in deformation fields

inherent to indentation. Clearly, there is a pronounced effect of the interface in governing mechanics at zones featuring small r.

4.4.2 Microstructure Response

Global heterogeneous strains imposed on the workpiece during indentation resulted in spatially graded microstructures featuring variation in grain sizes, morphologies and crystallographic textures. Equiaxed ultra-fine grained (UFG) microstructures with δ_{15° ~ 0.4 μm – 0.8 μm were seen in zones (r, λ) characterized by (r < 5 μm, 75°), (r < 20 μm, 65°), (r < 24 μm, 45°), (r < 20 μm, 37°) and (r < 9 μm, 0°), where δ_{15° refers to size of zones in the microstructure surrounded by boundaries featuring disorientation >15°. This is shown in Figure 4-13(a)-(e), wherein the center of the dashed white line corresponds to (r, λ) = (0 μm, 75°), (0 μm, 65°), (0 μm, 45°), (0 μm, 37°) and (0 μm, 0°), these corresponding to DIC-characterized strains of ε = 0.7, 1.3, 4.5, 1.3 and 1.4, respectively. It is recognized that while UFG microstructures are anticipated during imposition of severe plastic deformation (SPD) as seen at (r, λ) = (0 μm, 45°) with ε > 4, Figure 4-13(a), (b), (d) and (e) indicate anomalous grain refinement with UFG microstructures present after low ε < 1.5. Radially outwards with respect to the indenter and farther away from its interface at (r, λ) = (35 μm, 65°) and (20 μm, 45°), the microstructures exhibited a strongly graded character in which the grain size increased from UFG to microcrystalline sizes with δ_{15° > 1 μm. The corresponding microstructures are shown in Figure 4-14(a) and (b), DIC characterization resulting in ε = 1 and 1.7 in these zones, respectively. At increasing distances from the indenter, the microstructure consisted of pancake-shaped grains with serrated boundaries. The major axis of these grains was found to be parallel to the face of

the indenter. Examples of such microstructures are shown in Figure 4-14(c) and Figure 4-15(a) characterized at (r, λ) = (35 µm, 45°) and (50 µm, 45°), corresponding to ε = 1.3 and 1.5, respectively. The microstructure eventually merged with pristine undistorted grain characteristics featuring large equiaxed grains with δ_{15° > 50 µm, this also accompanied by falling levels of ε as shown in Figure 4-15(b) for (r, λ) = (300 µm, 0°), respectively.

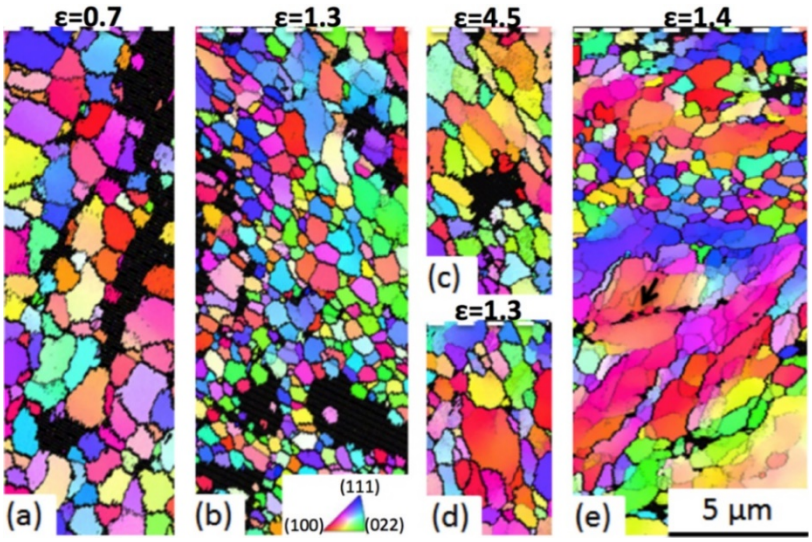

Figure 4-13 Orientation imaging microscopy using electron back scattered diffraction of the zones close to the interface of the indenter at (r, λ) = (a) (0 µm, 75°), (b) (0 µm, 65°), (c) (0 µm, 45°), (d) (0 µm, 37), and (e) (0 mm, 0°). Black arrow in (e) shows cube-oriented transition band. Dashed white line demarcates interface of the indenter.

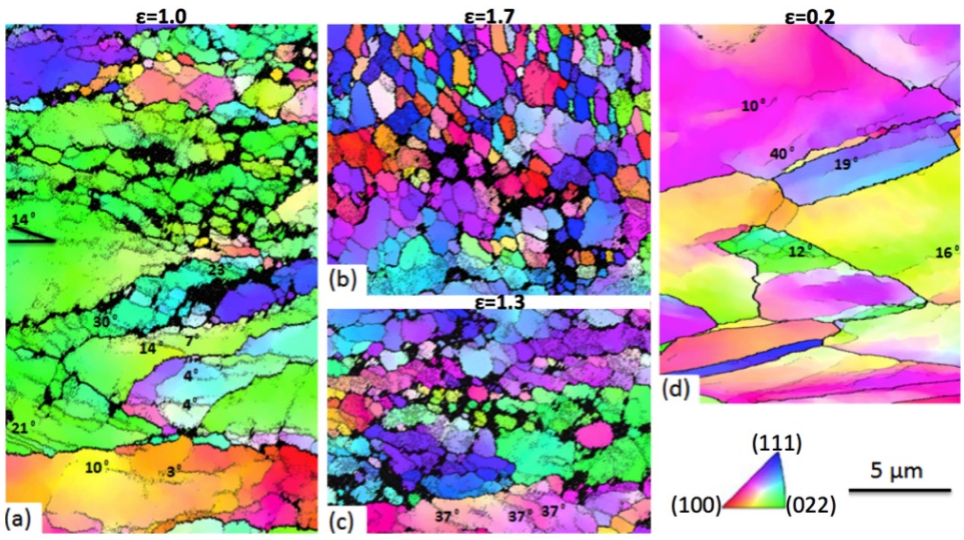

Figure 4-14 Orientation imaging microscopy using electron back scattered diffraction of the zones close to the interface of the indenter at (r, λ) = (a) (35 µm, 65°), (b) (20 µm, 45°), and (c) (35 µm, 45°) (d) (100 µm, 0°).

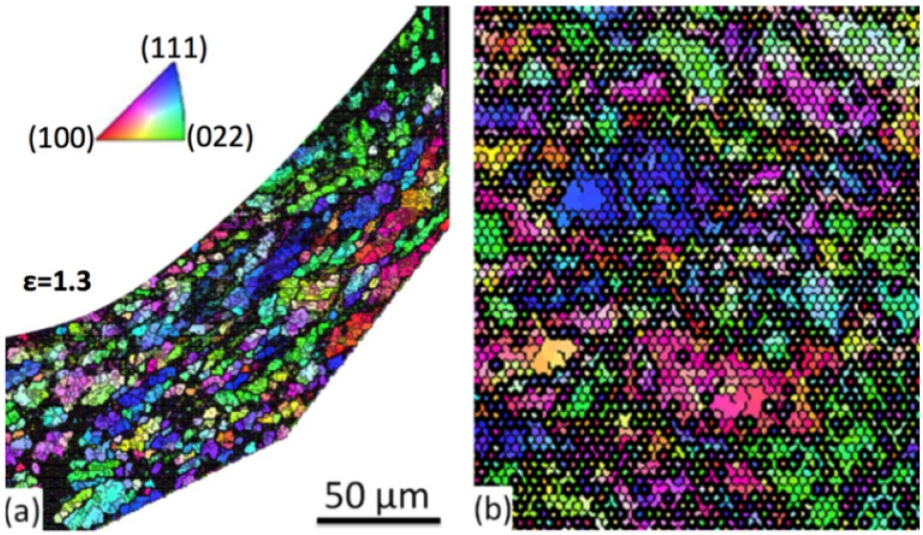

Figure 4-15 Orientation imaging microscopy using electron back scattered diffraction of the zones close to the interface of the indenter at (r, λ) = (a) (50 µm, 45°) (b) (300 µm,0°).

It was seen that intragranular dislocation boundaries with disorientation > 2° in regions beyond the recrystallized UFG zones had a well-defined local directionality. Herein, clusters of similarly oriented boundaries were seen, featuring orientations ranging from near parallel: +5°, to heavily off-parallel: +40°, with respect to the tangent of the indenter. These angles are labeled in Figure 4-14(a), (c), and (d). Directionality in dislocation boundaries generally results from crystallographic curvature induced by strain gradients [107]. Influence of strain gradients was characterized by numerical quantification of the plastic spin tensor using results obtained by DIC of the deformation field. To this end, the curl of the plastic strain tensor, given by Ref. [107]: $\chi_{ni}^{pl} = e_{nkj}E_{ij,k}^{pl}$ was calculated, where e_{nkj} is the permutation operator and $E_{ij,k}^{pl}$ is the spatial derivative of Lagrangian strain tensor components. Subsequently, the magnitude of the curl was found numerically, using: $\chi_e = \sqrt{\frac{2}{3}\chi_{ij}^{pl}\chi_{ij}^{pl}}$ whereby the dislocation density contribution $\rho_{SG} = \frac{\chi_e}{b}$ was estimated. Here b refers to the magnitude of the Burgers vector. This method resulted in small $\langle\rho_{SG}\rangle \sim 10^{13}$ m^{-2}, implying that the aforementioned dislocation clusters resulted from local strain gradients as opposed to those imposed globally on the workpiece during indentation.

Interestingly, a progressive decrease in spacing between dislocation boundaries accompanied by a decrease in grain size was seen within zones leading to the interface of the indenter. Grain boundary spacing characterized by the line intercept method using OIM data yielded δ_{2° = 0.7 μm, 0.4 μm, 0.67 μm and 1.5 μm, 0.83 μm, 1.4 μm near the top edge and bottom edge of Figure 4-14(a)-(c), respectively. Along with serrated boundaries in elongated grains at larger radial distances, these observations suggest onset of continuous

and geometric dynamic recrystallization (CDRX/GDRX) [44]. To this end, the grain orientation spread (GOS) was calculated to delineate onset of CDRX and GDRX [32]. Grain orientation spread is given by $GOS = \frac{1}{N-1}\sum_{i=1}^{n}\sum_{j=1}^{n}\Delta g_{ij}\left(g_i + g_j\right)$ and refers to spread in orientation (Δg_{ij}) within grains containing n OIM characterized points. This spread is a consequence of the evolution of dislocation-based geometrically necessary boundaries (GNBs) arising from global and local strain gradients [44]. Upon imposition of strains and through the progression of recrystallization, the disorientation across the GNBs increases, resulting in a concomitant rise in the GOS. Following grain fragmentation by CDRX or GDRX, defect-free grains with low intra-grain misorientations develop, at which point recrystallization is generally considered to have occurred [15,44,108]. GOS parameters calculated from the micrographs consistently resulted in low area averaged values of 1.0°±0.5°, 1.1±0.9°, 1.4±0.8°, 1.88°±1.1°, and 2.3±2° in the vicinity of the indenter at locations corresponding to Figure 4-13(a)-(e), respectively. However, GOS increased to higher values > 6° at increasing distances from the indenter. For instance, GOS = 6.3±2.4° and 5.8±2:5° were seen at (r, λ) = (35 µm, 65°) and (35 µm, 45°), the corresponding OIM micrographs are provided in Figure 4-14(a) and (c), respectively. A GOS < 2.6° conforms to the previously calibrated threshold that signifies complete recrystallization in OFHC Cu [108], bolstering the claim that CDRX and GDRX have taken place within regions close to the indenter interface. On the other hand, higher GOS indicates incomplete/progressing recrystallization, expected in regions with lower strain levels farther away from the interface.

4.4.3 Crystallographic Texture Evolution

Crystallographic textures in microstructures resulting from circular indentation were extracted from OIM of the workpiece. This was done for regions located at (r, λ) = (0 µm, 0°), (300 µm, 0°), and (50 µm, -45°), as shown in Figure 4-16(a)-(c), respectively. The corresponding OIM micrographs are shown in Figure 4-13(e), Figure 4-15(a)-(b), respectively. From the figure, it is clear that dissimilar textures developed in these regions, reflective of spatially heterogeneous deformation histories in the workpiece during indentation. For instance, empirically obtained textures close to the interface between the indenter and workpiece at (r, λ) = (0 µm, 0°) featured strong cube texture components. Strong and concentrated cube textures featuring high $f(g_{cube})$ (>10) are often seen after hot rolling in medium to high stacking fault energy metals such as Cu and Al [33]. However, unlike in hot rolling, crystallographic textures here feature low and diffuse cube textures with $f(g_{cube}) \sim 5$. In comparison, crystallographic textures farther away from the indenter at (r, λ) = (50 µm, -45°) and (300 µm, 0°) revealed characteristics typical of pure shear (cold rolling) and simple shear. These characteristics comprise three dominant fibers demarcated in Figure 4-16(b) and (c) using black arrows. Cube textures were only found in a small region directly underneath the indenter with the rest of the workpiece featuring shear-type textures, evidenced by OIM-based characterization and numerical simulation using the VPSC framework. Textures originating from ambient deformation processes are often reflective of the prevalent geometry of deformation. Contrasting textures between regions close to the interface and those farther away therefore suggest contrasting deformation geometries between these regions.

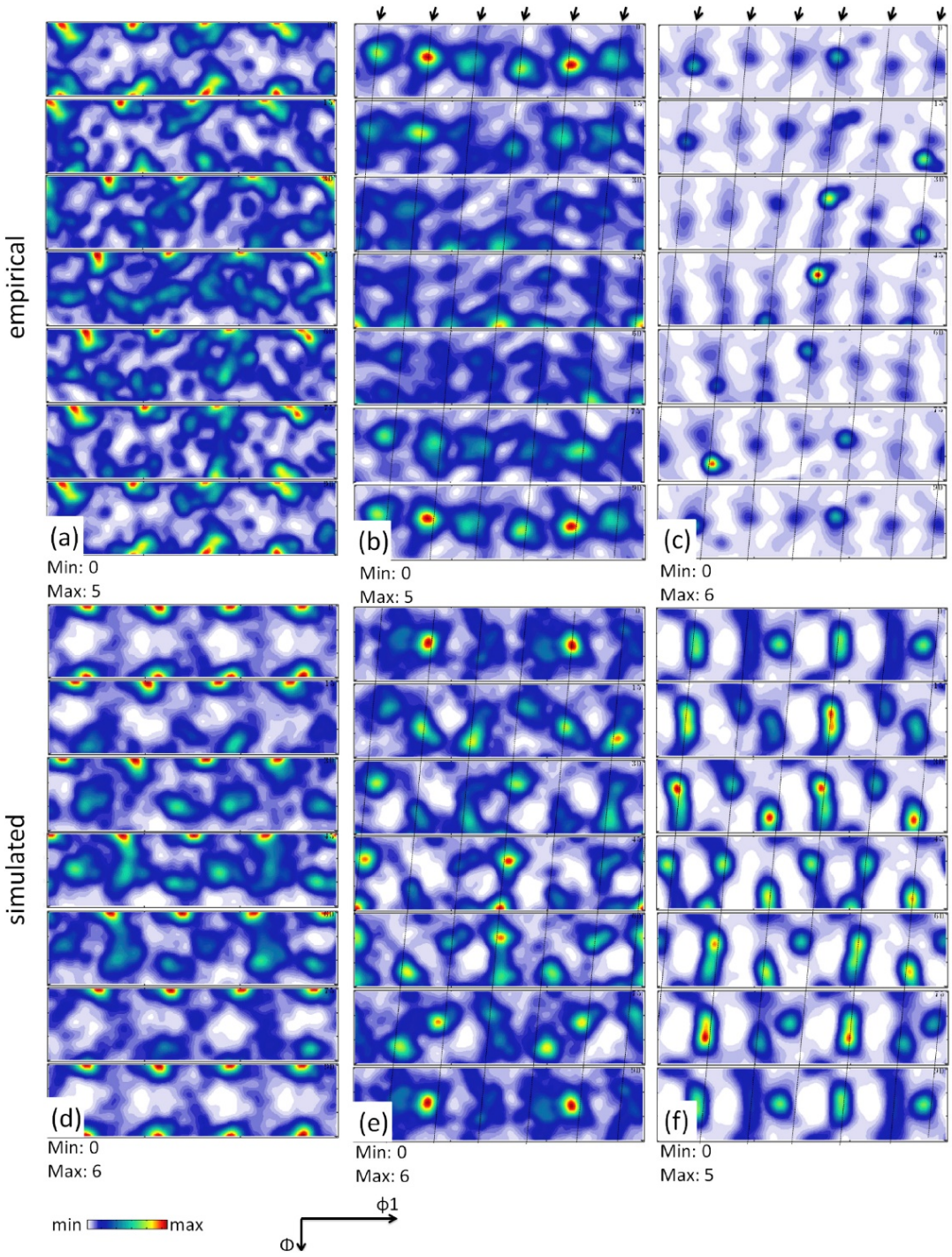

Figure 4-16 Empirically obtained orientation distribution functions at (r, λ) = (a) (0 μm, 0°) (b) (300 μm, 0°) (c) (50 μm, -45°). (d)-(f) Corresponding counterparts simulated using DIC + VPSC. Black arrows show locations of fibers in crystallographic textures.

4.5 Discussion

Microstructures obtained from indentation showed a gradation in material response consisting of a completely recrystallized UFG microstructure near the interface, compared with microcrystalline grains featuring increasing δ_{15° at larger r. A gradation was also seen in the associated crystallographic textures that were predominantly cube-oriented directly underneath the interface, compared with shear-type textures elsewhere in the deformation zone. DIC-based characterization of the flow field showed low ε close to the indenter interface, this unexpected given that grain refinement in this zone resulted in the formation of an UFG microstructure. Mechanics of graded microstructure evolution including potential sources of this anomalous accelerated grain refinement are discussed in the ensuing.

Previous investigations on microstructure response during imposition of SPD [108–110] have shown that Cu exhibits a gradual progression of CRDX/GDRX during imposition of strains in which UFG microstructures with δ_{15° < 0.5 μm are seen when ε > 4. CDRX and GDRX are dislocation plasticity based and morphologically driven mechanisms of grain refinement [15]. CDRX involves formation of grain boundaries that progressively increase in disorientation with respect to imposed effective strains [44]. In this manner, progressively smaller defect-free zones completely surrounded by boundaries featuring disorientation > 15° are formed, constituting dynamic recrystallization. On the other hand, GDRX involves pancaking of the grains due to imposed shear strains accompanied by serration of boundaries [15]. When the length scales associated with serrations matches the saturation grain size corresponding to the prevalent

thermomechanical conditions characterized by the ($\dot{\varepsilon}$, ε, T) triad, where T is the temperature, the pancake-shaped grain pinches off into several smaller grains [15,108].

Unlike the expected behavior in CDRX and GDRX, the present experimental results revealed formation of UFG microstructures at low ε, this suggesting activation of additional mechanisms that accelerate CDRX/GDRX. Progression of recrystallization within heavily recrystallized zones was characterized as the fractional length of high angle grain boundaries (HAGB) [108]: $f_{rx} = \frac{l_{HAGB}}{l_{HAGB}+l_{LAGB}}$, where l_{HAGB} and l_{LAGB} are lengths of high (θ > 15°) and low (2° < θ < 15°) angle grain boundaries, respectively. Heavily recrystallized microstructures constituting defect-free grains exhibit high f_{rx} parameters due to sparse presence of low disorientation dislocation structures featuring θ < 15°. A high f_{rx} > 0.9 was found within zones close to the indenter interface, revealing heavily recrystallized grains despite low effective strains. First order predictions of f_{rx} using DIC-based characterization of (ε, $\dot{\varepsilon}$) = (1.5, 0.1 s^{-1}), coupled with phenomenological models for predicting progression of CDRX/GDRX described in ref. [108], resulted in small recrystallization fractions f_{rx} < 0.1 close to the indenter interface.

A likely source of this variability might be found in interface friction affecting material response. Contribution from friction to ε was estimated numerically using finite element methods in Abaqus by simulating tribological conditions featuring coefficient of friction μ = 0.4 and sticking friction. The latter is a numerically-implemented feature that mimics sticking friction conditions by prohibiting sliding upon first contact. Plane strain simulations using the CPE4 element with plane strain thickness (t = 1 m) were implemented. The isothermal Johnson-Cook material model was used for simulating response of the workpiece during indentation. The indenter was modeled as a rigid body

with R = 0.5 mm and v = 0.1 mm·s^{-1}. Figure 4-17 shows the post-indentation mechanical state of the workpiece simulated using the two tribological conditions. An effective strain field qualitatively similar to the empirically observed field developed in the workpiece and featured two maxima at (r, λ) = (0 µm, +45°). Numerically-simulated maxima in ε were seen to vary proportionately with respect to coefficient of friction with ε ~ 3 for μ = 0.4, compared with ε ~ 5.6 for $\mu \gg 0.4$ (sticking). Further, the mechanical state of material directly underneath the indenter was similar in the two cases featuring small $\left\|\underline{E}^{pl}\right\|$ ~ 0.05 at (r, λ) = (45 µm, 0°), decreasing to ~ 0.03 at (10 µm, 0°). These locations are pointed out using white arrows in Figure 4-17. The similarity in effective strains despite contrasting friction conditions indicates that enhanced straining and accelerated recrystallization near the interface were not caused by friction effects.

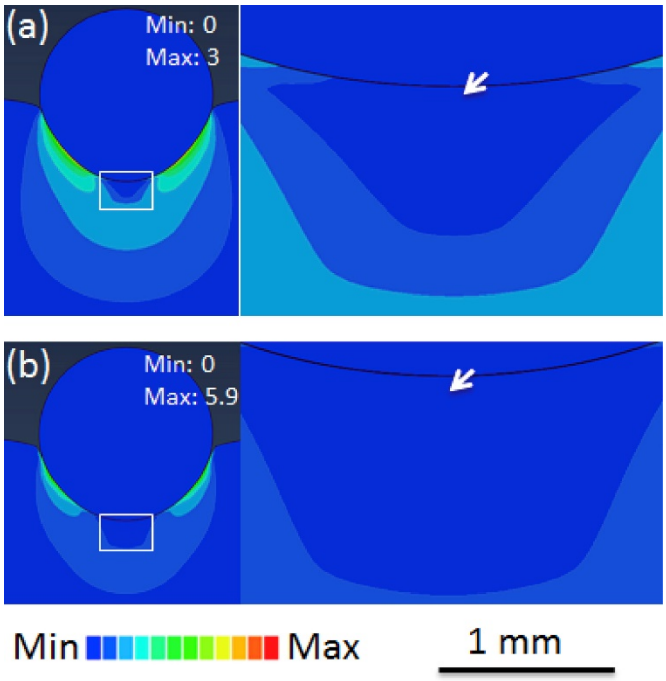

Figure 4-17 Numerically calculated effective strain ε fields obtained from circular indentation with (a) µ = 0.4 and (b) sticking friction conditions. The scale bar corresponds to the insets on the left. White arrow indicates location (r, λ) = (10 µm, 0°).

Rate of microstructure evolution and grain refinement with respect to imposed thermomechanical conditions has been shown elsewhere to be a function of heterogeneity in strain paths involving strain path changes and reversals [54,55]. Accommodation of strain heterogeneity can accelerate microstructure evolution by instigating dislocation slip in secondary systems and concomitantly enhancing local lattice rotation rate $\dot{\Theta}$. This behavior has been observed during heterogeneous straining of material in the C route of ECAP, compared with that of rolling [54]. The former features significant local and global strain path changes in contrast to monotonic strain history in the latter. This results in enhanced microstructure evolution with more $-ve\frac{\partial \delta}{\partial \varepsilon}$ and smaller grain sizes at similar effective strains $\varepsilon \sim 1$ during ECAP with $\delta_{15^\circ} \sim 1$ μm, compared with rolling with $\delta_{15^\circ} \sim$ 2.5 μm. The influence of the strain path can be quantified by measuring the total local lattice rotation Θ resulting from strain path changes [54]. This was achieved numerically in the present study using the VPSC framework. Herein, mechanical response and microstructure evolution in two zones A and B located at (r, λ) = (45 μm, 0°) and (100 μm, 0°), respectively, were investigated. These zones experienced similar effective strains $\varepsilon \sim 1.5$ at the end of the indentation experiment. Further, both zones A and B exhibited non-monotonic strain evolution with several local maxima in Lagrangian strain tensor components $\left|E_{ij}^{pl}\right|$. These strain histories are shown in curves (i) and (iv) in Figure 4-12(a), respectively. However, zone A featured a stronger globally non-monotonic behavior involving reversals in E_{11} and E_{22}. In this regard, a final $\underline{E}^{pl} = \begin{bmatrix} 0.02 & -0.10 \\ -0.10 & -0.02 \end{bmatrix}$ and $\left\|\underline{E}^{pl}\right\| \sim 0.14$ was seen in zone A, where $\left\|\underline{E}^{pl}\right\|$ was calculated as $\left\|\underline{E}^{pl}\right\| = \sqrt{\frac{2}{3}E_{ij}^{pl}E_{ij}^{pl}}$. Zone B featured a final $\underline{E}^{pl} = \begin{bmatrix} 0.35 & -0.21 \\ -0.21 & -0.35 \end{bmatrix}$ and $\left\|\underline{E}^{pl}\right\| \sim 0.44$.

Figure 4-18(a) shows the local lattice rotation rate $\dot{\Theta}$ obtained within zones A and B. Both zones exhibited non-monotonic $\dot{\Theta}$ with respect to imposed ε and zone A generally featured higher $\dot{\Theta}$ compared with zone B at any ε. Integration of rotation rate over the respective material trajectories to estimate accumulated local lattice rotation angle Θ resulted in ~ 7.5° and ~ 5.2° in zones A and B, respectively, as in Figure 4-18 (b). Higher final Θ in zone A highlights the general trend that presumably resulted in higher dislocation density ρ in regions close to the indenter. Higher ρ would result in accelerated refinement close to the interface, this contributing to formation of UFG microstructures at low strains ε < 1.5. It is interesting to note that the variability in final Θ exists without globally imposed strain path changes like those present in ECAP processing. This indicates a prevalence of micro-scale strain path changes close to the interface during indentation that resulted in enhanced accelerated grain refinement.

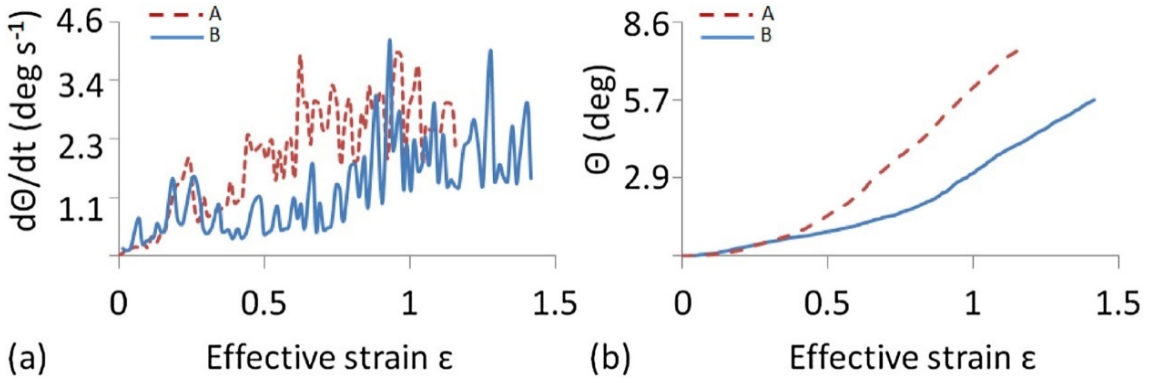

Figure 4-18 (a) Lattice rotation rates $\dot{\Theta}$ vs. effective strains ε. (b) Total lattice rotation imposed Θ vs. effective strains ε in zones A: (r, λ) = (45 µm, 0°) and B: (r, λ) = (100 µm, 0°).

Higher resolution investigations of DIC-characterized pathlines resulting from plastic flow during indentation revealed the presence of micro-bends. These micro-bend features are reminiscent of non-laminar pathlines seen in recent studies on unconstrained plastic deformation in wear tests [111,112]. These bends were characterized by quantifying the associated bend angle α within the pathline during indentation with respect to normal distance of the bend from the surface of the indenter r, where α is identified in Figure 4-19 (a). The spatial frequency of bend angles captures the probability of anomalous physical path changes within pathlines of material points during indentation. Figure 4-19(b) shows that zones closer to the interface of the indenter exhibited a significantly higher frequency of bends featuring $\alpha > 80°$. The frequency of bends was ~ 0.079 at zone A which is at 45 μm from the interface of the indenter, nearly four times greater than that seen at zone B ~ 0.020 at a distance 100 μm. The frequency dropped to ~ 0.004 at a distance of 140 μm with respect to the interface. It was seen that spatial bends in the pathlines featuring large α resulted in proportionately high $\dot{\Theta}$. This is shown for zones A and B in Figure 4-19 (c), wherein a direct proportionality between α and $\dot{\Theta}$ is observed. High $\dot{\Theta}$ corresponding to high local lattice rotation rate eventually accumulated to higher Θ as evidenced in Figure 4-17 for zone A, compared with zone B.

Recent investigations have shown that material flow during unconstrained plastic deformation in geometries (e.g., surficial sliding) follows non-laminar streamlines [111,112]. These streamlines exhibit anomalous bends/folds and have been shown to emerge within zones close to the surface during plastic flow in wear tests. Additionally, dimensions associated with these bends have been shown to scale with δ_{15°. Origins of such non-laminar flows were found in the differential deformation occurring between hard

and soft crystal orientations as predicted by the Bishop-Hill criterion [112]. However, the crystal plasticity implications of these anomalies in streamlines remain to be investigated.

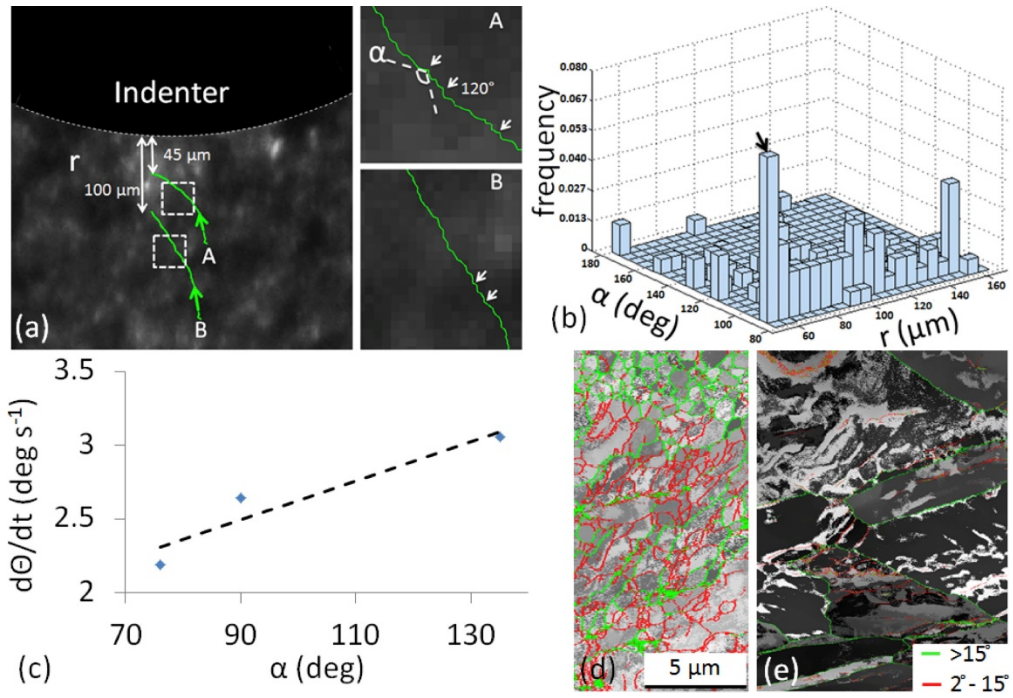

Figure 4-19 (a) Pathlines in zones A and B showing non-laminar features (white arrows in insets). (b) Spatial (bivariate) distribution of non-laminar features characterized by bend angle α and distance from interface of the indenter r. (c) Proportionality between $\dot{\Theta}$ and α. $\dot{\Theta}$ was calculated using the VPSC framework. Taylor factor fields for zones at (r, λ) = (d) (0 µm, 0°), (e) (100 µm,0°).

To this end, zones featuring relatively hard and soft orientations during indentation were characterized by quantifying the Taylor factor M fields of the microstructure directly underneath the indenter close to its interface. This was done by characterizing the deformation gradient tensors $\underline{F}$ in zones A and B and inputting the tensors to the TSL OIM

software. A lower M corresponds to a softer orientation in which globally imposed strains are accommodated by smaller levels of dislocation slip [113]. Figure 4-19(d) and (e) show that zones A and B exhibit several hard and soft orientations featuring high and low M, respectively. These zones were seen to be often demarcated by dislocation structures featuring $\theta > 2°$. However, within the same grain, several zones featuring similar M were seen wherein δ_{2° provides an upper bound for dimensions associated with these zones dM. Closer to the interface of the indenter at (r, λ) = (45 μm, 0°), these zones exhibited δ_M ~ 0.4 μm. However, farther away at (r, λ) = (100 μm, 0°), these zones exhibited a larger δ_M > 1.5 μm. Dislocation structures are known to result in spatial stress fluctuations and screening, even in the presence of globally homogeneous stress fields. Such structures can result in gradients in plastic strain tensors that in turn can result in enhanced lattice rotations.

4.6 Conclusion

In this chapter, *in situ* observations were made of deformation occurring during circular indentation of OFHC copper and lead. Characteristics of the deformation field as they pertain to actual indentation depths, incremental displacement fields, strain rate fields and strain fields were elucidated using a DIC-based imaging approach. The DIC-based approach provided accurate assessments of the deformation zone geometry in terms of the location and size of the deadzone prevailing during indentation. These experimental results were utilized to calibrate the deformation configuration for an expanding cavity model with a modified overall configuration of the deadzone boundary, elastic-plastic interface and nature of the free surface. The calibrated expanding cavity model was shown to provide

better estimates of the deformation in terms of maximum effective strain rate and indentation load for the experimental conditions investigated. The present results provide a useful experimental framework for validating other analytical models based on direct in situ observations of the deformation field. In addition, the material response and microstructure evolution of OFHC Cu during indentation was studied. It was shown that evolution of microstructures and crystallographic textures close to the interface of the indenter followed locally-altered routes. Microstructure response featured accelerated refinement with more $-ve\frac{\partial \delta}{\partial \varepsilon}$ that resulted in the formation of an UFG microstructure at low effective strains ε < 1.5. The origins of these phenomena were delineated by characterizing indentation strain fields using DIC and coupling these flow field measurements with EBSD-based OIM. In this regard, it was determined that the UFG microstructure close to the interface of the indenter evolved from continuous recrystallization processes. Thereafter, evolution of the UFG microstructure was linked to enhanced local lattice rotation rate associated with anomalous non-laminar micro-bends in material pathlines close to the interface of the indenter. To this end, lattice rotation rate was characterized by coupling the DIC-characterized strain fields with a calibrated VPSC framework. Subsequent quantification of Taylor factor fields by coupling DIC and OIM revealed relatively hard/soft domains undergoing plastic deformation during indentation that led to the formation of microbends.

CHAPTER 5. SEQUENTIAL INDENTATION-TYPE PROCESSES

5.1 Introduction

Deformation occurring in sequential indentation loading is critical for understanding the governing mechanics associated with mechanical surface treatment methods as well as indentation-based materials testing methods. For the former, it has been well investigated that surface integrity of metallic materials can be enhanced by using appropriate mechanical surface modification techniques. More recently, significant interest has been found in the use of these approaches to achieve superior functional performance through fabrication of gradient microstructures due to surface severe plastic deformation (S^2PD) [48]. In these S^2PD methods, near surface layers are subject to high plastic strains that decay into the subsurface, this yielding a gradient of grain refinement dependent on the gradient in the strains imposed at the surface. These gradient materials have been shown to exhibit improved resistance to wear [58], fatigue [3,114] and corrosion [5,115], as well as a superior combination of ductility and strength [10,13]. S^2PD approaches based on surface mechanical attrition treatment (SMAT) [116–118] and ultrasonic impact treatment (UIT) [115] rely on repeated surface impact to impart graded strain levels at surfaces; these process configurations have gained significant attention due to their inherent high controllability and compatibility with complex part geometries [119]. While similar to conventional air blast shot peening (ABSP) in their general principle [120], discrepancies between these methods exist in terms of the size of the tool geometry (i.e., diameter), as

well as the relative spacing (i.e., overlap), depth and especially direction of loading with respect to the surface. Selection of these parameters requires consideration of optimal treatment schedules to achieve specific levels of maximum strain as well as subsurface coverage in terms of the overlap of individual strain fields from unit-scale deformations.

The unit deformation field under multiple indentation-type loading events has been studied in the context of phenomena associated with sequential indentation and simultaneous co-indentation. Understanding of deformation in sequential indentation loading is important for effective selection of materials testing parameters that involve indentation-based assessments of hardness and strength. In this regard, critical spacing of indents is dependent on the relative size of the elastic-plastic zone underneath a single indent, where this spacing is generally set large enough to prevent substantial overlap of the associated subsurface plastic zones. In this regard, Samuels and Mulhearn have shown that a nominal indentation spacing of $2.7d_p$, where d_p is the indentation depth using a pyramid indenter, is sufficient to ensure less than 5% isostrain overlap in successive indentations [121]. With this as a basis for determination of indentation spacing, a host of other similar studies that have established the size of the elastic-plastic zone can inform similar estimates of minimum indentation spacing based on indenter geometry and workpiece material. In addition to the sequential indentation problem, the effects of multiple indentation-type loading on subsurface deformation have been studied through simultaneous co-indentation configurations wherein a surface is deformed concurrently by a pair of indenters set at controlled relative spacing [122]. In this regard, the effect of indenter separation length between was investigated in terms of residual stress components and development of subsurface plastic zones. While these studies have guided development

of finite element (FE) models for process scale simulations [123–125], they inherently have relied on post mortem assessments for validation of the evolving plastic field and have not provided a framework validated using measurements of the evolving plastic zones present due to multiple indentations.

Fundamental understanding of the evolving deformation field in indentation loading is possible using in situ experimental assessments [86,105,106], this complemented by validated FE models [77,124]. These *in situ* methods have been used to characterize the subsurface deformation field in the indentation of surfaces under various tool geometries. These studies have revealed and/or verified key features of the deformation field, such as the formation of material stagnation zones (e.g., dead zones) under penetration due to rigid flat punches and circular indenters [76]. Further, these *in situ* approaches have been useful for calibration of dead zone and plastic zone formulations for expanding cavity models to predict the state of the deformed subsurface [84,106].

The objective of this chapter is to elucidate an understanding of the effects of controllable parameters in sequential indentation of a model strain hardening material on size of the overlapping plastic zones as well as characteristics of the overall strain field in terms of gradient and maximum strain levels imposed. For this purpose, oxygen-free high-conductivity (OFHC) Cu was used as a model material as it is a conventional representative of a wide range of moderate stacking fault energy face centered cubic material systems. *In situ* mappings of material flow at high spatial resolution were facilitated using a digital imaging platform to quantify the deformation field during two sequential circular indentions under plane-strain conditions. An FE model was validated and the effect of indentation depth and separation length on evolutions of strain components and indentation

load was investigated. From the present results, empirical frameworks for control of subsurface strains and strain field overlap are elucidated. Further, the relative energy efficiencies and strain path changes due to specific combinations of indentation spacing and depth parameters used during indentation-type processing are evaluated.

5.2 Experimental Platforms

5.2.1 Sequential Circular Indentation Setup

Figure 5-1(a) shows a schematic of the experimental configuration used in the present study. Experiments were carried out under plane-strain conditions ensured by planar constraint of the imaged work surface by a tempered glass plate and constraint of the opposing surface by a steel backer plate. In this configuration, a series of indents were carried out sequentially on a workpiece. Each indentation in the sequence was conducted at the same final depth of indentation (H), rate of indentation (v_0) and processing time (T_0). To provide relative positioning of each indent, the workpiece was shifted in the lateral direction to yield an effective centerline-to-centerline spacing length (S). In the present study, the indenter was loaded with H = 1.5 mm, v_0 = 0.1 mm/s, T_0 = 15 s and S = 2.5 mm. The projected contact length of the indenter with the workpiece (L) is given by $L = \sqrt{R^2 - (R - H)^2}$. The resulting surface profiles produced from the first and second indents are shown schematically in Figure 5-1(b). For this study, a circular indenter of radius R = 2.5 mm was constructed from tool steel by electrical discharge machining (EDM) and finished by polishing the indenter surface with 1000 grid SiC paper. OFHC Cu workpieces were machined into 25 mm × 60 mm × 6 mm blocks pre-annealed at 600 ºC for 2 hours.

Quantitative analysis of the deformation was conducted by DIC-based setup as described in Chapter 3.

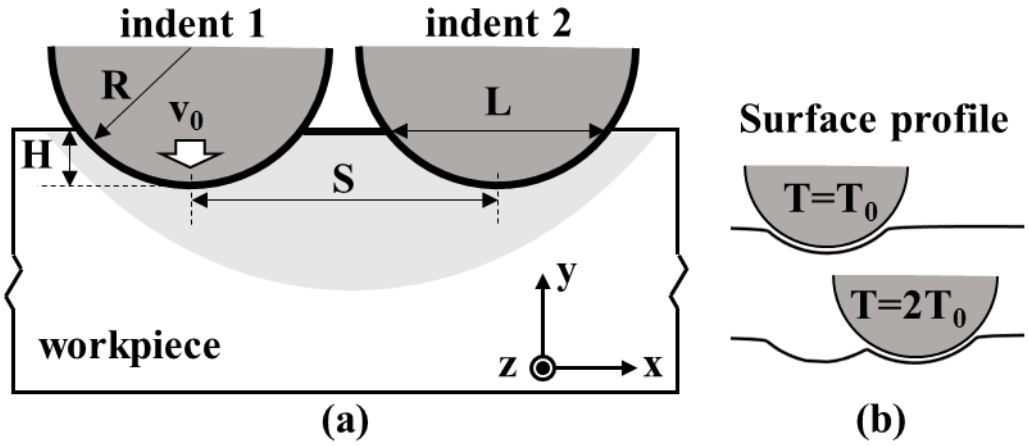

Figure 5-1 Schematic representation of (a) sequential indentation configuration and (b) surface profiles yielded from single and two indentations.

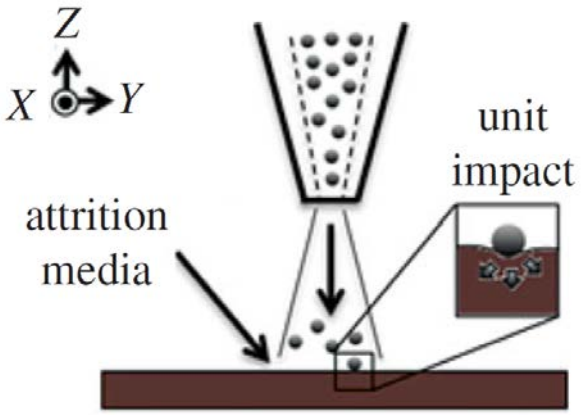

Figure 5-2 Configuration of direction SMAT.

5.2.2 Surface Mechanical Attrition Treatment Setup

To complement these unit deformation tests, S^2PD experiments were performed. Directional SMAT was performed on as-received OFHC Cu (alloy 101, 2.3mm thick)

using spherical silica SiO_2 shots (diameter $d_{shot} \sim 200$ μm) accelerated by a directed blast of air at 0.4 MPa. The area of the specimens was 25.4 mm × 25.4 mm. The blast of SiO_2 impacts was directed normally with respect to the surface near the center of the workpiece. Consequently, the area close to the center of the specimen was exposed to several hundred overlapping impacts oriented in near parallel orientations with respect to the Z-axis in Figure 5-2. The surface treatment was performed for durations of 600 s and 1200 s. The velocity of impact v_{impact} was measured to be approximately 10 m·s^{-1} by recording the mass flow rate.

5.3 Simulation Methods

5.3.1 2D FEA Model

Deformation in sequential indentation was simulated as a series of indents in ABAQUS/Explicit. The indenter was modeled as a discrete rigid body and the workpiece was modeled as an isothermal body using four-node and three-node bilinear, reduced integration, and plane-strain elements as shown in Figure 5-3. The isothermal state of the workpiece was justified considering the low loading rates used in the experimental studies. The Johnson–Cook material model was used with $\sigma = [A + (B\bar{\varepsilon}^{pl})^n]\left[1 + C \times log\left(\frac{\dot{\bar{\varepsilon}}^{pl}}{\dot{\varepsilon}_0}\right)\right]$ where [A, B, C, $\dot{\varepsilon}_0$, n] = [90 MPa, 292 MPa, 0.025, 1 s^{-1}, 0.31] for OFHC Cu [126]. The indenter was vertically translated into the specimen surface by displacement control with a constant loading rate of 0.1 mm/s, retracted and then displaced in the lateral direction with a certain spacing length and repeated for the second indent. The contact was defined as node-to-node contact of the master and slave surfaces with Coulomb friction coefficient of μ = 0.2. This friction coefficient was determined by simulation trials that showed

agreement with deformation fields of the experimental results. The accuracy of the simulation was assessed by comparing the predicted effective plastic strain and indentation load with the DIC-based measurements, as in the ensuing. After validating the simulation framework, a series of parametric simulations were conducted with H/R = [0.1, 0.2, 0.3, 0.4, 0.5], and S/R = [0.1, 0.2, 0.5, 1.0, 2.0, 3.0].

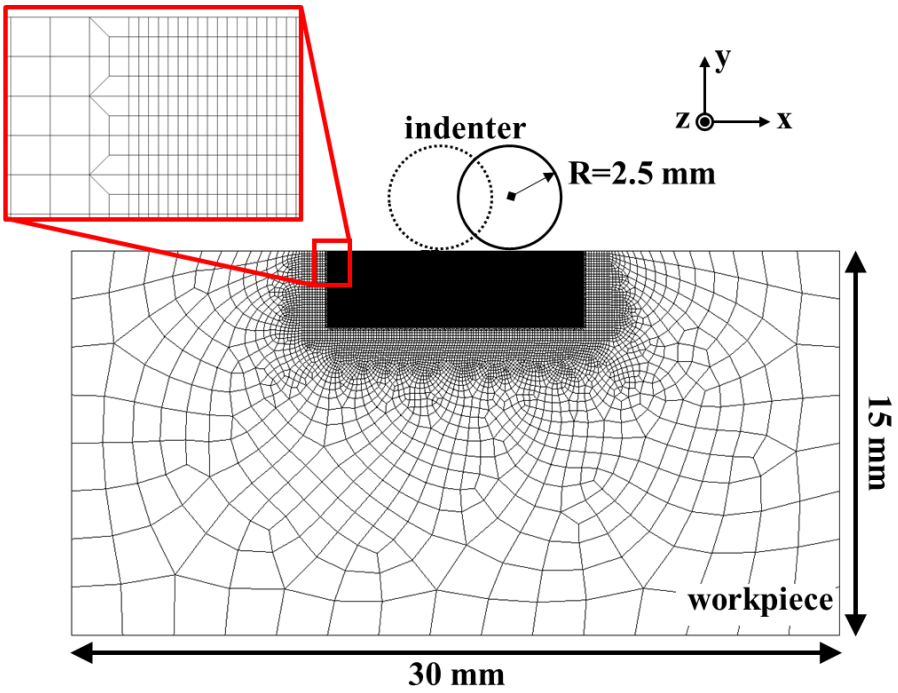

Figure 5-3 Meshing of finite element (FE) model of the workpiece and close view of refined mesh elements in the vicinity of contact region.

5.3.2 3D FEA Model

Deformation in SMAT was simulated as a sequence of impacts and was implemented through Python subroutines and built-in scripting interface in ABAQUS. Using these subroutines, the mechanical state of the workpiece prior to a single impact was extracted from the post-deformation state from the previous impact simulation. Impacting

shots were modelled as spherical elastic bodies with diameter D = 200 μm, E =73 GPa and ν = 0.17 using tetrahedral (C3D4) mesh elements. The workpiece was modelled as an isothermal body using hexahedral elements (C3D84, element size: 10 μm) with reduced integration and hourglass control. The iso-thermal state of the workpiece was governed by the diffuse nature of deformation imposed by spatially and temporally discrete impacts across the work surface that prohibit concentrated heat dissipation. Note that high pressure air blast also would act to subdue temperature rise by enhancing thermal dissipation. The Johnson–Cook material model was used for OFHC Cu. Gaussian-distributed velocities of $V_x = N(0, 0.5)$, $V_y = N(0, 0.5)$, $V_z = N(10, 0.01)$ m·s^{-1} were assigned to the impacting shots. Initial positions of shots were also Gaussian-distributed at $N(0, 10)$, $N(0, 10)$ μm with respect to the workpiece center.

5.4 Sequential Circular Indentation

5.4.1 Deformation Evolution

The deformation occurring in multiple indentations on the OFHC workpiece was measured using *in situ* DIC. Figure 5-4 shows optical images taken from a series of indents carried out up to a final depth of H/R = 0.3 and with a relative spacing of S/R = 1.0. The optical image frames in Figure 5-4(a) and Figure 5-4(d) show the state of workpiece at the final indentation depth for the first indent and second indent, respectively. The corresponding effective strain fields for these conditions are provided in Figure 5-4(b) and Figure 5-4(e). As is seen in the figures, the deformation occurring in the first indent is similar to that previously reported for circular indentation of OFHC Cu in Ref. [106].

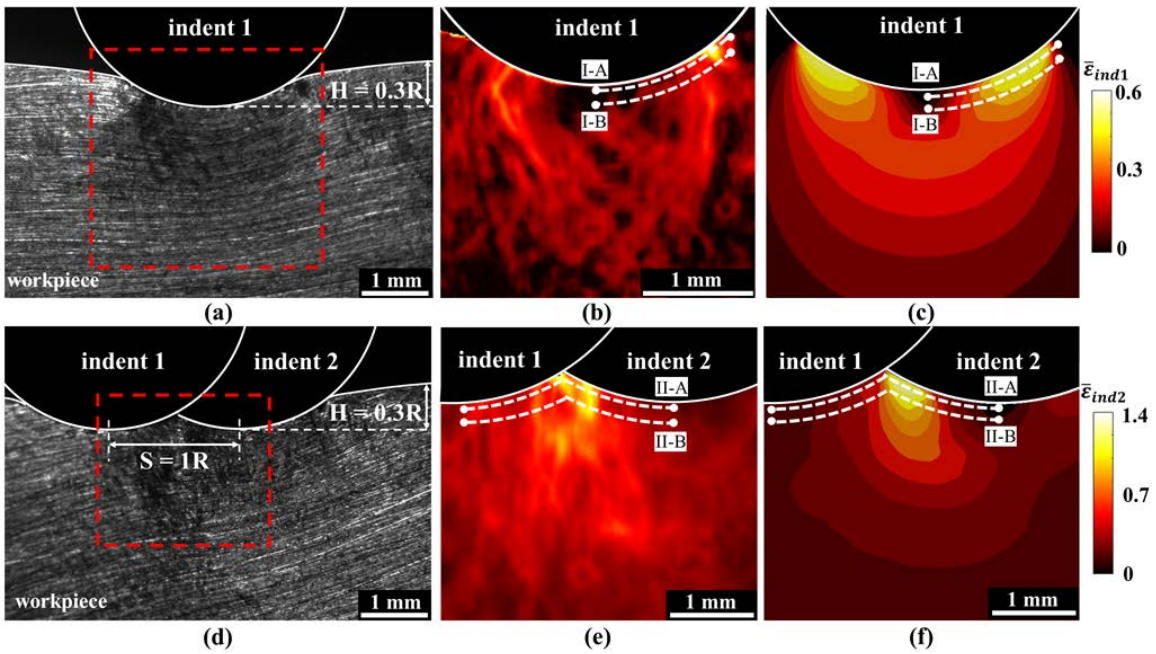

Figure 5-4 (a) Optical image of final deformed workpiece, (b) experimental and (c) FE-predicted distribution of $\bar{\varepsilon}$ after a single indent at H/R = 0.3. (d) Optical image of final deformed workpiece, (e) experimental and (f) FE-predicted distribution of $\bar{\varepsilon}$ after the second indent at S/R = 1.0.

In this regard, a hemispherical region of material displaces with the indenter as it penetrates into the workpiece. At the boundary of this dead zone, a semi-circular banded region persists where the maximum effective strain at normalized indentation depths of H/R = 0.19 and H/R = 0.33 was $\bar{\varepsilon} \sim$ 0.23 and $\bar{\varepsilon} \sim$ 0.34, respectively [106]. It was also noted that at larger indentation depths, these bands extended to greater subsurface depths and become increasingly diffuse. In the present work, the depth of the plastic zone at an indentation depth of H/R = 0.3 was ~ 1.10R and the lateral extent of this plastic zone was ~ 1.45R. At greater subsurface depths, the effective strain falls below an appreciable level

of $\bar{\varepsilon} < 0.01$, wherein elastic deformation is likely more dominant. The deformation occurring during the second indent is also shown in Figure 5-4(e). From the deformation fields, a maximum plastic strain in the deformed subsurface was $\bar{\varepsilon} \sim 0.6$ was obtained after the first indent and this was increased to $\bar{\varepsilon} \sim 1.3$ after the second indent.

From the effective strain fields, the plastic strain at each loading step was measured along pre-defined contours directly underneath the indenter (e.g., I-A, I-B, II-A, II-B) and offset from the surface by $0.05R$ and $0.3R$, respectively, as is shown in Figure 5-4(b) and Figure 5-4(e). The resulting distribution along these curves is summarized in Figure 5-5(a) and Figure 5-5(b). The subsurface strain distributions along these curves for the first indent are summarized in Figure 5-5(a). The effective strain along the contour I-A at $x/R = 0.0$ (e.g., centerline of the first indent) was $\bar{\varepsilon} \sim 0.08$, which is lower than the corresponding strain of $\bar{\varepsilon} \sim 0.23$ at a similar position in contour I-B. This is expected as contour I-A is in closer proximity to the dead zone. The plastic strain along contour I-A reaches a maximum value of $\bar{\varepsilon} \sim 0.48$ at $x/R = 0.5$ and rapidly decreases to $\bar{\varepsilon} \sim 0.05$ at $x/R = 0.7$. Similarly, the plastic strain along contour I-B reaches the maximum value of $\bar{\varepsilon} \sim 0.30$ at $x/R = 0.5$ and decreases to $\bar{\varepsilon} \sim 0.05$ at $x/R = 0.8$. These observations are consistent with both the presence of a region of low strain (i.e., dead zone) near the indent centerline and a narrow high strain band formed toward the periphery of the indenter contact and flanking the dead zone.

The cumulative strain distribution resulting from the second indent along contours II-A and II-B are shown in Figure 5-5(b). For the second indent, this shows that the maximum induced effective strain of $\bar{\varepsilon} \sim 1.32$ occurs at $x/R = 0.5$ for contour II-A, this

compared to $\bar{\varepsilon}$ ~ 0.73 for contour II-B. It should be noted that the strain in the dead zone region of the first indent was increased by the presence of the second indent. In this regard, the cumulative effective strain at x/R = 0.0 was $\bar{\varepsilon}$ ~ 0.21 and $\bar{\varepsilon}$ ~ 0.32 for contours II-A and II-B, respectively. Figure 5-4(c) and Figure 5-4(f) shows the FE-predicted distribution fields of effective plastic strain in the same regions reported above from the experimental measurements. The corresponding strain distributions are reported in Figure 5-5(a) and Figure 5-5(b) and good agreement is found between the experimental measurements and the FE-based predictions. The experimental and predicted results in Figure 5-5 matched closely with R^2 = 0.98, this providing validation of the simulation framework.

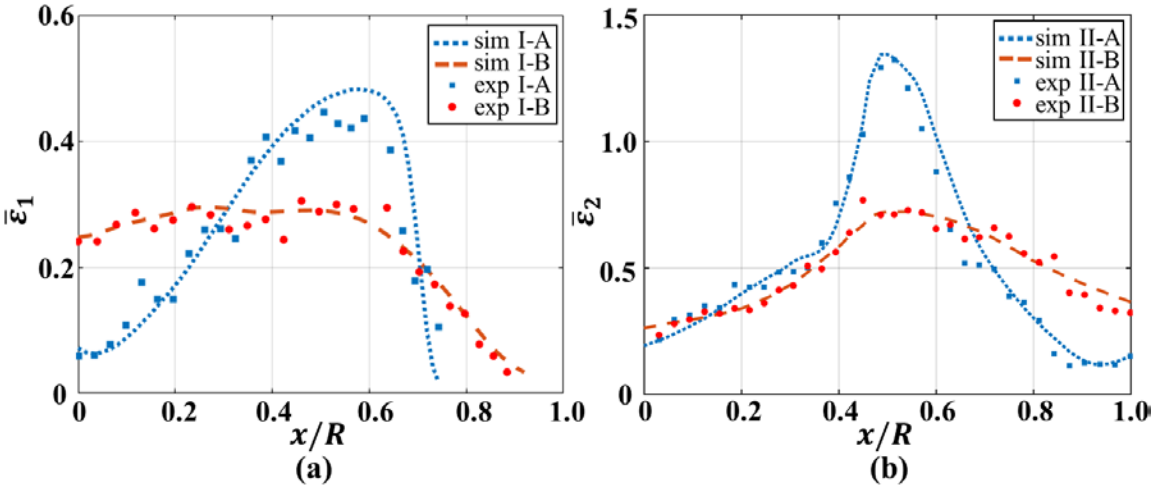

Figure 5-5 Comparison of effective plastic strain between DIC-obtained and FE-predicted results along contours I-A, I-B, II-A, and II-B after (a) single and (b) sequential indentation at H/R = 0.3 and S/R = 1.0.

Further validation of the simulation results was made by comparison of the indentation load to the experimental measurements. Figure 5-6 shows the comparison of

the indentation load with respect to normalized indentation depth H/R = [0.1, 0.2, 0.3, 0.4, 0.5] during the first indentation in the sequence. In the figure, the normalized indentation load from the FE model ranged from $F_1 = 280\times10^3$ N/m to $F_1 = 1130\times10^3$ N/m and was close to the experimentally measured values obtained within less than 15% relative error. These data were also in good agreement with the load evolution predicted by a calibrated expanding cavity model (CECM) established in a prior study [106]. Comparing both models, the FE simulation provided a better estimation of indentation load compared to the analytical solution. It is also worthwhile to note that the CECM is not valid at larger normalized indentation depth of $H/R > 0.3$ as assumptions regarding the growth of the internal expanding cavity are not valid in this regime.

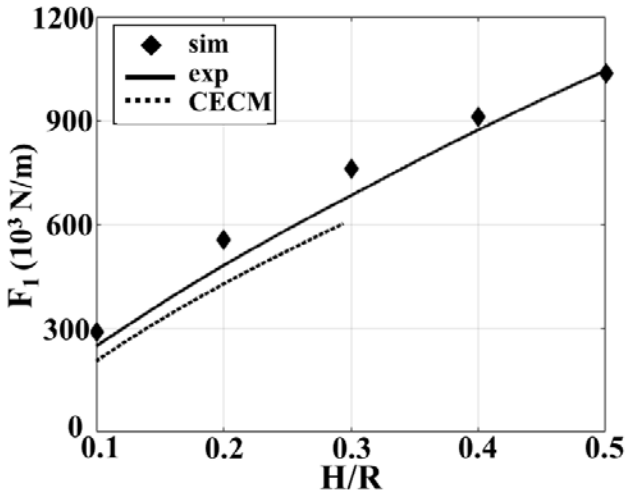

Figure 5-6 Indentation load with respect to normalized depth of indentation of H/R during the first indentation.

After validation, a series of simulations were carried out to explore the role of controllable parameters in sequential indentation on the subsurface plastic zone. For this

purpose, normalized indentation depths of H/R = [0.2, 0.3] and normalized indentation spacings of S/R = [0.1, 0.2, 0.5, 1.0, 2.0, 3.0]. Figure 5-7 shows the result of the simulation results with Figure 5-7(a)-(f) at H/R = 0.2 and Figure 5-7(g)-(l) at H/R = 0.3. From the figure, it is clear that the normalized indentation spacing determines the overall nature of the subsurface deformation zone. At small values with S/R < 0.2, as in Figure 5-7(a), Figure 5-7(b), Figure 5-7(g) and Figure 5-7(h), the effective strain distributions after the second indentation were markedly similar to deformation fields reported for a single indent [106]. In this regard, a noticeable dead zone region was produced underneath the indenter that featured low plastic strains with $\bar{\varepsilon}$ < 0.1. Additionally, a band of high strain rate and strain surrounded the dead zone and featured high effective strains with $\bar{\varepsilon}$ > 0.5.

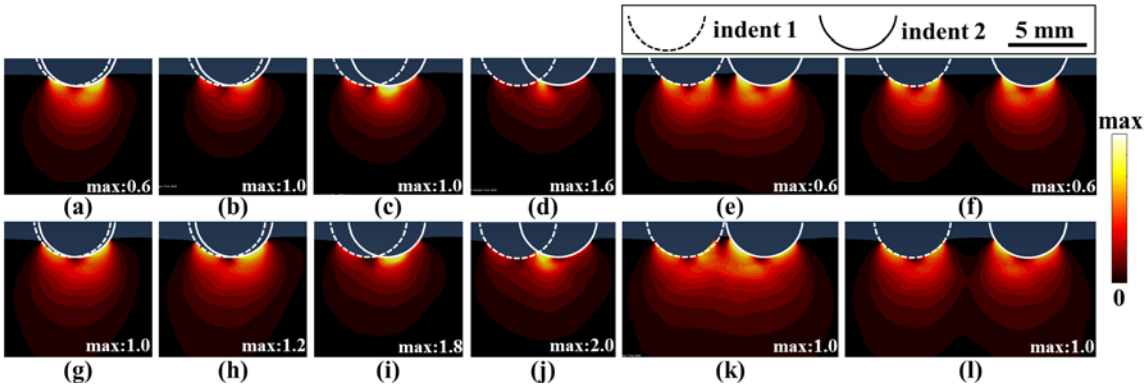

Figure 5-7 Effective plastic strain fields of subsurface regions from FE model with S/R = [0.1, 0.2, 0.5, 1.0, 2.0, 3.0] and (a)-(f) H/R = 0.2, (g)-(l) H/R = 0.3.

As the normalized indentation spacing was increased to $1.0 \geq S/R \geq 0.5$, as shown in Figure 5-7(c), Figure 5-7(d), Figure 5-7(i), and Figure 5-7(j), regions of the deformed subsurface were exposed to strains with $\bar{\varepsilon}$ > 1.0, primarily those located between the two

indents. In this case, the maximum effective plastic strain in the deformed subsurface was nearly double that resultant after a single indent. At normalized indentation spacing with $H/R \geq 2.0$, as in Figure 5-7(e), Figure 5-7(f), Figure 5-7(k), and Figure 5-7(l), the individual deformation fields associated with each indent were more clearly visible due to the increased separation. Further at the largest normalized indentation spacing of $H/R \geq 3.0$, the maximum plastic strain in the deformed subsurface was equivalent to that seen for the case of a single indent and/or a closely-spaced set of sequential indents as in Figure 5-7(a) and Figure 5-7(g).

5.4.2 Discussion

The present study investigated the effects of process parameters in sequential indentation on mechanical responses of a model strain hardening material in terms of the subsurface deformation field and indentation load. In the context of controllability of indentation-based methods for imparting controlled subsurface strain distributions, the present results have utility for understanding the relationship between surface and subsurface coverage, energy dissipation and role of strain path changes in heterogeneous surface deformation. Each of these implications are discussed in the ensuing.

From the present results, subsurface deformation in indentation-based S^2PD is controllable by appropriate selection of indentation depth and spacing parameters. Measures of interest to quantify severity and homogeneity of the deformation include the maximum strain in the deformed subsurface and the degree of deformation overlap (e.g., subsurface coverage) in the resulting strain fields, respectively. For the former, the normalized maximum effective plastic strain in the deformed subsurface for the first

indentation, $\bar{\varepsilon}_{1\_max}/\bar{\varepsilon}_{0.5R}$, was characterized with respect to normalized depth of indentation of H/R, where $\bar{\varepsilon}_{0.5R}$ refers to the maximum effective plastic strain with H/R = 0.5. In this regard, the normalized maximum strain increases from $\bar{\varepsilon}_{1\_max}/\bar{\varepsilon}_{0.5R}$ = 0.45 to $\bar{\varepsilon}_{1\_max}/\bar{\varepsilon}_{0.5R}$ = 1.0 from H/R = 0.1 to H/R = 0.5, as shown in Figure 5-8(a). The normalized maximum effective strain for the second indentation, $\bar{\varepsilon}_{2\_max}/\bar{\varepsilon}_{0.5R}$, depends strongly on the specific value of normalized indentation spacing S/R. Figure 5-8(b) shows the normalized maximum effective strain for each value of normalized indentation depth H/R across all values of normalized indentation spacing S/R. In this regard, $\bar{\varepsilon}_{2\_max}/\bar{\varepsilon}_{0.5R}$ for H/R = [0.1, 0.2, 0.3, 0.4, 0.5] corresponded to S/R = [0.5, 0.5, 1.0, 1.0, 1.0]. From the figure, the normalized maximum strain increases from $\bar{\varepsilon}_{2\_max}/\bar{\varepsilon}_{0.5R}$ = 1.0 to $\bar{\varepsilon}_{2\_max}/\bar{\varepsilon}_{0.5R}$ = 2.5 from H/R = 0.1 to H/R = 0.5. The peak strain at each stage followed a relationship in the form: $\bar{\varepsilon}_{max}/\bar{\varepsilon}_{0.5R} = C(H/R)^n$, where $(C, n) = (1.42, 0.53)$ for the first indent and $(C, n) = (3.84, 0.59)$ for the second indent. The R-squared value for these fits were both 0.99.

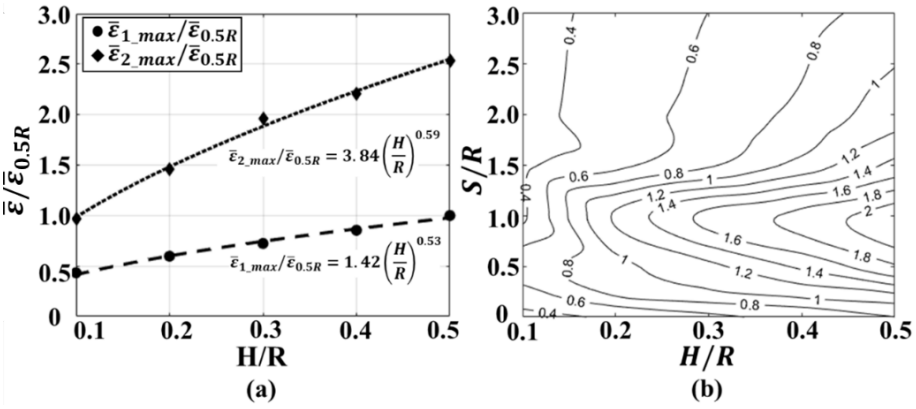

Figure 5-8 Normalized maximum effective plastic strain with respect to (a) H/R for single and sequential indentation and (b) H/R and S/R for sequential indentation.

To determine the role of normalized deformation parameters H/R and S/R in affecting subsurface deformation coverage, the subsurface effective strain fields were characterized for degree of strain field overlap. Figure 5-9 shows the size of the deformation-affected region across a range of indents from S/R = [0.1, 0.2, 0.5, 1.0, 1.5, 2.0] at H/R = 0.3. In this figure, individual nodes were categorized into two classes dependent on whether the respective total cumulative strain of each node was primarily determined by the first indentation ($\bar{\varepsilon}_1 \geq 0.1, \Delta\bar{\varepsilon} < 0.1$) or by both indentations ($\bar{\varepsilon}_1 \geq 0.1, \Delta\bar{\varepsilon} \geq 0.1$), where $\bar{\varepsilon}_1$ is the effective strain due to the first indent and $\Delta\bar{\varepsilon}$ is the incremental effective strain associated with the second indent. In the below discussion, the latter of these two regions is referred to as the subsurface overlap region. The threshold of $\bar{\varepsilon} \geq 0.1$ is based on the minimum deformation level that has been observed to alter the microstructure in the subsurface of a S^2PD-processed copper materials [127]. From the figure, it is evident that the size of the subsurface overlap region is dependent on the indentation spacing length. At a normalized depth of indentation of H/R = 0.3, the area of overlap region ranged from 0.25×10^{-6} m^2 at S/R = 0.1 to the maximum value of 2.06×10^{-6} m^2 at S/R = 1.0, and then gradually decreased to zero at S/R = 3.0.

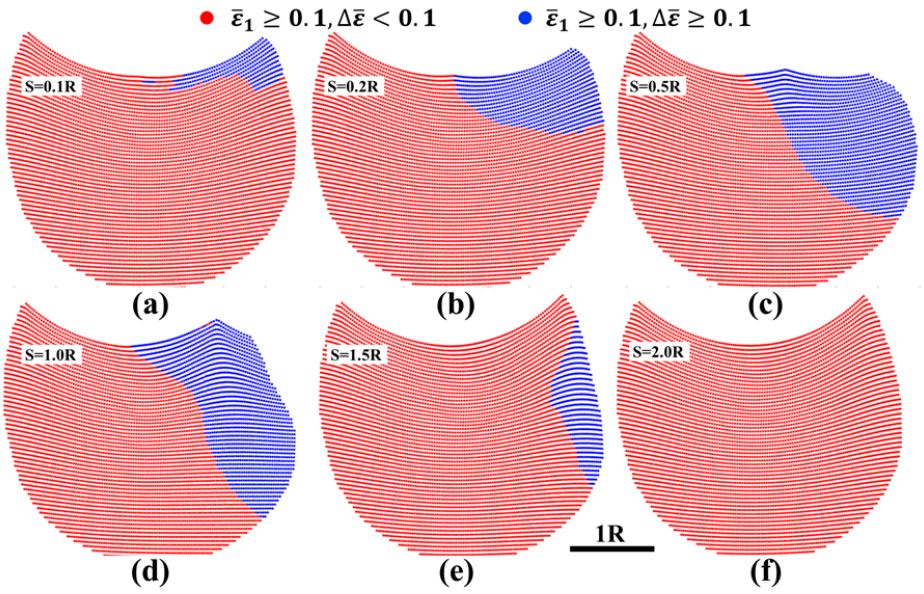

Figure 5-9 Deformation-affected region produced by sequential indentation configuration at normalized indentation depth of H/R = 0.3. Red nodes indicate the regions only deformed by the first indent and blue nodes indicate the regions affected by both indentations.

To understand the effect of normalized indentation depth H/R on the size of the plastic zone, Figure 5-10(a) summarizes the size of the subsurface area wherein a threshold strain of $\bar{\varepsilon}_1 \geq 0.1$ was achieved. In this regard, as normalized indentation depth increases from H/R = 0.1 to H/R = 0.5, the normalized area of the plastic zone increased from $A_1/A_{0.5R}$ = 0.1 to $A_1/A_{0.5R}$ = 1.0, where $A_{0.5R}$ refers to the area of region plastically deformed such that $\bar{\varepsilon}_1 \geq 0.1$ with H/R = 0.5. The size of the overlap region was also quantified as a function of normalized indentation depth H/R where material in the overlap region $A_2/A_{0.5R}$ satisfy $\bar{\varepsilon}_1 \geq 0.1$ and $\Delta\bar{\varepsilon} < 0.1$. As was the case for maximum effective strain, the size of the overlap region depends strongly on the specific value of normalized

indentation spacing S/R. Figure 5-9(b) shows he normalized maximum size of the overlap region $A_{2\_max}/A_{0.5R}$ for each value of normalized indentation depth H/R across all values of normalized indentation spacing S/R. In this regard, It should be noted that $A_{2\_max}/A_{0.5R}$ was approximately $0.3A_1/A_{0.5R}$ for all values of H/R. From the figure, these normalized areas followed a relationship in the form: $A/A_{0.5R} = C(H/R)^n$, where $(C, n) = (2.78, 1.49)$ for $A_1/A_{0.5R}$ and $(C, n) = (0.78, 1.51)$ for $A_{2\_max}/A_{0.5R}$. The R-squared value for these fits were both 0.99.

A commonly used metric for mechanical surface treatment methods has come in the form of surface coverage, which has been used to quantify the relative size of the deformed surface area [128,129], as opposed that of the subsurface as in the present work. Prior work has established the importance of control of surface coverage to control overall functional properties by mitigation of possible defects, such as surface cracks or folds at regions undergoing significant deformation [130]. Figure 5-10 shows a schematic summarizing the surface coverage parameter for a single indentation as a function of the indentation spacing S and the projected contact length L, this given by $L = 2\sqrt{R^2 - (R - H)^2}$ as in Figure 5-1. From the figure, several modes of surface coverage are identified. First, when $S < \sqrt{2}L$ as shown in Figure 5-11(a), the indentation overlaps with pre-strained regions and the target surface is fully covered by surface indentations, this yield surface coverage exceeding 100%. When $\sqrt{2}L \leq S \leq 2L$ as shown in Figure 5-11(b), surface coverage drops below 100% as well as the overlap with the pre-strained regions. Finally, when $S > 2L$ in Figure 5-11(c), no overlap occurs between successive indents. It is worthwhile to note that the actual deformed surface profile from a single

indentation may result in material piling-up or sinking-in at the surface of the indent [89]. In this regard, sinking-in phenomena decreases the actual contact length of L compared to the derived value.

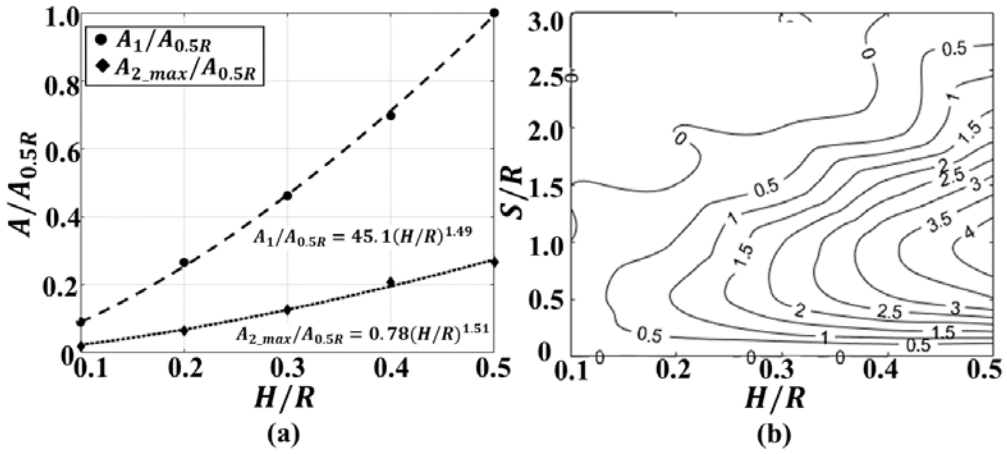

Figure 5-10 Normalized size of the deformation-affected area with respect to (a) H/R for single and sequential indentation and (b) H/R and S/R for sequential indentation.

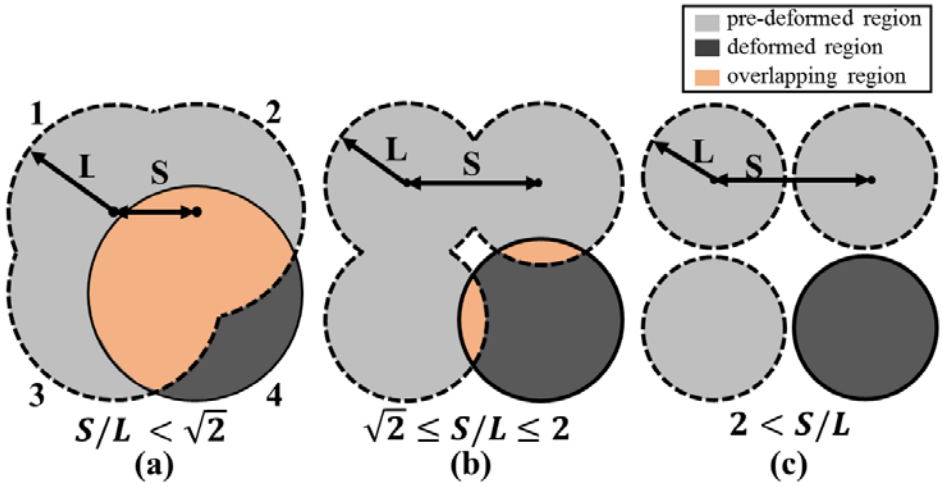

Figure 5-11 Schematic of surface coverage dependent on L and S in sequential indentation configuration where (a) $S < \sqrt{2}L$, (b) $\sqrt{2}L \leq S \leq 2L$ and (c) $S > 2L$.

The relationship of surface coverage to measures for quantifying severity and homogeneity of the subsurface deformation can be considered by evaluating the role of the normalized indentation spacing parameter S/L on the maximum strain in the deformed subsurface and the subsurface overlap/coverage. Figure 5-12(a) shows the ratio of maximum plastic strain $\bar{\varepsilon}_{2\_max}/\bar{\varepsilon}_{1\_max}$ with respect to S/L. From the figure, at S/L = 0, $\bar{\varepsilon}_{2\_max}/\bar{\varepsilon}_{1\_max}$ = 1.0. This increases to a maximum value of $\bar{\varepsilon}_{2\_max}/\bar{\varepsilon}_{1\_max}$ = 2.5 at S/L = 1.2 and decreases to $\bar{\varepsilon}_{2\_max}/\bar{\varepsilon}_{1\_max}$ = 1.0 at S/L > 4. In Figure 5-12(b), a similar trend can be observed for subsurface coverage which reaches a peak value of A_2/A_1 = 0.28 at S/L = 1.1. The effect of the indentation spacing parameter S/L on the load dissipated in the sequential indentation process is shown in Figure 5-12(c), where F_1 is the load from the first indent and F_2 the load from the second indent. From the figure, a maximum value of F_2/F_1 = 1.15 occurred at S/L = 2.0 and the ratio approached F_2/F_1 = 1.0 at larger quantities of S/L. It should be noted that decay to F_2/F_1 = 1.0 at large indentation spacing is expected as successive indents can be treated as independent deformation events in the presence of sufficiently large relative spacing. From the above analysis, subsurface coverage and subsurface maximum strain parameters are maximized with S/L in the range of [1.1, 1.2] and the required indentation load in this range is approximately equivalent to that of a single indent (e.g., $F_2 = F_1$).

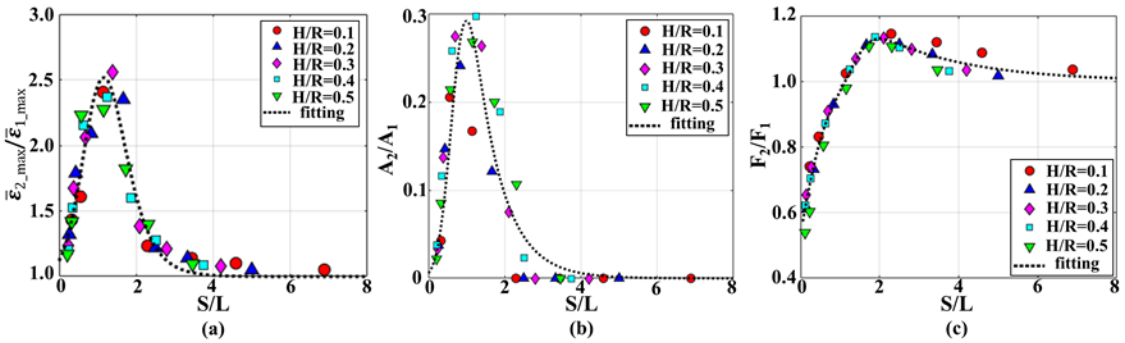

Figure 5-12 Ratio of (a) normalized maximum plastic strain, (b) normalized deformation-affected area, and (c) normalized indentation load in sequential indentation with respect to S/L for all investigated conditions.

The relative efficiency of a surface deformation process can be considered by analysis of maximum strain, surface/subsurface coverage and dissipated load. To quantify the total energy consumed in deforming the subsurface thorough sequential indentation, the total energy dissipated W_t was evaluated for each processing condition and was quantified based on the FE-predicted load trajectory, using $W_t = \sum_{i=1}^{2} \int F_i dH_i$ [131], where F_i, H_i, and i indicate indentation load, depth, and sequence number, respectively. The normalized total energy, $W_t/W_{t\_0.5R}$, dissipated is summarized in Figure 5-13 in terms of the normalized maximum plastic strain and the normalized subsurface overlap area. As expected, Figure 5-13(a) shows that larger plastic strains in the deformed subsurface result in a larger energy dissipation for a given depth of indentation. Figure 5-13(a) also shows that it is possible to achieve a given level of maximum plastic strain at lower dissipated energy depending on the sequential indentation parameters. For example, it is possible to achieve a normalized maximum plastic strain of $\bar{\varepsilon}_{2\_max}/\bar{\varepsilon}_{0.5R}$ ~ 1.0 at conditions of [H/R,

S/R] = [0.1, 0.5] and [H/R, S/R] = [0.5, 0.1], where the relative normalized total energy used in the latter condition is 80% lower. The upper and lower bounds for the total energy dissipated at a given level of strain are marked at the extents of the plot and fit according to an exponential function in the form: $W_t/W_{t\_0.5R} = C(\bar{\varepsilon}_{2\_max}/\bar{\varepsilon}_{0.5R})^n$, where the upper bound is defined by $(C, n) = (1.01, 2.31)$ and the lower bound defined by $(C, n) = (0.20, 2.30)$. Similarly, upper and lower bounds for the subsurface overlap are shown in Fig. 12(b) and are given by: $W_t/W_{t\_0.5R} = C(A_2/A_{0.5R})^n$, where the upper bound is defined by $(C, n) = (39.81, 1.02)$ and the lower bound defined by $(C, n) = (7.81, 1.08)$.

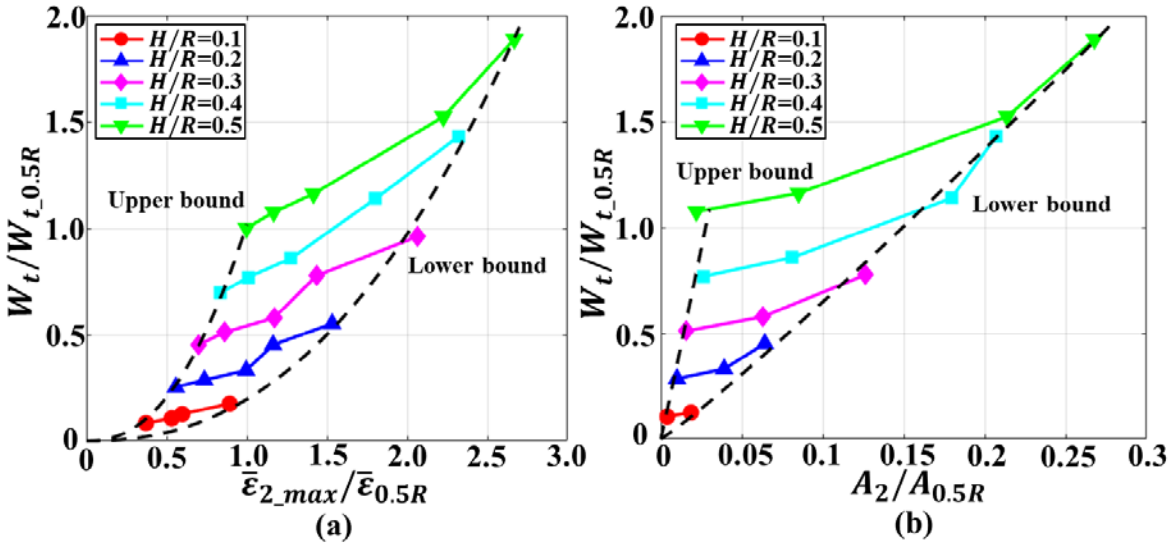

Figure 5-13 Total energy with respect to (a) maximum effective plastic strain and (b) maximum deformation-affected area in sequential indentation, where dashed lines indicate the upper and lower bound of total energy.

The present results also have utility for understanding the role of sequential indentation parameters on strain path changes in the deformed subsurface. In this regard,

it has been shown that the rate of microstructure refinement in S^2PD is sensitive to strain path changes occurring in the subsurface [28]. The influence of strain path changes in accelerating rates of microstructure evolution with respect to strains imposed has been well recognized in other severe plastic deformation (SPD) processes. For instance, the rate of grain refinement in pure Al alloys was seen to be accelerated in the B-route of equal channel angular pressing (ECAP), this compared to the other routes in ECAP undergoing the same deformation due to presence of strain path changes [28]. Similar effects have been seen in periodic shear-based transient surface generation, where strain path changes coupled with larger pre-strains resulted in greater reductions in grain size [48]. Figure 5-14(a) shows the evolution of maximum effective plastic strain with a normalized indentation spacing of S/R = 1.0 and normalized indentation depths of H/R = [0.2, 0.3]. Plastic strains induced at the first indentation were $\bar{\varepsilon}_1$= [0.47, 0.61] with H/R = [0.2, 0.3]. The evolution of each strain component is depicted in Figure 5-14(b), where ε_{22} is omitted since $\varepsilon_{22} = -\varepsilon_{11}$ in plane strain. Experimental measures of strain path changes during the two indentations were $[\Delta\varepsilon_{11}, \Delta\varepsilon_{12}]$ = [-0.16, 0.3] with H/R = 0.2 and $[\Delta\varepsilon_{11}, \Delta\varepsilon_{12}]$ = [-0.31, 0.88] with H/R = 0.3. Knowledge of these strain path change magnitudes is important since it has been shown in prior work that control of these components in surface deformation is critical in controlling texture formation and also in controlling rate of microstructure refinement at the surface [127,132].

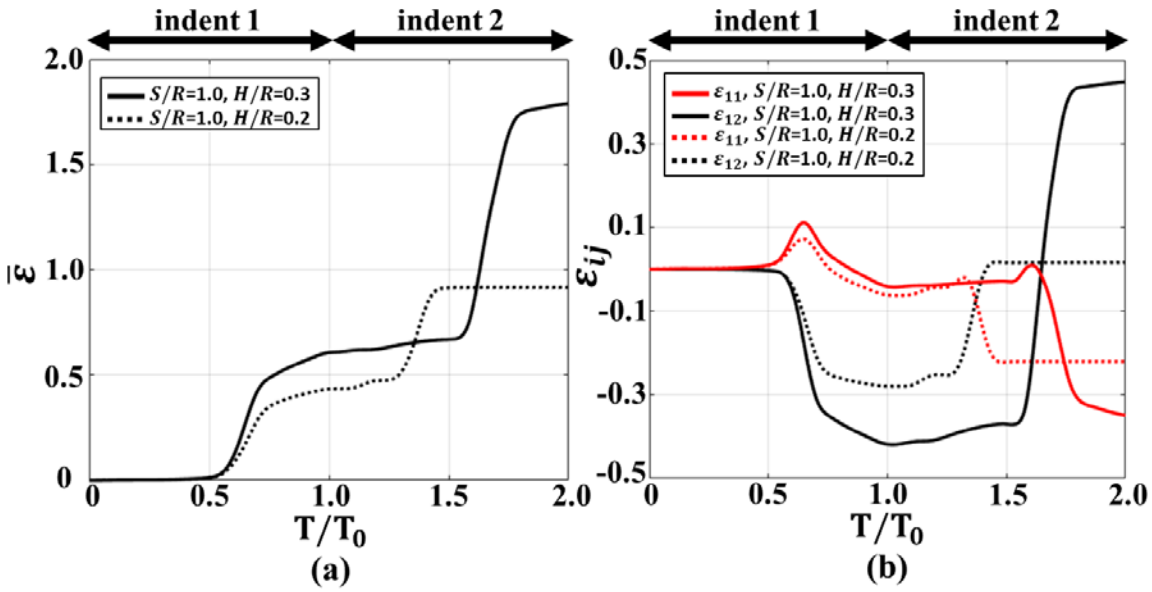

Figure 5-14 Evolution of (a) effective plastic strain and (b) Lagrangian strain components with respect to normalized processing time of T/T_0 in sequential indentation.

5.5 Surface Mechanical Attrition Treatment

5.5.1 Deformation Evolution

The simulated deformation field for a unit surface deformation is given in Figure 5-15(a) for $V = -0.5e_X + 0.6e_Y - 10e_Z$ m·s^{-1}, where e_X, e_Y and e_Z are unit vectors. The effective strain field and Lagrangian strain components in Figure 5-15(b–h) reveal a three-dimensional material flow pattern involving comparable strain components featuring max $|E_n|$ of similar orders of magnitude, where $|E_n|$ refers to components in the Lagrangian strain tensor *E*. The three-dimensional nature of the deformation field is important for understanding potential strain path changes, reversals and strain heterogeneity in the final deformed surface that can lead to accelerated microstructure refinement during S^{2}PD

[54,55]. In terms of strain rate, a maximum effective strain rate $\dot{\varepsilon} \sim 5.3 \times 10^5$ s^{-1} was observed during the surface deformation process.

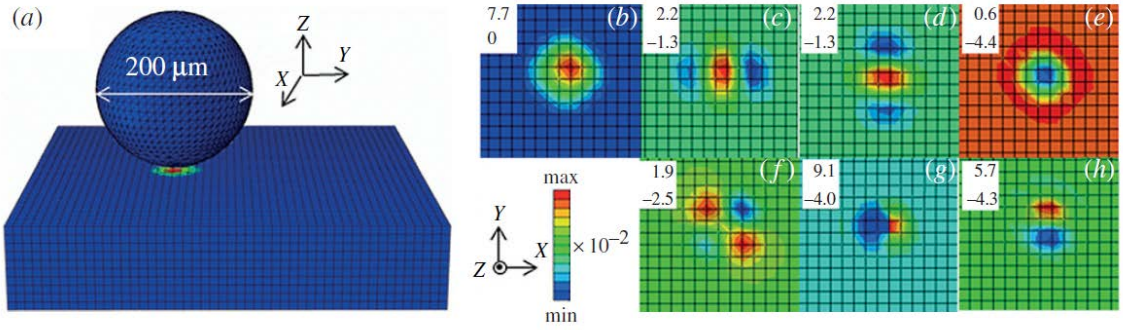

Figure 5-15 (*a*) Simulation of surface deformation for unit impact, (*b*) effective strain field and (*c–h*) Lagrangian strain tensor field components (E_{11}, E_{22}, E_{33}, E_{12}, E_{13}, E_{23}, respectively). Maximum and minimum values of the strain fields are provided in the inset data.

The deformation occurring after multiple surface impacts was simulated up to a total of 850 impacts. The final effective strain field exhibited a Gaussian-type spatial distribution as evident in Figure 5-16, this arising due to the Gaussian-distributed spatial locations of the spherical shots. Figure 5-16(a) also shows the numerically simulated strain profiles under the surfaces treated using SMAT. From the plot, it is clearly evident that the maximum strain in the deformed surface increases with the number of impacts and decays exponentially with increased depth into the work subsurface. In terms of maximum strain, at 850 impacts a peak effective strain in the deformed subsurface of $\varepsilon \sim 1.3$ at d =10 µm was seen. The exponential variation of strain can be modelled as $\varepsilon_d = \varepsilon_s exp(-\kappa d)$, where ε_s is the effective strain imposed on the surface and κ is an empirically obtained constant.

After 850 impacts, the effective strain in the subsurface followed $\varepsilon_d = 3.29\exp(-0.12d)$ with an R^2 =0.98. Both ε_s and κ were seen to increase monotonically with the number of surface impacts.

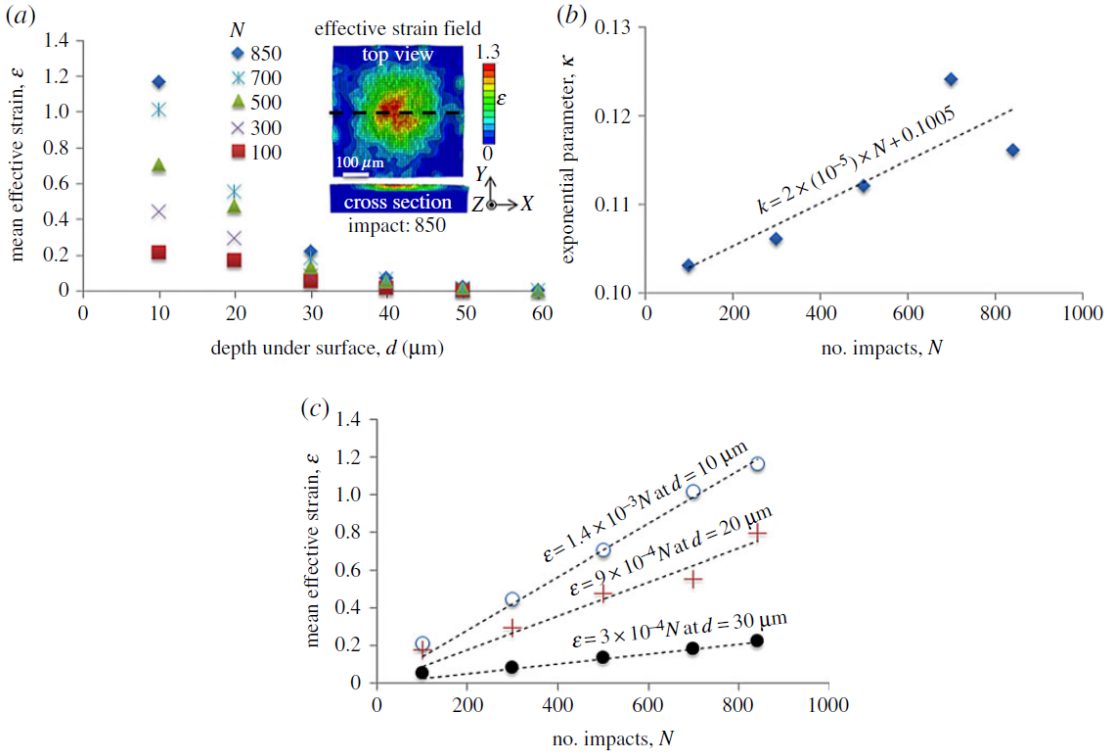

Figure 5-16 (*a*) Numerically obtained strain profiles under the surface deformed by SMAT. Inset shows strain field after 850 impacts on the surface and in cross section. (*b*) Variation in exponential parameter with respect to number of impacts N. (*c*) Variation in strain with respect to number of impacts at specified depths from treated surface.

From Figure 5-16(b)-(c), these variations were seen to be $\kappa = 2 \times 10^{-5}N + 0.1005$ and ε_s =1.4 × 10^{-3} N at d =10 μm, respectively, where N is the number of impacts. This variation manifests in the deformation affected zone increasing in dimensions with respect to the number of impacts. Further, the linear increase of ε_d with the number of

impacts implies that imposition of larger effective strains in the subsurface is possible with directly increasing surface treatment times. Interestingly, exponential variations in effective strains with respect to depths under the surfaces have also been seen in other controlled S^2PD platforms such as machining wherein parameters of the same were found to be relatable to process variables [133,134]. In this regard, it is evident that mechanical attrition processes avail similar control on process mechanics and microstructure response trajectories, the process variables of relevance being treatment times and energy of impact as discussed in the ensuing sections.

5.5.2 Microstructure Observation

The deformed microstructures in the SMAT-processed surfaces are depicted in Figure 5-17(a). From the OIM measurements, equiaxed-UFG microstructures are clear in the vicinity of the treated surfaces. The evolution of these microstructures is likely to be a consequence of CDRX in the deformed surface. In CDRX, progressive formation and subdivision of dislocation structures takes place due to increased levels of deformation, this resulting in grain fragmentation and formation of UFG states [44,135]. The relationship between grain size and treatment time is summarized in the δ_{15° versus d profiles provided in Figure 5-17(b). For the 600 s treatment, a grain size of $\delta_{15^\circ} \sim 0.5$ µm was observed over a relatively small subsurface depth of less than 3 µm. At the longer treatment duration of 1200 s, a similar grain size existed over a deeper zone approximately 15 µm in the deformed subsurface. The longer duration treatment also featured a smaller gradient in microstructure, with empirically obtained $\frac{\partial \delta_{15^\circ}}{\partial d}$ = 0.068 and 0.092 for the 1200 s and 600 s treatments, respectively. OIM scans performed on 1200 s specimens exhibited

a lower degree of alignment in their dislocation structures compared with those seen in OIM of 600 s specimens. These structures existed in zones between the severely deformed layer close to the surface and the pristine material existing at larger depths and are demarcated using thin black lines in Figure 5-17(a), referring to boundaries featuring disorientation $\theta > 2°$.

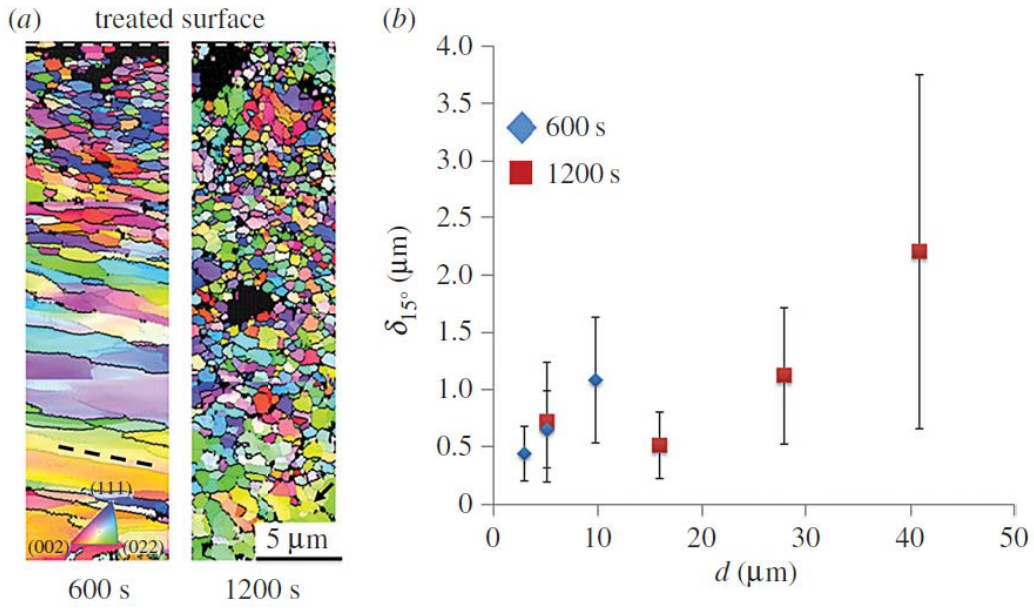

Figure 5-17 (a) Orientation imaging microscopy using electron back scattered diffraction of treated surface, (b) variation in grain size $\delta_{15°}$ with respect to depth d from treated surface. Dashed line in (a) shows orientation of dislocation structures. Arrow in (a) points at zone featuring poorly aligned dislocation structures.

Such dislocation structures are known to originate from strain path changes and accelerate microstructure evolution with respect to imposed effective strains [54,55]. Dominance of such dislocation structures exhibited by specimens that underwent S^2PD for longer durations suggests an increasing and cumulative contribution of strain path changes

to the mechanics of material evolution. In this regard, it can be anticipated that the thickness of the zone featuring ultra-fine grain sizes should expand nonlinearly with respect to treatment times due to the accelerated microstructure response as seen empirically: d = 3 μm, 15 μm at t = 600 s, 1200 s, respectively. However, this trend can be expected to disappear at longer treatment durations owing to strain hardening of the material directly beneath the surface, wherein a constant thickness of the zone featuring deformed grains can be anticipated despite an increasing number of impacts. Further investigations are needed to verify this claim.

5.6 Conclusion

In this chapter, the deformation field and load response during sequential indentation of a model strain hardening materials was investigated. *In situ* observations of the evolving subsurface deformation field were made using DIC-based measurement and these results were found to agree well with both analytical model and FE-based predictions of the strain distribution and load response. Maximum strain and the degree of strain field overlap in the deformed subsurface were maximized when the ratio of indentation spacing to projected indentation contact length was approximately S/L = [1.1, 1.2]. Additionally, relative differences in energy expended were found for differing conditions that produce similar levels of subsurface plastic strain and strain field overlap. In this regard, a lower bound for the maximization of both parameters can be determined across a range of conditions that include indentation depth and indentation spacing. The role of these parameters on affecting the magnitude of strain path changes occurring in the deformed subsurface were also evaluated in the context of understanding potential effects on microstructure and texture evolution in mechanical surface treatment methods. In addition,

deformation in directional surface mechanical attrition in terms of thermomechanical variables (i.e. strain, strain rate) and their decay into the subsurface was investigated using an FE model. It was observed that surface strain levels as well as the extent of the subsurface strained layer are directly related to the number of impacts on the workpiece surface.

CHAPTER 6. SLIDING-TYPE PROCESSES

6.1 Introduction

The endowment of gradients to near-surface microstructures in machine elements has garnered significant interest recently. This interest originates from strong correlations between these gradients and concomitant enhancements of surface originating structural and functional behavior in fabricated components [40,136]. For instance, gradients involving near-surface nanocrystalline microstructures on a microcrystalline bulk exhibit enhanced resistance to scratching, fatigue and corrosion [4,5,133] in addition to featuring superior combinations of ductility and strength compared to homogeneous microstructures featuring a lack of gradients [10]. The sources of these unique properties are found in the synergetic strengthening created by the incompatible deformation present across the mixture of refined and coarse grains, this resulting from promoted dislocation activities [13]. In this regard, materials with gradients in microstructures are more promising candidates for applications where the typical enhanced properties accessible through grain refinement must be attained without an appreciable loss of ductility.

Mechanical surface modification techniques involving grain refinement by severe plastic deformation (SPD), *viz.* surface severe plastic deformation (S^2PD), have been developed for fabrication of gradient microstructures [8]. Here, grain refinement involves interplay of dislocations through generation, storage and annihilation, sometimes further compounded by twinning. Through this interplay, a microcrystalline structure featuring $\delta > 10\ \mu m$ evolves to a nanocrystalline state featuring $\delta < 0.1\ \mu m$, where δ is the average grain size. Sliding-type processes utilizing the effect of high interfacial friction have been

found to be effective in nanocrystallization, while preserving the pristine state of the bulk. Examples of such processes include platen friction sliding (PFS) [136], surface mechanical grinding treatment (SMGT) [23], and sliding friction treatment (SFT) [24]. These processes enable the generation of deep work-hardened layers while providing control over the nature of the aforementioned gradients, wherein the functional behavior of the fabricated component can be optimized.

The transition from micro to nanocrystalline states can be characterized as a function of thermomechanical conditions prevailing during shear, this comprising strain, strain-rate and temperature (i.e., ε, $\dot{\varepsilon}$, T). Herein, the response of materials in extreme S^2PD conditions characterized by high strains (i.e., $\varepsilon > 8$) is less understood. Sources of this knowledge gap include the effects of high concentrations of grain boundaries with pre-existing and pristine dislocations during accumulative straining [47]. Further, these effects are compounded by process specific deformation fields, wherein frameworks that encapsulate material response as a function of the simplistic thermomechanical variables (i.e., ε, $\dot{\varepsilon}$, T) are challenging to formulate over an extensive thermomechanical domain [48]. The present work seeks to address this knowledge gap by delineating material behavior during deformation occurring in S^2PD by severe plastic burnishing (SPB). This process involves a hard wedge advancing over a workpiece, wherein the microstructural state in the latter is perturbed by the frictional sliding induced severe shear from the former. The mechanics of this process are analogous to machining [16]. However, the SPB process geometry involving extremely negative rake angles results in imposition of high surface strains (i.e., $\varepsilon > 8$), significantly higher than the strain resultant in conventional machining processes (i.e., $\varepsilon \sim 2$). Further, this deformation geometry enables the characterization of

material flow using a non-contact technique, digital image correlation (DIC). It is anticipated that deploying a combination of extreme rake angles and DIC will reveal the deformation behavior of materials in extreme strains. Towards this, prior experimentation has looked at the effect of extreme rake angles on material behavior by SPB [111,137]. These studies were instrumental in identification of unforeseen fluid-like flow behavior in metallic systems at extreme strains. However, questions remain regarding underpinnings of these flow characteristics with concomitant evolution of microstructures at severe strains.

Seeking to understand the aforementioned underpinnings of S^2PD, the objective of this chapter is to delineate the evolution of crystallographic textures in the processed subsurface in SPB of oxygen free high conductivity copper (OFHC Cu). Crystallographic textures refer to the distribution of orientations in a polycrystalline microstructure and are characterized using the orientation distribution function (ODF). In turn, the integral of the ODF or $f(g)dg$ represents the fractional volume in the polycrystal that features grains in close vicinity of the orientation g in the Euler space. While the evolution of crystallographic textures has received considerable attention in conventional SPD processes, such as equal channel angular processing (ECAP) [18] and large strain extrusion machining (LSEM) [57,140], its dependence on the imposed heterogeneous thermomechanics during S^2PD is not well understood, along with the mechanics of interaction of microstructural features such as grain boundaries and dislocations. This knowledge gap precludes generation of controlled gradients in crystallographic textures during S^2PD and is further complicated by process specific deformation fields. Herein, a phenomenological framework is proposed to predict the mechanics of texture and

microstructure evolution in SPB.

6.2 Experimental Platforms

6.2.1 Wedge-Based Burnishing Setup

To understand the evolution of the surficial deformation field and microstructural state, orthogonal SPB was performed on oxygen free high conductivity (OFHC) Cu under plane strain conditions. These conditions were insured by deploying a specimen thickness > 10 times the depth of engagement, as illustrated in Figure 3-1(b). The experimental configuration includes a tool steel wedge-shaped burnishing tool and an OFHC Cu workpiece. Both rake and flank faces of the burnishing tool were ground to produce an edge radius less than 10 μm. OFHC Cu workpieces with dimensions of 5 mm × 50 mm × 20 mm were annealed at 600 ºC for 2 hours to yield an average grain size of 20 μm and grain aspect ratio of ~ 0.3. Controllable processing parameters included wedge engagement depth (h), burnishing rate (v), and incident wedge angle (α). In this work, experiments with α = [-20°, -40°, -60°] were implemented, wherein h was set within the range of 100 - 150 μm and v was set at 0.1 mm/s. Subsequent discussion of the process mechanics is with respect to the coordinate system defined by the burnishing direction (BD), the normal direction (ND) and the transverse direction (TD) as shown in Figure 3-1(b).

6.2.2 Shear-Based Transient Surface Generation

A two-dimensional plane strain configuration shown in Figure 6-1 was used to generate deformed surfaces in annealed OFHC Cu (grain size δ ~ 50 μm). Control of the surface waveform was facilitated by advancing a hardened steel tool into the workpiece at

a constant lateral velocity (X-direction) of v_x = 25 mm·s^{-1} while sinusoidally modulating the tool vertical velocity (Y-direction) as $v_y(x) = 0.314 v_x cos\left(\frac{2\pi x}{0.15}\right)$ mm·s^{-1}, in the range v_y = [-7.9, 7.9] mm·s^{-1}. The resulting surface waveform was given by $a_0(x) = 0.1 + 0.0075 sin\left(\frac{2\pi x}{0.15}\right)$ where all dimensions are in mm. The tool had a nominal rake angle of α = 0°, and included angle of β = 30° and a clearance angle of 60°. The effective rake angle varied continuously along the surface wavelength due to the imposed sinusoidal vertical velocity. The effective rake angle is related to the ratio of the lateral and vertical velocities as $\alpha_{eff} = -tan^{-1}\left(\frac{v_y}{v_x}\right)$ which, for the present conditions, varied over the range α_{eff} = [-17.44°, 17.44°]. Additionally, several conventional surface generation experiments were also conducted with v_y = 0 to enable in situ characterization of the deformation field.

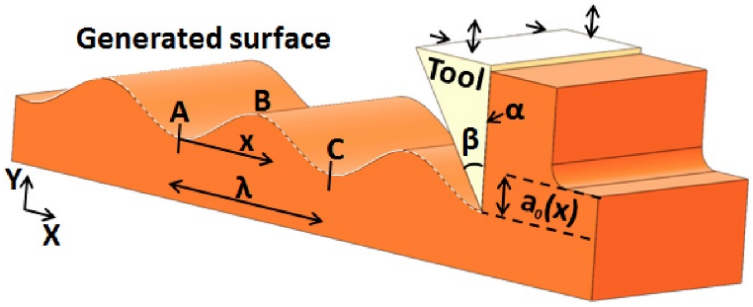

Figure 6-1 Experimental configuration for transient surface generation.

6.3 Wedge-Based Severe Plastic Burnishing

6.3.1 In Situ Characterization of Deformation Fields

The velocity fields resulting from deformation imposed during SPB were characterized using DIC of motion of asperities on the workpiece surface. Subsequently, the effective strain rate fields were extracted from these velocity fields as: $\bar{\dot{\varepsilon}} = \sqrt{\frac{2}{3}\dot{\varepsilon}_{ij} : \dot{\varepsilon}_{ij}}$.

Figure 6-2(a)-(f) show these velocity and effective strain rate fields, characterized within a finite time interval of 0.1 s.

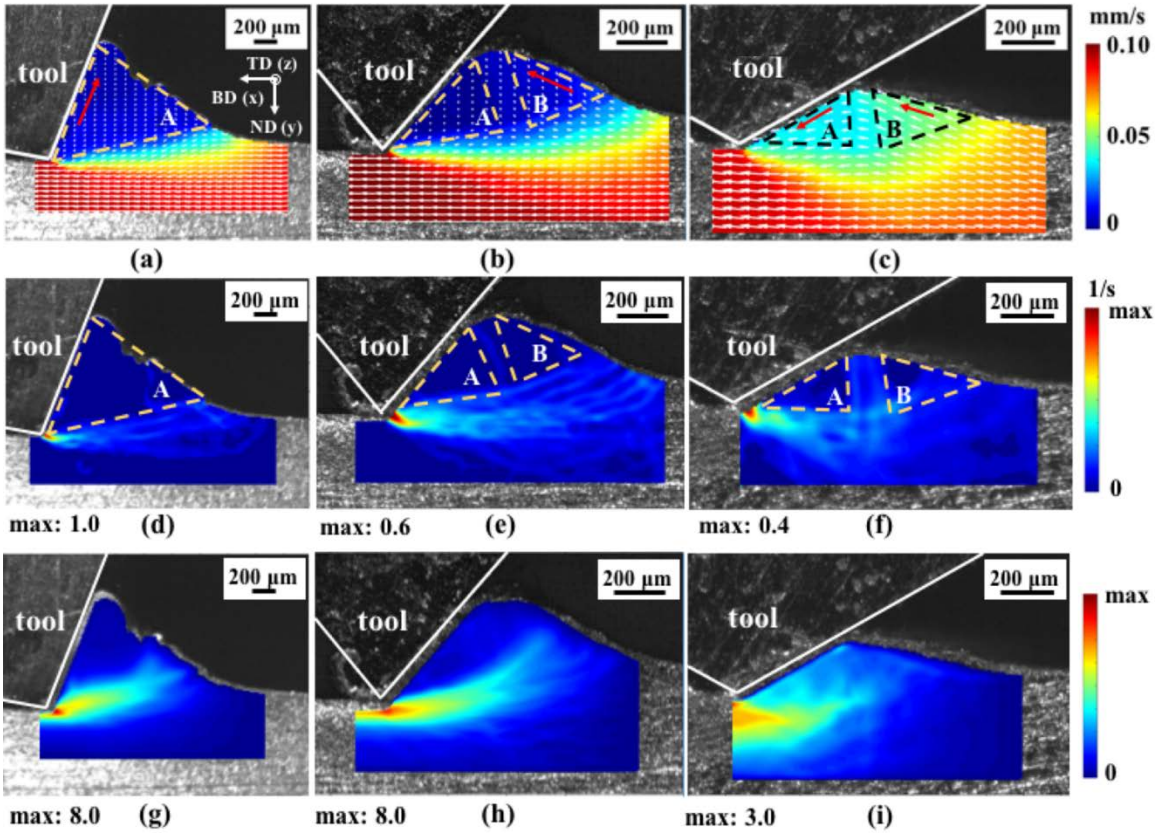

Figure 6-2 DIC-obtained velocity fields overlapped on images of the wedge-based surface deformation process with incident wedge angle of (a) -20° (b) -40° and (c) -60°. Direction of white arrows indicate magnitude and direction of the local velocity vector. Effective strain rate fields (d)-(f) and effective strain fields (g)-(i) for incident wedge angles of -20°, -40°, and -60°, respectively.

Herein, Figure 6-2(a) shows the material flow for α = -20°, where material in region A flowed along the face of the wedge-shaped tool at a constant rate of 0.01 mm/s. The

primary shear zone extending from the tip of the wedge to the free surface as shown in Figure 6-2(d) exhibited a peak strain rate of $\bar{\dot{\varepsilon}}$ ~ 1.0 s^{-1}. From the corresponding effective strain field of Figure 6-2(g), it was seen that deformation in region A was negligible ($\bar{\dot{\varepsilon}}$ < 5% peak strain rate) and material within a zone ahead of the tool and in the subsurface dominantly accommodated the aforementioned deformation. At wedge angle α = -40°, as in Figure 6-2(b), the deformation field was markedly different. For this condition, two distinct regions were observed: (1) a triangular region of stagnated material flow (region A) with v ~ 0 mm/s anchored to the tool face and (2) a region of material flow (region B) abutting the stagnated material flow region A and moving with velocity v ~ 0.015 mm/s. The formation of the dead zone ahead of the tool, i.e. region A, resulted in a modified effective shape to the wedge on the plastic field, with a more negative effective inclination angle of α ~ -75°. Nonetheless, the morphology and shape of the primary shear zone was similar as that occurring above at α = -20°, with a peak strain rate of $\bar{\dot{\varepsilon}}$ ~ 0.6 s^{-1} observed in Figure 6-2(e). Formation of stagnant material zones has been observed before during SPB involving negative rake angles [141].

At a wedge angle of α = -60° shown in Figure 6-2(c), there is a clear absence of material stagnation in the flow field. A relatively stable prow of material forms ahead of the wedge and propagates in a wave-like manner towards the tool (see movie in supporting information). Herein, it was realized that material in the surface left in the wake of the tool after SPB originated from a zone near the surface of the pristine workpiece. Further, this material followed a path of continuous flow through regions B and A in Figure 6-2(c) with velocities of 0.055 mm/s and 0.040 mm/s, respectively. A peak strain rate of $\bar{\dot{\varepsilon}}$ ~ 0.4 s^{-1} was observed in this process, as shown in Figure 6-2(f). A secondary shear zone located at

the interface between regions A and B aligned along ND in the stable prow was observed with material in this region exhibiting a strain rate of $\bar{\dot{\varepsilon}} \sim 0.15\ s^{-1}$. The resulting strain fields for each of these experimental conditions are shown in Figure 6-2(g)-(i), respectively.

The temporal evolution of Lagrangian strain tensor components in material in the vicinity of the surface treated by SPB is shown in Figure 6-3(a). It is evident from this figure that simple shear deformation dominates the surface. In this regard, the shear strain rate ($\dot{\varepsilon}_{xy}$) field exhibited large maxima in magnitude compared to that of normal components ($\dot{\varepsilon}_{xx}$, $\dot{\varepsilon}_{yy}$). This is shown in Figure 6-3(a) where maximum shear strain rates with α = [-20°, -40°, -60°] were $max(\dot{\varepsilon}_{xy})$ = [0.45 s^{-1}, 0.36 s^{-1}, 0.37 s^{-1}], respectively. Nonetheless, a decrease in rake angles to more negative values resulted in a proportionally larger strain rate component along ND and BD in comparison to the aforementioned shear component. Here, a max($\dot{\varepsilon}_{xx}$, $\dot{\varepsilon}_{yy}$) = [0.29 s^{-1}, 0.18 s^{-1}, 0.22 s^{-1}] was seen for α = [-20°, -40°, -60°], respectively. Prior investigations have shown that such characteristics of deformation strongly influence the rate and characteristics of microstructure evolution during SPD [48,57,126]. In this regard, consequences of this effect are discussed in the forthcoming sections.

Effective strain fields in the subsurface region were calculated by integrating effective strain rates along pathlines characterized using DIC. The effect of incident wedge angle on subsurface straining is summarized in Figure 6-3(b), wherein the deformation levels in the work subsurface were normalized by the engagement depth (d/h). The spatial distribution of strain was fitted empirically in the form of $\varepsilon = c_1 \exp(c_2 d/h)$, where c_1 is the residual plastic strain imposed at the work surface and c_2 is a constant indicating rate

of decrease in strain with respect to subsurface depth. The exponential form of this trend was motivated from prior work involving machining of brass [133]. In this regard, c_1 ~ [6.6, 8.3, 2.5] and c_2 = [-2.1, -1.9, -0.5] were found for the incident wedge angles of α = [-20°, -40°, -60°], respectively. The lower values of c_1 and c_2 for α = -60°, compared with those for α = -20° and α = -40° indicate a change in material behavior at extremely negative rake angles during SPB. Microstructural underpinnings of the same are delineated in the forthcoming sections.

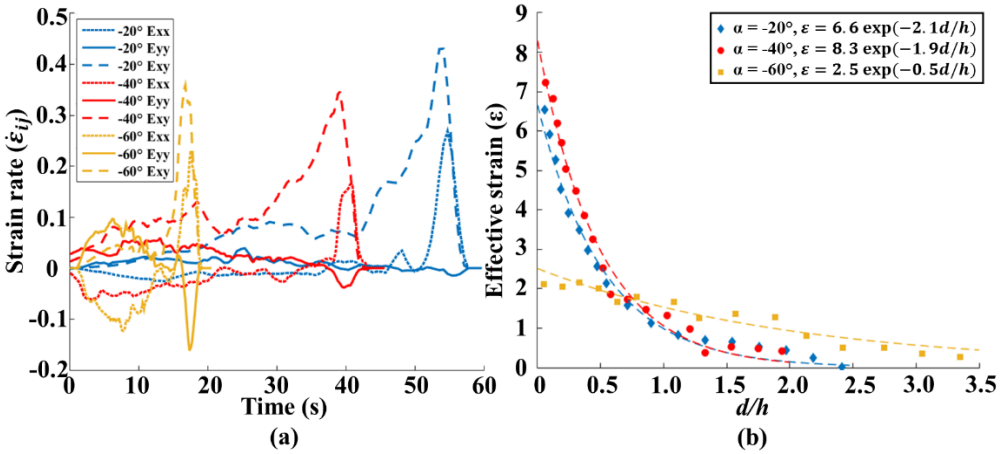

Figure 6-3 (a) Evolution of Lagrangian strain rate tensor components ($\dot{\varepsilon}_{ij}$) with respect to the time elapsed. (b) Variation of strain with the normalized depth (d/h) from the deformed material surface.

6.3.2 Surface Microstructural Characterization

Figure 6-4(a)-(c) show OIM of microstructures characterized near the surface, i.e. d/h ~ 0, after wedge-based SPB with α = [-20°, -40°, -60°], respectively. For a wedge angle of α = -20°, which corresponded to (ε, $\bar{\dot{\varepsilon}}$) ~ (6.6, 1.0 s^{-1}), moderately elongated

UFGs parallel to the burnishing direction were formed with $\delta_{5^\circ} \sim 0.15$ μm. Here, δ_{5° refers to the average size of grains surrounded by boundaries with a misorientation angle of $\theta > 5°$. At a more negative wedge angle of α = -40°, which corresponded to $(\varepsilon, \bar{\dot{\varepsilon}}) \sim$ (8.3, 0.6 s^{-1}), nano-scale grains elongated along BD with $\delta_{5^\circ} \sim 0.25$ μm were observed. For α = -60°, progressively less refinement was observed due to moderate straining with $(\varepsilon, \bar{\dot{\varepsilon}}) \sim$ (2.5, 0.4 s^{-1}), with elongated grains featuring $\delta_{5^\circ} \sim 0.39$ μm. Here, larger grain sizes were also accompanied by grain aspect ratios with increasing deviation from unity at more negative incident wedge angles (Figure 6-4(d)).

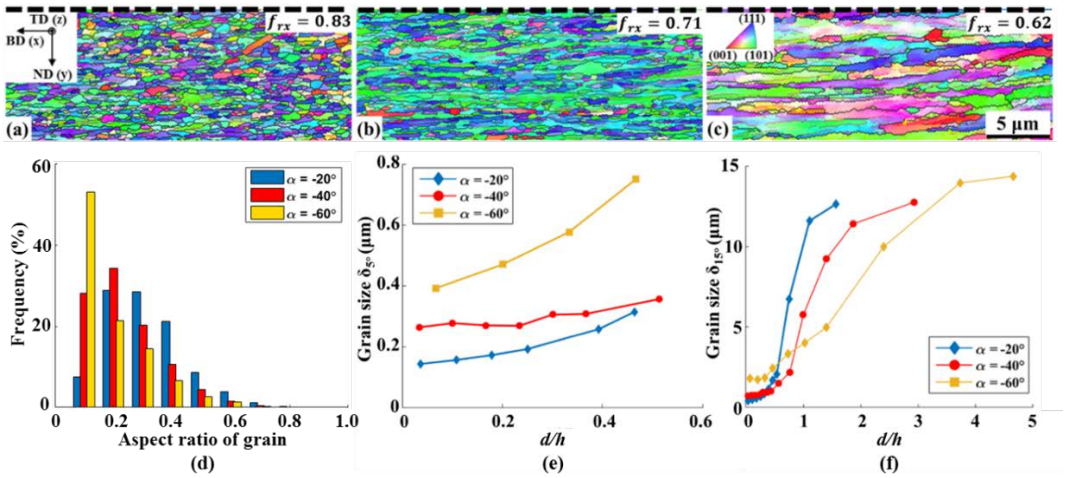

Figure 6-4 OIM images of subsurface microstructure on the TD plane close to the burnished surface ($d \sim$ 3–14 μm) with incident wedge angles of (a) -20°, (b) -40° and (c) -60°. (d) Corresponding statistical distribution of grain aspect ratio. Variation of grain size with respect to the normalized depth (d/h) from the processed surface, defined by (e) > 5° misorientation, δ_{5°, and (f) > 15° misorientation, δ_{15°.

The variation in average grain sizes (i.e., δ_{5° and δ_{15°) with respect to normalized depth of engagement d/h from the burnished surface was characterized by OIM and is summarized in Figure 6-4(e)-(f). The average grain size increased monotonically with increasing depth, with a minimum grain size occurring near the SPB treated surface. In this regard, the increase in both δ_{5° and δ_{15° deeper into the subsurface is consistent with the measured deformation gradient as shown in Figure 6-3(b), this exhibiting $\frac{\partial \varepsilon}{\partial (d/h)} < 0$. Herein, decreasing maximum values of $\frac{\partial \delta}{\partial (d/h)}$ = [18.5, 8.7, 3.4] were determined for α = [-20°, -40°, -60°]. From grain size data, the thickness of the deformed layer was approximated as d/h = [1.9, 3.0, 4.8] for α = [-20°, -40°, -60°], respectively.

The progression of recrystallization during SPB was characterized as the fraction of high angle grain boundaries (HAGB) in terms of boundary length as: $f_{rx} = l_{HABG}/(l_{HABG} + l_{LAGB})$. Here, l_{HABG} and l_{LAGB} are lengths of high (θ > 15°) and low (15° > θ > 2°) angle grain boundaries, respectively. This fraction assumes a high value f_{rx} ~ 1 at the commencement of recrystallization when low angle dislocation boundaries characterized by 15° > θ > 2° are annihilated. In this regard, high recrystallization fractions have been seen as a consequence of continuous dynamic recrystallization (CDRX) during SPD and S^2PD processes [44]. Further, a monotonically increasing relationship has been observed between parameter f_{rx} and imposed effective strains ε during machining based SPD of OFHC Cu [108]. The recrystallization fractions in our SPB experiments for α = [-20°, -40°, -60°] were f_{rx} = [0.83, 0.71, 0.62] respectively at a normalized depth d/h = 0. The corresponding levels of imposed effective strains were ε = [6.6, 8.3, 2.5]. These values evolved to f_{rx} = [0.71, 0.70, 0.63] and f_{rx} = [0.49, 0.56, 0.52] at normalized depths of d/h

= [0.5, 0.4, 0.5] and d/h = [1.1, 1.5, 3.0] as in Figure 6-5(a)-(c) and Figure 6-5(d)-(f), respectively. Empirically characterized effective strains at these depths, were ε = [2.3, 3.9, 2.0] and ε = [0.7, 0.5, 0.6], respectively. A high recrystallization fraction of f_{rx} = 0.83 at ε = 6.6, along with near equiaxed grain morphologies during SPB with α = -20° indicates the onset and near commencement of CDRX. However, this trend was not observed in samples processed using SPB with more negative rake angles. The surface left in the wake of the tool during SPB with α = -40° featured a smaller recrystallization fraction of f_{rx} = 0.71, despite featuring a larger strain of ε = 8.3. This anomaly is analyzed in the forthcoming sections.

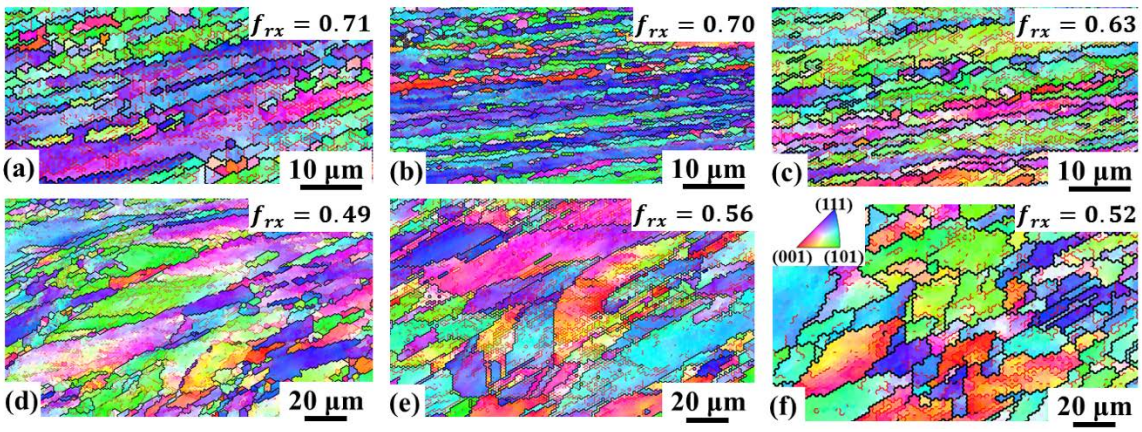

Figure 6-5 OIM of the microstructure at normalized depth (d/h) with incident wedge angle (a) d/h = 0.5, α = -20°, (b) d/h = 0.4, α = -40°, (c) d/h = 0.5, α = -60°, (d) d/h = 1.1, α = -20°, (e) d/h = 1.5, α = -40°, (f) d/h = 3.0, α = -60°. Red lines and black lines demarcate boundaries featuring disorientation θ > 2° and θ >15°, respectively.

Figure 6-6 shows the OIM-characterized sections of the ODF featuring φ_2 = {0°, 15°, 30°, 45°, 60°, 75°, 90°}. These sections were characterized from material in the vicinity of the surface left after SPB and exhibited three dominant fibers outlined in solid black lines in Figure 6-6. Comparison with shear based processes such as machining [57] and plane strain compression [132] indicated a similar evolution of crystallographic textures in SPB. Herein, textures obtained from surfaces treated by SPB with α = [-20°, -40°] exhibited high concentrations along fibers in close vicinity with respect to $f1$, $f2$, and $f3$ fibers that evolve in simple shear. The $f1$ fiber is composed of the {111} partial fiber and starts at the $A_{1\theta}^{*}$ component, passes through $A_\theta/\bar{A}_\theta$ and ends at the $A_{2\theta}^{*}$ component. The $f2$ fiber constitutes both {111} and ⟨110⟩ partial fibers, wherein the {111} partial fiber starts from C_θ, passes through $B_\theta/\bar{B}_\theta$ and ends at $A_\theta/\bar{A}_\theta$. The ⟨110⟩ partial fiber starts at $A_\theta/\bar{A}_\theta$ and ends at $A_{1\theta}^{*}$. The $f3$ fiber is symmetrical with respect to the $f2$ fiber and is composed of the C_θ, $B_\theta/\bar{B}_\theta$ and $A_\theta/\bar{A}_\theta$ in the ⟨110⟩ partial fiber and the $A_\theta/\bar{A}_\theta$ and $A_{2\theta}^{*}$ in the {111} partial fiber. The locations of each ideal component are summarized in Table 1. The C_θ component exhibited the largest strength in these fibers, featuring $f\left(g_{C_\theta}\right)$ = [10, 17] after SPB with α = [-20°, -40°], these featuring surficial strains ε = [6.6, 8.3], respectively. In this regard, the parameter $\max\{f\left(g_{C_\theta}\right)\}$ exhibits a monotonic relationship with respect to effective strains imposed on the surface as seen in simple shear based processing. The pole figures shown in Figure 6-6 also corroborated this similarity. In contrast, textures produced in material treated with SPB featuring α = -60° exhibited fibers that shared a strong resemblance with plane strain compression (i.e., rolling [142]). Reasons behind this deviation at α = -60° with respect to α = [-20°, -40°] are discussed in the next section.

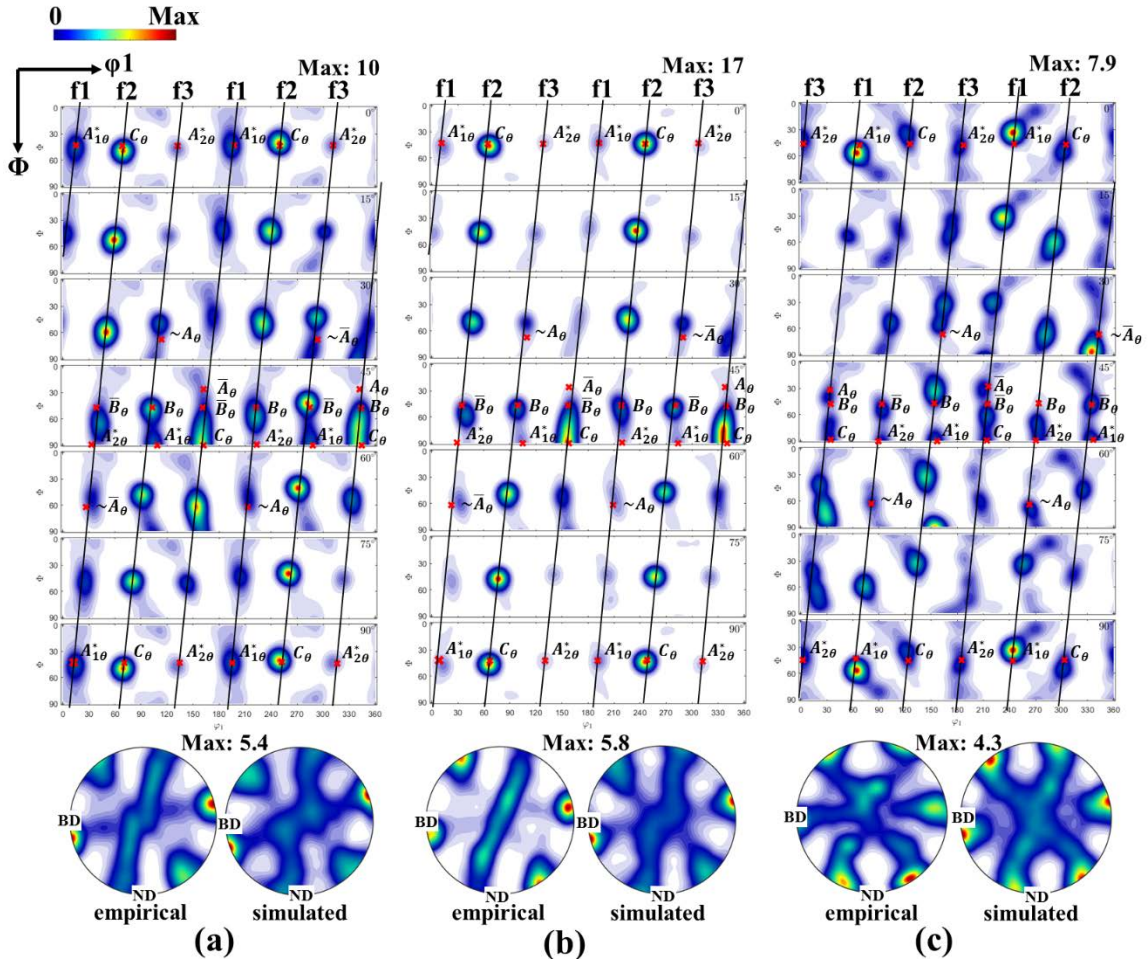

Figure 6-6 The empirical obtained orientation distribution functions and (111) pole figures with (a) α = -20° (b) α = -40°, and (c) α = -60°. The simulated textures were predicted using DIC+VPSC framework. Black dashed lines indicate the partial fiber and red crosses indicate the ideal shear texture components in FCC material.

Table 1. The ideal orientations of shear textures undergoing burnishing processes in Cu.

	α (°)	Euler angles (°)		
		φ_1	Φ	φ_2
$A_{1\theta}^{*}$	-20	18.37	45	0
	-40	12.37	45	0
	-60	70.37	45	0
$A_{2\theta}^{*}$	-20	127.74	45	0
	-40	121.74	45	0
	-60	179.74	45	0
A_{θ}	-20	343	35.26	45
	-40	337	35.26	45
	-60	35	35.26	45
$\bar{A}_{\theta}$	-20	163	35.26	45
	-40	157	35.26	45
	-60	215	35.26	45
B_{θ}	-20	103	54.74	45
	-40	97	54.74	45
	-60	35	54.74	45
$\bar{B}_{\theta}$	-20	43	54.74	45
	-40	37	54.74	45
	-60	95	54.74	45
C_{θ}	-20	73	45	0
	-40	67	45	0
	-60	125	45	0

6.3.3 Discussion

A comparison of empirically characterized microstructure and quantified deformation fields of SPB indicate presence of process anomalies. These anomalies encapsulated non-monotonic fluctuations in imposed effective strains with respect to SPB process variable α. Further, the fractional recrystallization content f_{rx} in microstructures left in the surface in the wake of the tool exhibited a non-monotonic variation with respect to imposed effective strains. This behavior is in contrast with prior observations made in OFHC Cu in comparable deformation geometries, wherein monotonic relationships between f_{rx} and imposed effective strains were seen. The forthcoming sections attempt to delineate these anomalies.

6.3.3.1 Mechanics and microstructure evolution in surface severe plastic deformation

Understanding the correlation between subsurface deformation levels and process parameters is critical for a generalized framework for predicting the resulting surface and subsurface microstructure. From the data of the present study, a response surface was mapped and is shown in Figure 6-7(a), this relating strain levels to incident wedge angle and normalized subsurface depth. As shown in the figure, less negative incident wedge angles tend to induce higher peak subsurface strains up to $\varepsilon \sim 8$ at the work surface, while also producing smaller deformed subsurface layers. In contrast, more negative incident wedge angles exhibit the opposite effect with a maximum normalized deformed layer thickness of 5 for $\alpha \sim -70°$. This mapping of subsurface deformation mechanics provides a generalizable framework for selecting S^2PD parameters to achieve specific deformation levels and subsurface strain distributions.

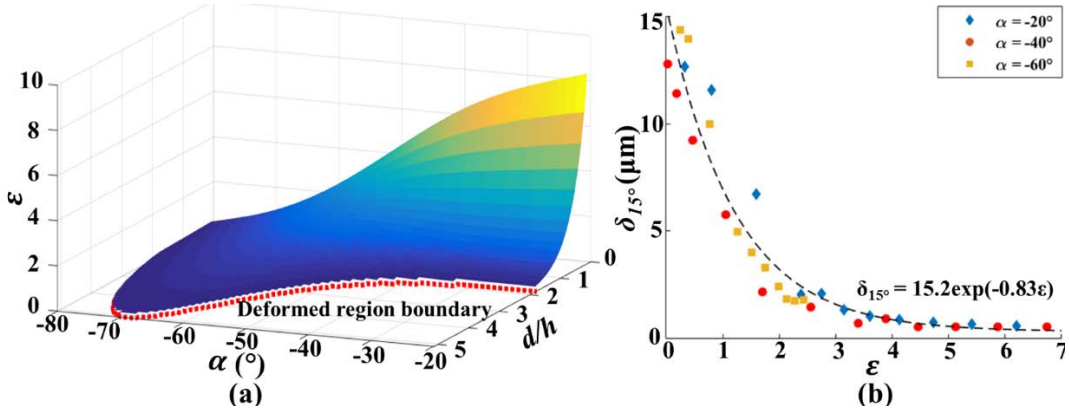

Figure 6-7 (a) Effective strain field induced by surface deformation process with respect to incident wedge angle (α) and normalized subsurface depth (d/h). The red dashed line indicates the boundary of deformed region within the strain threshold of $\varepsilon > 0.2$. (b) The variance of grain size with respect to effective strain.

The microstructure of polycrystalline metallic systems evolves with the interplay of dislocation and twinning during imposition of severe strains. The correlation between average grain size and the imposed plastic strain in the surface/subsurface across the range of incident wedge angles is shown in Figure 6-7(b). From the figure, the grain size decreased exponentially with respect to increasing strain with the relationship $\delta_{15^\circ} = 15.2 \times e^{-0.83\varepsilon}$. At near ambient temperatures, consequences of this interplay, *viz.* fragmentation and concomitant generation of new domains surrounded by high angle grain boundaries can be classified in continuous or geometric dynamic recrystallization (CDRX or GDRX) processes. CDRX involves the progressive fragmentation of grains by the formation and consolidation of dislocation cell structures. These structures feature differential disorientations with respect to their neighbors. Upon accumulative straining, these disorientations grow in magnitude through the plastic rotation of their respective lattice orientations. On the other hand, GDRX involves shear based pancaking of grains with concomitant serration of grain boundaries. When the serrations in facing boundaries of the grain approach each other in close proximity, the original grain pinches off into several offspring grains, thereby resulting in fragmentation. Both CDRX and GDRX have been observed during shear based surface generation by machining. In this regard, their presence in SPB indicates similarities in the mechanics governing material response across machining and burnishing.

The mechanics of material response as described above is mediated by the imposed deformation during the advancement of wedge tool. This boundary condition naturally results in generation of large cutting and thrust forces on the material that exists in the vicinity of the tool along its path of travel [143]. The components of these forces along the

shear plane administering the primary deformation zone results in a dislocation based material response culminating in CDRX and GDRX. Herein, this response has been encapsulated in a phenomenological framework that prescribes a monotonic exponential growth of the recrystallization fraction (i.e., f_{rx}) with respect to imposed effective strains ε. In this regard, the non-negligible decrease of f_{rx} = 0.83 for α = -20° and ε = 6.6 to f_{rx} = 0.71 for α = -40° and ε = 8.3 is indicative of an anomalous deviation in the mechanics of material response across the two conditions in the present SPB experiments. This behavior indicates lower levels of continuous recrystallization despite imposition of larger strains during SPB at extremely negative rake angles.

Sources of the aforementioned anomaly in SPB can be found in evolution of the dynamics of machining at comparable process parameters. Progressively negative rake angles have been shown to instigate the generation of larger thrust forces at the expense of smaller cutting forces during machining and SPB. At very negative rake angles, this effect will naturally result in smaller resolved shear forces along the aforementioned shear plane, wherein it is anticipated that the rate of microstructure evolution as described in the previous paragraph will be subdued. This hypothesis was tested by characterization of the Lagrangian strain tensor field under the surface undergoing SPB with α = -60° with measured strain components of (ε_{xy}, ε_{xx}, ε_{yy}) = (1.8, 0.7, -0.4) indicating significantly larger normal strains in comparison with shear strains. In contrast, experimental conditions of α = -20° and α = -40° resulted in tensor components of ($\varepsilon_{xy}, \varepsilon_{xx}, \varepsilon_{yy}$) = (6.0, 1.1, -0.5) and ($\varepsilon_{xy}, \varepsilon_{xx}, \varepsilon_{yy}$) = (5.3, 0.8, -0.3), respectively. In this regard, we also note that plane strain compression has been shown to result in a smaller rate of lattice rotation at comparable effective strain rates, in contrast with deformation by simple shear [132]. The

net effect of these phenomena is an apparent decrease in the recrystallization fraction despite larger strains resulting from the process configuration involving more negative α. The observation that $\frac{\partial f_{rx}}{\partial \varepsilon} < 0$ over the processing space explored in the present study is suggestive of fundamental processing limits on recrystallized microstructures achievable through shear based surface generation in machining and SPB depending on the nature of the mechanics imposed. This aspect will be discussed in the forthcoming sections.

6.3.3.2 Evolution of surface crystallographic texture

The VPSC framework was used to simulate the evolution of surface and subsurface crystallographic textures during SPB. The framework utilized a simple Voce hardening law and results from the same are shown in Figure 6-8. Quantitative examination of the simulated textures with respect to their empirically measured counterparts is summarized in Table 2.

Table 2. The variation of texture index (T) and normalized texture index ($\hat{T}_d$) of the experimental and simulated textures with respect to incident wedge angle (α).

	α = -20°		α = -40°		α = -60°		Initial texture	
	Measured	VPSC	Measured	VPSC	Measured	VPSC	Measured	VPSC
T	3.2	3.0	4.9	4.5	2.6	2.5	1.2	1.2
$\hat{T}_d$	0.36		0.27		0.29		0.01	

The index (T) of simulated textures was T = [3.2, 4.9, 2.6] for α = [-20°, -40°, -60°] at $d/h \sim 0$, respectively. These values closely matched that of the empirical counterparts obtained from OIM (i.e., T = [3.0, 4.5, 2.5]). This is also confirmed by corresponding values of normalized texture index $\hat{T}_d$ = [0.36, 0.27, 0.29] for α = [-20°, -40°, -60°], respectively.

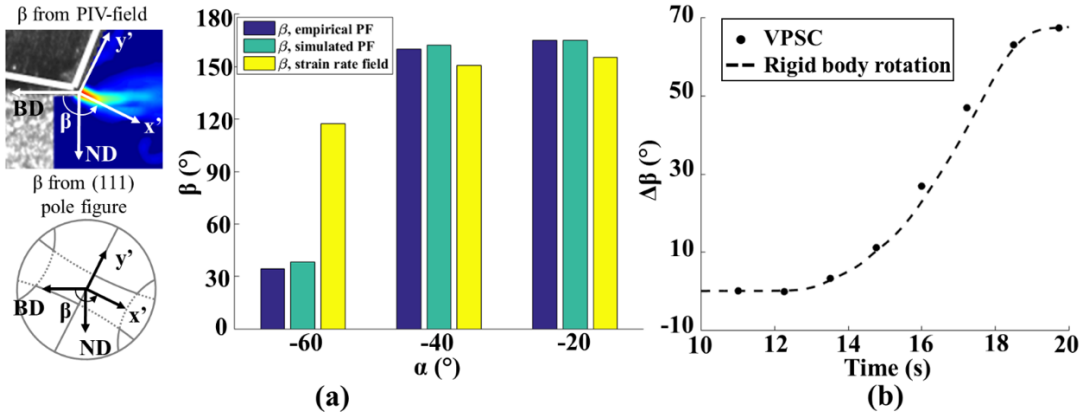

Figure 6-8 (a) Schematic representation of tilting angle (β) measurement based on (111) pole figure and deformation field and summary of β with respect to incident wedge angle (α) (b) The change of β ($\Delta\beta$) with respect to the processing time with α = -60°.

As the evolved texture was found to deviate from the ideal positions of shear texture components, rotation of the partial fibers can be observed in Figure 6-8. Deformation-based processing techniques based on simple shear have been linked elsewhere to rotated ideal texture components [139,140]. To quantify the presence of such phenomenon in the wedge-based SPB process, the tilt angle (β) of the texture was measured for each processing condition in the present study. As shown in Figure 6-8(a), the x' axis in the $x' - y'$

coordinate system is defined to be orthogonal to the ⟨110⟩ fiber and approximately parallel with the shear plane measured in the DIC-obtained deformation fields. The tilt angle was defined as the angle between x' axis and direction BD. Figure 6-8(a) summarizes the texture tilt angle as measured from the empirically obtained (111) pole figures, the simulated (111) pole figures and the effective strain rate field. From the figure, relatively good agreement is seen with the measured and simulated tilt angles for α = [-20°, -40°] in the range of 150°. However, a large difference of ~75° was observed between the measured/simulated pole figures and the rotation in the strain rate field for α = -60°.

In comparison with α = [-20°, -40°], textures obtained from α = -60° exhibited considerable deviations with respect to crystallographic textures obtained in simple shear based processing. Sources of this behavior can be traced to corresponding deviations across deformation fields imposed on surfaces treated with SPB with α = [-20°, -40°] and α = -60°, respectively. The former process conditions result in significantly larger contributions to the final microstructure from the simple shear components of the Lagrangian deformation tensor, where $(\varepsilon_{xy}, \bar{\varepsilon})$ = (6.0, 6.6) for α = -20° and $(\varepsilon_{xy}, \bar{\varepsilon})$ = (5.3, 8.3) for α = -40°. In contrast, the experimental measurements with α = -60° revealed that the normal components of the deformation tensor along BD and ND resulted in $(\varepsilon_{xx}, \varepsilon_{yy})$ = (0.7, -0.4), which accounts for a significantly larger portion of the imposed effective strain, $\bar{\varepsilon}$ = 2.5. The differences in the nature of the strain tensor result in the crystallographic textures exhibiting characteristics of plane strain compression (i.e., rolling). These were confirmed in Fig 8(b). The evolution of tilt angle ($\Delta\beta$) in the simulated texture is closely matching the rotation angle calculated by strain tensor components.

The above results indicate the limitation of the simple shear assumption for a wedge-based SPB process. These *in situ* subsurface deformation field measurements revealed that shear and plane compression/tension result in the misalignment between texture orientation and principal shear direction. Similar observations have also been reported in the shear textures produced by ECAE configuration, where the positions of ideal shear texture components are shown to be rotated away from the extrusion direction by 10° - 20° [144]. In this regard, a better understanding of the interactive effects of shear and compression/tension strain would be of importance to provide accurate texture modelling in SPD configurations. Although decoupling the combined effect of individual strain components in SPB processing is non-trivial, textures produced by plane strain tension alone have been found to be similar to those by simple shear, this resulting in an accelerated rate of texture development [63]. In this research, the overall effective strain level can be effectively used to predict the texture strength, given the linear correlation of texture index (i.e., T = [1.2, 2.6, 3.2, 4.9]) and overall effective strain level (i.e., $\bar{\varepsilon}$ = [0, 2.5, 6.6, 8.3]). However, an excessive level of deformation (i.e., $\bar{\varepsilon} > 10$) imposed by multiple passes is expected to result in weaker texture due to the effects of dynamic recrystallization [145].

6.3.3.3 Implications on microstructure tailoring frameworks based on shear-based surface processing

The aforementioned results suggest presence of fundamental limits on frameworks for tailoring microstructures for endowing fabricated components with enhanced functional characteristics. Traditional deployment of frameworks that have been formulated for simple shear-based surface processing would prescribe more negative rake

angles for imposition of larger effective surficial strains. In turn, larger strains would be anticipated to give rise to a larger recrystallization fraction. Herein, an implicit assumption in such frameworks is the dominance of the simple shear component in the Lagrangian strain tensor. However, the current research clearly shows that salient aspects of the deformation field in shear-based surface processing undergo a switchover at extremely negative rake angles. This switchover instigates a dominance of plane strain compression during shear-based surface processing. Consequently, the predictions of simple shear calibrated microstructure-tailoring frameworks, for instance those described in Refs. [16,57] require further validation across larger swathes of the thermomechanical space and process configurations.

6.4 Shear-Based Transient Surface Generation

6.4.1 Microstructure Characterization

Figure 6-9(a) shows OIM of the heterogeneous surface topography from which microstructure parameters pertaining to gradients in grain diameter (δ), recrystallization fraction (f_{rx}), dislocation structure orientation and crystallographic texture were extracted. From the figure, a high concentration of UFGs was seen across the entire surface wavelength in the immediate subsurface, compared to microcrystalline grains observed at greater subsurface depths. Figure 6-9(b) summarizes grain size δ_{2° measurements as a function of depth in the direction of the surface normal (d) for two locations along the surface wavelength. From the figure, the gradient in grain size was steeper for $\frac{\mathrm{x}}{\lambda} \sim 0.6$ in comparison to $\frac{x}{\lambda} \sim 0.35$, wherein grain size δ_{2° denotes grains comprised of boundaries

having misorientation greater than 2°. The gradient in grain size $\left(\frac{\partial \delta_{2^\circ}}{\partial d}\right)$ observed here is similar to that noted elsewhere for conventional material removal configurations [133].

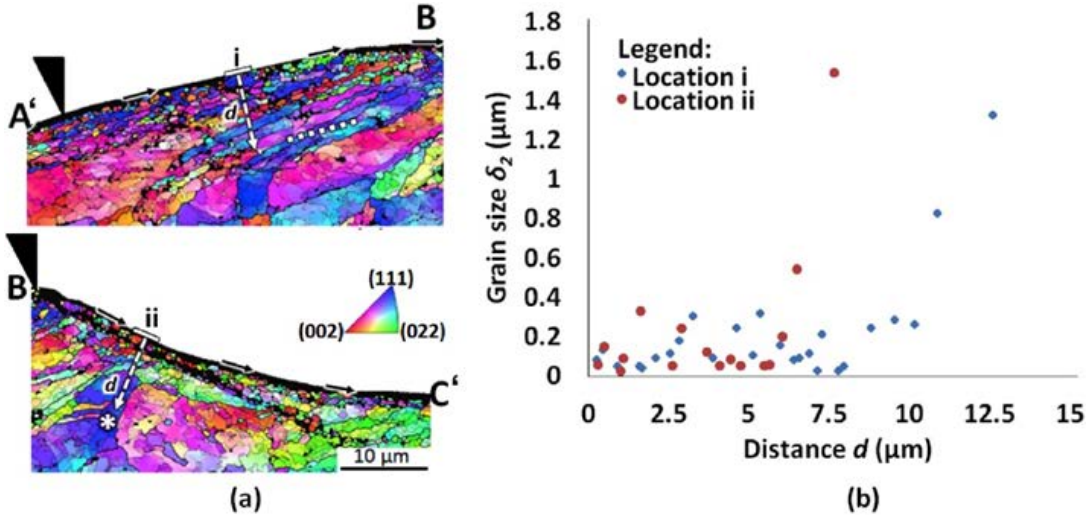

Figure 6-9 (a) OIM of subsurface microstructure characterized using EBSD for A'B with $\frac{x}{\lambda}$ = [0.2, 0.5] and BC' with $\frac{x}{\lambda}$ = [0.5, 0.8]. (b) Gradient in grain size δ_{2° with respect to increasing distance d along lines marked using i and ii.

Figure 6-10 shows higher resolution OIM of the subsurface microstructure field. The dashed white line in Figure 6-10(a) demarcates the zone abutting the surface exhibiting presence of UFGs with δ_{15° < 0.5 µm. From the micrograph, it is clear that this UFG layer thickness d_{ufg} varied with respect to location along the surface wavelength. This variation, illustrated in Figure 6-11, exhibits global and local maxima that are identified in the figure with arrows. The global maximum identified at $\frac{x}{\lambda}$ ~ 0.17 corresponds to the location approximately halfway between points A and B in Figure 6-10(a). The smaller local maxima at $\frac{x}{\lambda}$ ~ 0.6 corresponds to the zone within the dotted ellipse near apex B in Figure

6-10(a). The UFG surficial zones exhibited pancake shaped grains with serrated boundaries impinging onto the surface, identified using white arrows in Figure 6-10(a) and magnified in Figure 6-10(b). These features are indicative of geometric dynamic recrystallization [15,108] wherein serrations on opposing sides of a grain impinge with imposition of incremental shear and result in formation of several offspring grains.

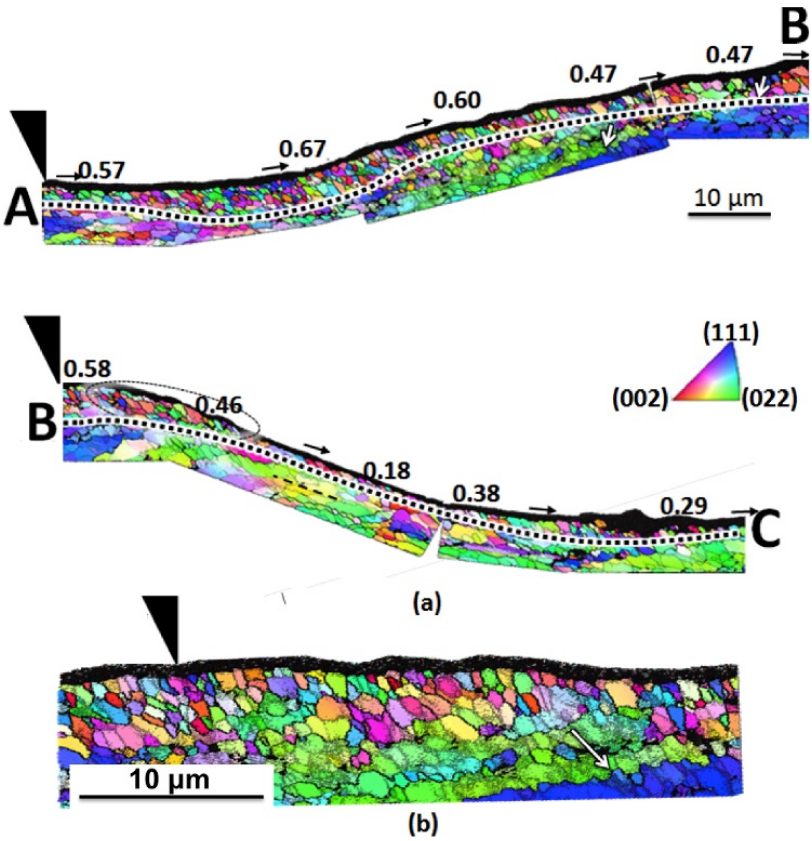

Figure 6-10 (a) High resolution OIM of surficial microstructure in transient surface generation. Numbers overlaid above the surface indicate spatial variation in local recrystallization fraction f_{rx}. (b) Magnified view of the OIM of surficial microstructure characterized halfway between AB at $\frac{x}{\lambda}$ = 0.25.

Extent of recrystallization was quantified by determining recrystallization fraction, given as $f_{rx} = \frac{l_{HAGB}}{l_{LAGB}+l_{HAGB}}$, where l_{HAGB} and l_{LAGB} refer to length of low and high angle grain boundaries featuring disorientations of 2° - 15° and > 15°, respectively. These fractions are shown in Figure 6-11 and are correlated to the UFG layer thickness, wherein the largest recrystallization fraction f_{rx} = 0.67 occurred where maximum UFG layer thickness was observed (e.g., $\frac{x}{\lambda}$ ~ 0.17). Similarly, the smallest recrystallization fraction f_{rx} = 0.18 was observed where the UFG layer thickness was also minimum (e.g., $\frac{x}{\lambda}$ ~ 0.75). Interestingly, recrystallization fraction exhibited a local maximum f_{rx} = 0.58 close to apex B (e.g., $\frac{x}{\lambda}$ ~ 0.6), where a local maximum in UFG layer thickness was also seen. The heterogeneity in recrystallization fraction observed across the surface wavelength is indicative of transient effects in the mechanics of the surface generation.

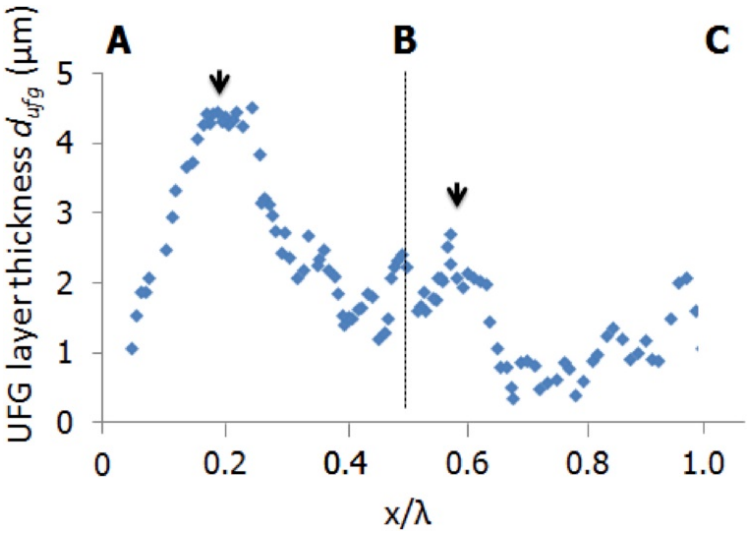

Figure 6-11 Variation in thickness d_{ufg} of the zone exhibiting UFGs $\delta_{15°}$ < 0.5 µm with respect to normalized position along the surface wavelength $\frac{x}{\lambda}$.

Surficial crystallographic textures produced during transient surface generation were extracted from OIM data using the MATLAB based software MTEX [146] and subsequently reoriented in order to facilitate comparison with textures produced in conventional surface generation configurations [57]. This reorientation ensured horizontal (e.g., X direction) in the final ODFs. Herein, sections of the orientation distribution function (ODF) given by φ_2 = {0°, 15°, 30°, 45° 60°, 75°, 90°} are elucidated in Figure 6-12. These crystallographic textures reveal a near $\frac{2}{m}$ symmetry about the X-direction with high concentrations of orientations along fibers outlined using dashed lines. These fibers were coincident with those exhibited by conventional surface generation within experimental error and the intensities exhibited by the ODFs were also within a similar range [57]. However, qualitative examination of the present crystallographic textures suggests a degree of variation within the deformation mechanics during transient surface generation. For instance, crystallographic textures obtained from section e in Figure 6-12 exhibited a larger spread compared with that obtained from other sections.

6.4.2 Discussion

Prior studies have shown that microstructure fields and crystallographic textures resulting from plastic deformation evolve as a consequence of the prevalent thermomechanics characterized in terms of (ε, $\dot{\varepsilon}$, T). For subsurface deformation occurring during surface generation, attempts have been made to describe this triad as a function of deployed processing parameters in terms of tool rake angle a and deformation rate v. Fidelity of frameworks in modeling microstructural consequences resulting from the

deformation imposed during surface generation have been demonstrated across a broad class of materials and thermomechanical subspace [134].

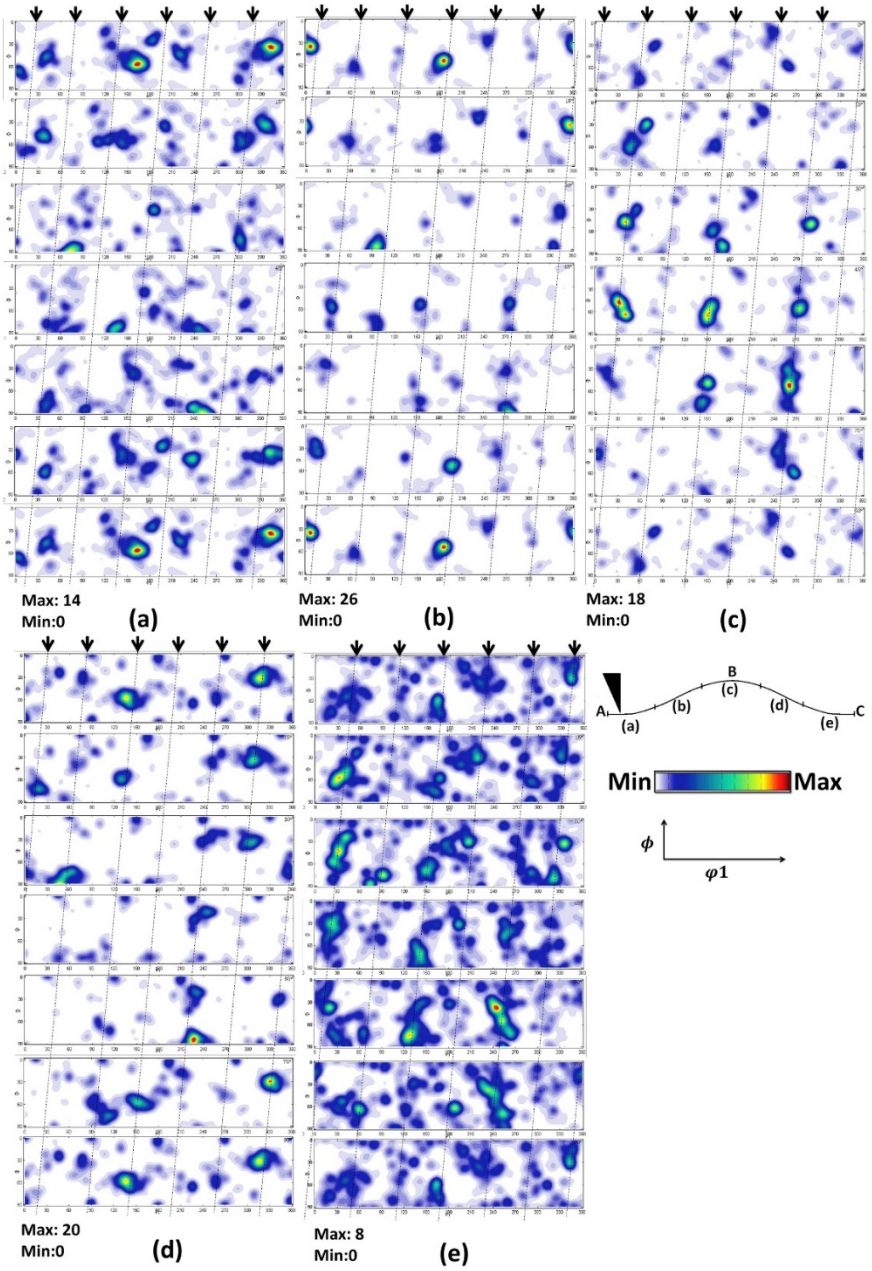

Figure 6-12 Rotated orientation distribution functions characterized using OIM along locations (a-e) identified in the inset on the bottom right. The rows correspond to φ_2 = 0°, 15°, 30°, 45°, 60°, 75°, 90° sections.

The state of the deformed surface in terms of the imposed effective strains in conventional surface generation (i.e., v_y = 0) is given by $\varepsilon_d = \varepsilon_0 exp\left(-K_\alpha \frac{d}{a_0}\right)$, where K_α is a parameter dependent solely on α and ε_0 is the surface effective strain correlated with α through effective strain imposed in the removal volume (chip) [147]. As α is constant in conventional surface generation, the subsurface strain field is a steady-state but spatially heterogeneous deformation field. This is not the case for a transient surface generation process as the effective rake angle takes on a range of values depending on the instantaneous position along the surface waveform. For the experimental conditions explored in the present study, this resulted in $\alpha_{eff} \in$ [-17.44°, 17.44°] during the surface generation process. Further, the DIC measurements yielded $\varepsilon_0 = -0.07\alpha + 3.6$ and $K_\alpha = -0.62\alpha - 140$. The resulting subsurface deformation field is shown in Figure 6-13(a).

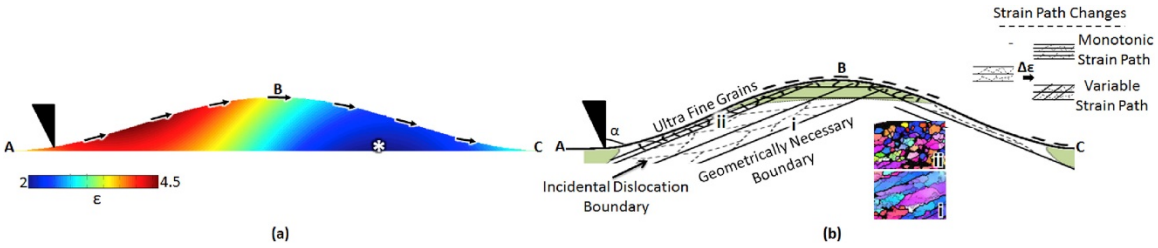

Figure 6-13 (a) Effective strain field imposed on the fabricated topography. (b) Schematic illustrating microstructure evolution in transient surface generation with strain path changes. Inset on right shows effect of strain path changes on accelerated microstructure evolution. These zones are identified using the dashed line.

From the figure, the strain field is heterogeneous along the surface wavelength wherein regions of high strain correspond to the rising surface edge (i.e., α_{eff} < 0) and

regions of low strain correspond to the falling surface edge (i.e., $\alpha_{eff} > 0$). Further, asymmetry in the strain field is clearly evident due to the transient nature of the subsurface deformation field along the surface wavelength.

Comparison of the subsurface effective strain field with the microstructure of the deformed subsurface suggests activation of continuous recrystallization with the imposition of large plastic strain in the subsurface. Imposition of increasing levels of strain generally results in the formation of incidental dislocation boundaries (IDBs) and geometrically necessary boundaries (GNBs). The former results from probabilistic events constituting the statistical interlocking of dislocations whereas the latter results from geometrical necessity in order to maintain material continuity [44]. Progressive imposition of strains causes misorientation featured by IDBs to increase, eventually resulting in their progression to GNBs. The spacing between these boundaries decreases with imposition of larger strains, resulting in microstructure refinement. In this regard, grain refinement within the subsurface during transient surface generation is schematically illustrated in Figure 6-13(b). The microstructure field quantified in Figure 6-9(b) along directions i, ii depicted in Figure 6-9(a) exhibited an increase in grain size δ_{2° harmoniously with respect to decreasing strains along these directions. The microstructure fields also exhibited a similar evolution in dislocation boundaries and their consolidation to form new grains as depicted in insets i and ii in Figure 6-13(b), wherein inset ii in the near surface exhibits a more refined grain structure due to higher imposed strains and that of inset i in the far field exhibits less refinement due to lower imposed strains. This mechanism of microstructure evolution is often accompanied by shear-induced pancaking of grains surrounded by high angle grain boundaries (HAGBs) featuring misorientation $\theta > 15°$. High aspect ratio

pancake-shaped grains tend to develop serrations on their boundaries [108] that eventually subdivide a single grain to several off-spring grains upon pinching with their counterparts in the facing boundary. Herein, instances of grain pancaking and serration were observed near apex B in the surface wavelength, locally identified using the white arrow in the segment AB in Figure 6-10(a) and (b). Finally, the location exhibiting minimum effective strains in the strain field depicted in Figure 6-13(a) using the asterisk corresponds to the zone that exhibits a near-pristine equi-axed grain structure.

Progression in strain induced recrystallization of new grains was quantified by extracting the parameter $f_{rx} = \frac{l_{HAGB}}{l_{LAGB}+l_{HAGB}}$ close to the surface using results obtained from OIM. This characterization is depicted as numbers over the topography in Figure 6-10(a). This parameter, also known as the high angle grain boundary fraction assumes a value close to 1 after recrystallization of new grains, these being essentially defect free upon their genesis and lacking low angle grain boundaries [15,108]. From the present results, f_{rx} exhibited a cyclical variation with respect to location along the surface wavelength. The maximum value of f_{rx} = 0.67 coincided directly with the location $\frac{x}{\lambda}$ = 0.17 that exhibited maximum surficial strain ε~4.8 as well as global maximum in UFG layer thickness d_{ufg} ~ 5 μm. Similarly, the location $\frac{x}{\lambda}$ ~ 0.75 with minimum f_{rx} = 0.18 coincided with lowest surficial strain ε ~ 2.4 and smallest d_{ufg} ~ 0.5 μm. Further positive correlation between f_{rx}, ε and d_{ufg} was seen at other positions along the surface wavelength of $\frac{x}{\lambda}$ = {0.28, 0.40} whereby surface strains of ε = {4.8,4.3} yielded f_{rx} = {0.60, 0.47}, along with a decrease in the UFG layer thickness d_{ufg} = {3 μm, 1.1 μm}. Closer inspection of the coupled variation in f_{rx} and ε in the subsurface revealed evolution that cannot be explained

by a monotonic relationship between these two parameters. For example, a negative correlation between these parameters was observed for $\frac{x}{\lambda}$ = {0.40, 0.51}, which corresponded to ε = {4.3, 3.6} and f_{rx} = {0.47, 0.58}. This feature was reflected onto the observed variation of parameter d_{ufg} which also exhibited an increase from 1 μm to 2 μm across these locations, despite concomitantly decreasing strains. This non-monotonic response is considered in the ensuing.

6.5 Conclusion

In this chapter, material response, microstructure, and crystallographic texture were investigated during wedge-based SPB of OFHC Cu with varying incident wedge angles. Larger peak surface plastic strains and deeper affected surficial regions were observed compared to conventional surface generation processes. It was shown that gradient microstructures formed and could be attributed to the heterogeneous deformation levels imposed on the final processed surface and subsurface. Multiple types of microstructures include nano-scale and micro-scale elongated grains, equiaxed UFG microstructures and coarsely deformed microcrystalline structures were observed. The controllability of the burnishing process was discussed, this providing a direct guide for generating expected surficial microstructure gradients by control of burnishing parameters. Crystallographic textures were characterized experimentally using OIM information, this accompanied by accurate predictions by VPSC coupled with DIC-obtained deformation history. The evolutions of texture in all conditions were evaluated in terms of the texture rotation, this offering a scope for the validation of analytical models for texture evolution in surface severe plastic deformation. Deviations between measured and simulated textures were

analyzed based on differences in the mechanics of surface generation by SPB that arise due to the imposed processing conditions. Additionally, non-monotonic evolution of recrystallization fraction with respect to magnitude of the imposed plastic strain was found to be present due to salient differences in the plastic strain tensor. The implications of these results on surface microstructure control frameworks were explained in terms of corresponding effects on strain tensor components in the processed surface and subsurface. In addition, evolution of subsurface microstructure during transient surface generation in OFHC Cu was also investigated using EBSD-based OIM characterization. The deformed subsurface was found to consist of a graded ultrafine-grained microstructure. In this regard, the thickness of this ultrafine-grained layer was observed to vary as a function of position along the surface wavelength. Analysis of recrystallization fraction in the microstructure of the deformed surface showed evidence of accelerated microstructure evolution and refinement during the imposed surficial deformation.

CHAPTER 7. CONCLUSIONS AND FUTURE WORK

7.1 Summary of Results

In the present research, gradient microstructure control has been investigated in fundamental loading configurations pertaining to unit-type indentation, sequential indentation and sliding on a model strain hardening material. These processing system models are representative models for describing deformation occurring over a range of surface generation processes, including machining, burnishing, sliding, and surface mechanical attrition. The deformation field and severity of the deformation were characterized *in situ* using a DIC-based measurement method and predicted by FE simulations using Abaqus Explicit. Gradients in microstructure and crystallographic texture were experimentally identified using EBSD-based OIM and modeled using the VPSC framework. For reference, the results of these investigations have been archived in refereed publications and conference proceedings [48,106,126,132,148–155]. The primary findings and contributions of this thesis are given as follows for each major type of processing configuration:

Unit indentation-type processes

- A reformulated expanding cavity model with modified deadzone, elastic-plastic and free surface interfacial geometry was shown to provide improved estimates of the deformation in unit-type indentation loading in terms of parameters of interest such as maximum effective strain rate and indentation load for the experimental conditions investigated.

- Accelerated refinement of subsurface microstructure to UFG-scale levels was directly observed and attributed to enhanced local lattice rotation rate associated with non-laminar micro-bends in material flow pathlines close to the interface of the indenter.

Sequential indentation-type processes

- Maximum induced strain and the degree of strain field overlap in the deformed subsurface in sequential indentation were maximized when the ratio of indentation spacing to projected indentation contact length was approximately S/L = 1.1.
- Upper and lower bounds on energy dissipated in controlling strain levels and subsurface strain overlap were mapped. It was shown that efficient combinations of indentation spacing and indentation depth could be used to achieve specific combinations of strain and subsurface overlap.
- Surface strain levels and the extent of the subsurface strained layer were shown to directly relate with the number of impacts on the workpiece surface in directional surface mechanical attrition process via FE simulation and experiments.

Sliding-type processes

- Multiple types of microstructures including nano-scale and micro-scale elongated grains, equiaxed UFG microstructures and coarsely deformed microcrystalline structures were observed in sliding-type process through direct control of burnishing parameters.
- Controllability of subsurface grain size was demonstrated by control of strain levels achieved by changes in rake angle.

- Deviations between measured textures and VPSC-simulated textures were found to be due to differences in the mechanics of surface generation by SPB that arise due to the imposed processing conditions.
- The thickness of the ultrafine-grained layer in transient surface generation was observed to vary as a function of position along the surface wavelength. Analysis of recrystallization fraction in the microstructure of the deformed surface showed evidence of accelerated microstructure evolution and refinement during the imposed surficial deformation due to the variability of the loading path.

7.2 Recommendations for Future Research

The results of the fundamental studies presented in this thesis can be leveraged to control the final microstructure in a deformed by selecting proper MSM-based process parameters. Potential topics for future research are as follows:

- The research described in this thesis has demonstrated the mechanics of surface deformation for a model strain hardening material at relatively lower strain rate to accommodate direct observations of the deformation zone. In this regard, the unit models developed in the present work may vary from the strains present in dynamic attrition processes due to presence of high strain rates. Further, material loss and fracture with increased strains in repeated processing may also contribute to variations in expected behavior. As such, additional investigations on the effects of higher strain rate in the formation of gradient material are applicable in the current setup. Of particular interest are low-to-moderate stacking fault energy metals that may give rise to formation of either growth or deformation twin boundaries in

S^2PD. Nano-twinned materials have shown exceptional combinations of formability, hardenability, and ultimate strength, due to the unique properties of these interfaces. In this regard, formation of gradient microstructure embedded with nano-twinned structure could potentially transform the deformation mechanisms from dislocation-dominated plasticity to twinning-induced plasticity.

- While the present study has focused on a framework for relating process-deformation-microstructure parameters, the specific effects of gradient microstructure on thermomechanical properties and corresponding deformation mechanisms relative to conventional homogeneous microstructures were not explicitly studied. It would be useful to consider the processing implications of the present work on these performance measures of interest. Unique mechanical behavior of functionally graded microstructures has been attributed to either nano-grained or nano-twinned microstructures with varying grain size. The equivalent yield stress in these gradient microstructures has been evaluated in other work based on plasticity models that account for stress gradient plasticity, mean field theory and others. A more comprehensive understanding of the structural behavior of gradient microstructures and possible linkages to processing models such as those in the present study would be beneficial in providing a more comprehensive methodology for the manufacturing-informed design of advanced materials with enhanced mechanical properties.

REFERENCES

[1] Y. Estrin, A. Vinogradov, Extreme grain refinement by severe plastic deformation: A wealth of challenging science, Acta Mater. 61 (2013) 782–817.

[2] L. Huang, J. Lu, M. Troyon, Nanomechanical properties of nanostructured titanium prepared by SMAT, Surf. Coatings Technol. 201 (2006) 208–213.

[3] H.W. Huang, Z.B. Wang, J. Lu, K. Lu, Fatigue behaviors of AISI 316L stainless steel with a gradient nanostructured surface layer, Acta Mater. 87 (2015) 150–160.

[4] H.W. Huang, Z.B. Wang, X.P. Yong, K. Lu, Enhancing torsion fatigue behaviour of a martensitic stainless steel by generating gradient nanograined layer via surface mechanical grinding treatment, Mater. Sci. Technol. 29 (2013) 1200–1205.

[5] Z. Pu, S. Yang, G.L. Song, O.W. Dillon, D.A. Puleo, I.S. Jawahir, Ultrafine-grained surface layer on Mg-Al-Zn alloy produced by cryogenic burnishing for enhanced corrosion resistance, Scr. Mater. 65 (2011) 520–523.

[6] C. Saldana, T.G. Murthy, M.R. Shankar, E.A. Stach, S. Chandrasekar, Stabilizing nanostructured materials by coherent nanotwins and their grain boundary triple junction drag, Appl. Phys. Lett. 94 (2009) 021910.

[7] C. Saldana, A.H. King, E.A. Stach, W.D. Compton, S. Chandrasekar, Vacancies, twins, and the thermal stability of ultrafine-grained copper, Appl. Phys. Lett. 99 (2011) 231911.

[8] C. Saldana, A.H. King, S. Chandrasekar, Thermal stability and strength of deformation microstructures in pure copper, Acta Mater. 60 (2012) 4107–4116.

[9] R.Z. Valiev, T.G. Langdon, Principles of equal-channel angular pressing as a processing tool for grain refinement, Prog. Mater. Sci. 51 (2006) 881–981.

[10] K. Lu, Making strong nanomaterials ductile with gradients, Science (80-.). 345 (2014) 1455–1456.

[11] G. Cusanelli, A. Hessler-Wyser, F. Bobard, R. Demellayer, R. Perez, R. Flükiger, Microstructure at submicron scale of the white layer produced by EDM technique, J. Mater. Process. Technol. 149 (2004) 289–295.

[12] D. Trauth, F. Klocke, D. Welling, M. Terhorst, P. Mattfeld, A. Klink, Investigation of the surface integrity and fatigue strength of Inconel718 after wire EDM and machine hammer peening, Int. J. Mater. Form. 9 (2016) 635–651.

[13] X. Wu, P. Jiang, L. Chen, F. Yuan, Y.T. Zhu, Extraordinary strain hardening by gradient structure, Proc. Natl. Acad. Sci. 111 (2014) 7197–7201.

[14] J. Li, G.J. Weng, S. Chen, X. Wu, On strain hardening mechanism in gradient nanostructures, Int. J. Plast. 88 (2017).

[15] M.H. F.J. Humphreys, Recrystallization and related annealing phenomena, Elsevier, 1995.

[16] T.L. Brown, C. Saldana, T.G. Murthy, J.B. Mann, Y. Guo, L.F. Allard, A.H. King, W.D. Compton, K.P. Trumble, S. Chandrasekar, A study of the interactive effects of strain, strain rate and temperature in severe plastic deformation of copper, Acta Mater. 57 (2009) 5491–5500.

[17] H.W. Zhang, Z.K. Hei, G. Liu, J. Lu, K. Lu, Formation of nanostructured surface layer on AISI 304 stainless steel by means of surface mechanical attrition treatment, Acta Mater. 51 (2003) 1871–1881.

[18] K. Lu, J. Lu, Nanostructured surface layer on metallic materials induced by surface mechanical attrition treatment, Mater. Sci. Eng. A. 375–377 (2004) 38–45.

[19] N.R. Tao, Z.B. Wang, W.P. Tong, M.L. Sui, J. Lu, K. Lu, An investigation of surface nanocrystallization mechanism in Fe induced by surface mechanical attrition treatment, Acta Mater. 50 (2002) 4603–4616.

[20] Q. Liu, D. Juul Jensen, N. Hansen, Effect of grain orientation on deformation structure in cold-rolled polycrystalline aluminium, Acta Mater. 46 (1998) 5819–5838.

[21] M. Malaki, H. Ding, A review of ultrasonic peening treatment, Mater. Des. 87 (2015) 1072–1086.

[22] M. Qin, D.Y. Ju, R. Oba, Investigation of the influence of incidence angle on the process capability of water cavitation peening, Surf. Coatings Technol. 201 (2006) 1409–1413.

[23] W.L. Li, N.R. Tao, K. Lu, Fabrication of a gradient nano-micro-structured surface layer on bulk copper by means of a surface mechanical grinding treatment, Scr. Mater. 59 (2008) 546–549.

[24] T.S. Wang, J. Yang, C.J. Shang, X.Y. Li, B. Lv, M. Zhang, F.C. Zhang, Sliding friction surface microstructure and wear resistance of 9SiCr steel with low-temperature austempering treatment, Surf. Coatings Technol. 202 (2008) 4036–4040.

[25] P.S. Prevéy, J.T. Cammett, The influence of surface enhancement by low plasticity burnishing on the corrosion fatigue performance of AA7075-T6, Int. J. Fatigue. 26 (2004) 975–982.

[26] C.H.H. D. Y. Yang, A New Formulation of Generalized Velocity Field for Axisymmetric Forward Extrusion Through Arbitrarily Curved Dies, J. Eng. Ind. 109

(1987) 161–168.

[27] X.C. Liu, H.W. Zhang, K. Lu, Formation of nano-laminated structure in nickel by means of surface mechanical grinding treatment, Acta Mater. 96 (2015) 24–36.

[28] R.B. Figueiredo, I.P. Pinheiro, M.T.P. Aguilar, P.J. Modenesi, P.R. Cetlin, The finite element analysis of equal channel angular pressing (ECAP) considering the strain path dependence of the work hardening of metals, J. Mater. Process. Technol. 180 (2006) 30–36.

[29] J.Y. Huang, Y.T. Zhu, H. Jiang, T.C. Lowe, Microstructures and dislocation configurations in nanostructured Cu processed by repetitive corrugation and straightening, Acta Mater. 49 (2001) 1497–1505.

[30] H. Gleiter, Nanocrystalline materials, Prog. Mater. Sci. 33 (1989) 223–315.

[31] Y.M. Wang, K. Wang, D. Pan, K. Lu, K.J. Hemker, E. Ma, Microsample tensile testing of nanocrystalline copper, Scr. Mater. 48 (2003) 1581–1586.

[32] J.R. Weertman, Mechanical Behavior of Nanocrystalline Metals, in: Nanostructured Mater. Process. Prop. Appl. Second Ed., Elsevier, 2006: pp. 537–564.

[33] X. Wu, N. Tao, Y. Hong, B. Xu, J. Lu, K. Lu, Microstructure and evolution of mechanically-induced ultrafine grain in surface layer of AL-alloy subjected to USSP, Acta Mater. 50 (2002) 2075–2084.

[34] X. Wu, M. Yang, F. Yuan, G. Wu, Y. Wei, X. Huang, Y. Zhu, Heterogeneous lamella structure unites ultrafine-grain strength with coarse-grain ductility, Proc. Natl. Acad. Sci. 112 (2015) 14501–14505.

[35] C.C. Koch, Optimization of strength and ductility in nanocrystalline and ultrafine grained metals, Scr. Mater. 49 (2003) 657–662.

[36] H. Van Swygenhoven, Grain boundaries and dislocations, Science (80-.). 296 (2002) 66–67.

[37] J. Moering, X. Ma, J. Malkin, M. Yang, Y. Zhu, S. Mathaudhu, Synergetic strengthening far beyond rule of mixtures in gradient structured aluminum rod, Scr. Mater. 122 (2016) 106–109.

[38] Y. Wei, Y. Li, L. Zhu, Y. Liu, X. Lei, G. Wang, Y. Wu, Z. Mi, J. Liu, H. Wang, H. Gao, Evading the strength-ductility trade-off dilemma in steel through gradient hierarchical nanotwins, Nat. Commun. 5 (2014) 3580.

[39] E. Ma, T. Zhu, Towards strength–ductility synergy through the design of heterogeneous nanostructures in metals, Mater. Today. 20 (2017) 323–331.

[40] X.C. Liu, H.W. Zhang, K. Lu, Strain-induced ultrahard and ultrastable

nanolaminated structure in nickel, Science (80-.). 342 (2013) 337–340.

[41] X.L. Wu, P. Jiang, L. Chen, J.F. Zhang, F.P. Yuan, Y.T. Zhu, Synergetic strengthening by gradient structure, Mater. Res. Lett. 2 (2014) 185–191.

[42] M.F. Ashby, The deformation of plastically non-homogeneous materials, Philos. Mag. 21 (1970) 399–424.

[43] H. Gao, Y. Huang, Geometrically necessary dislocation and size-dependent plasticity, Scr. Mater. 48 (2003) 113–118.

[44] D.A. Hughes, N. Hansen, Microstructure and strength of nickel at large strains, Acta Mater. 48 (2000) 2985–3004.

[45] D.A. Hughes, Q. Liu, D.C. Chrzan, N. Hansen, Scaling of microstructural parameters: Misorientations of deformation induced boundaries, Acta Mater. 45 (1997) 105–112.

[46] D.A. Hughes, N. Hansen, D.J. Bammann, Geometrically necessary boundaries, incidental dislocation boundaries and geometrically necessary dislocations, Scr. Mater. 48 (2003) 147–153.

[47] S. Basu, M.R. Shankar, Spatial confinement-induced switchover in microstructure evolution during severe plastic deformation at micrometer length scales, Acta Mater. 79 (2014) 146–158.

[48] S. Basu, Z. Wang, R. Liu, C. Saldana, Enhanced subsurface grain refinement during transient shear-based surface generation, Acta Mater. 116 (2016) 114–123.

[49] D.R. Barraclough, C.M. Sellars, Static recrystallization and restoration after hot deformation of Type 304 stainless steel, Met. Sci. 13 (1979) 257–268.

[50] D.G. Cram, H.S. Zurob, Y.J.M. Brechet, C.R. Hutchinson, Modelling discontinuous dynamic recrystallization using a physically based model for nucleation, Acta Mater. 57 (2009) 5218–5228.

[51] R. Bhattacharya, B.P. Wynne, Hot working and crystallographic texture analysis of magnesium AZ alloys, Mater. Sci. Technol. 27 (2011) 461–477.

[52] U.F. Kocks, C.N. Tomé, H.-R. Wenk, Texture and Anisotropy: Preferred Orientations in Polycrystals and Their Effect on Materials Properties, Cambridge University Press, 2000.

[53] P. Paufler, W. F. Hosford. The mechanics of crystals and textured polycrystals. Oxford University Press, New York–Oxford 1993. 248 Seiten, Preis £ 30,–. ISBN 0-19-507744-X, Cryst. Res. Technol. 29 (1994) 532–532.

[54] C.F. Gu, L.S. Tóth, M. Arzaghi, C.H.J. Davies, Effect of strain path on grain

refinement in severely plastically deformed copper, Scr. Mater. 64 (2011) 284–287.

[55] I.J. Beyerlein, C.N. Tomé, Modeling transients in the mechanical response of copper due to strain path changes, Int. J. Plast. 23 (2007) 640–664.

[56] Y. Iwahashi, Z. Horita, M. Nemoto, T.G. Langdon, The process of grain refinement in equal-channel angular pressing, Acta Mater. 46 (1998) 3317–3331.

[57] S. Basu, M. Ravi Shankar, Crystallographic Textures Resulting from Severe Shear Deformation in Machining, Metall. Mater. Trans. A Phys. Metall. Mater. Sci. 46 (2014) 801–812.

[58] Y.S. Zhang, Z. Han, K. Wang, K. Lu, Friction and wear behaviors of nanocrystalline surface layer of pure copper, Wear. 260 (2006) 942–948.

[59] T. Roland, D. Retraint, K. Lu, J. Lu, Fatigue life improvement through surface nanostructuring of stainless steel by means of surface mechanical attrition treatment, Scr. Mater. 54 (2006) 1949–1954.

[60] R.K. Dutta, L. Malet, H. Gao, M.J.M. Hermans, S. Godet, I.M. Richardson, Formation of Nanostructures in Severely Deformed High-Strength Steel Induced by High-Frequency Ultrasonic Impact Treatment, Metall. Mater. Trans. A Phys. Metall. Mater. Sci. 46 (2014) 813–830.

[61] K. Wang, N.R. Tao, G. Liu, J. Lu, K. Lu, Plastic strain-induced grain refinement at nanometer scale in copper, Acta Mater. 54 (2006) 5281–5291.

[62] V. Lemiale, Y. Estrin, H.S. Kim, R. O'Donnell, Forming nanocrystalline structures in metal particle impact, Metall. Mater. Trans. A Phys. Metall. Mater. Sci. 42 (2011) 3006–3012.

[63] A. Gholinia, P. Bate, P.B. Prangnell, Modelling texture development during equal channel angular extrusion of aluminium, Acta Mater. 50 (2002) 2121–2136.

[64] M. Kawasaki, B. Ahn, T.G. Langdon, Microstructural evolution in a two-phase alloy processed by high-pressure torsion, Acta Mater. 58 (2010) 919–930.

[65] M.E. Merchant, Mechanics of the metal cutting process. I. Orthogonal cutting and a type 2 chip, J. Appl. Phys. 16 (1945) 267–275.

[66] H.A. Bruck, S.R. McNeill, M.A. Sutton, W.H. Peters, Digital image correlation using Newton-Raphson method of partial differential correction, Exp. Mech. 29 (1989) 261–267.

[67] J. Westerweel, Fundamentals of digital particle image velocimetry, Meas. Sci. Technol. 8 (1997) 1379–1392.

[68] M. Raffel, C.E. Willert, S.T. Wereley, J. Kompenhans, Post-Processing of PIV Data,

in: Part. Image Velocim., Springer International Publishing, Cham, 2018: pp. 177–208.

[69] B. Pan, K. Qian, H. Xie, A. Asundi, Two-dimensional digital image correlation for in-plane displacement and strain measurement: A review, Meas. Sci. Technol. 20 (2009) 062001.

[70] S. Li, I.J. Beyerlein, C.T. Necker, D.J. Alexander, M. Bourke, Heterogeneity of deformation texture in equal channel angular extrusion of copper, Acta Mater. 52 (2004) 4859–4875.

[71] A.A. Gazder, S. Li, F.H. Dalla Torre, I.J. Beyerlein, C.F. Gu, C.H.J. Davies, E. V. Pereloma, Progressive texture evolution during equal channel angular extrusion, Mater. Sci. Eng. A. 437 (2006) 259–267.

[72] R.A. Lebensohn, C.N. Tomé, A self-consistent anisotropic approach for the simulation of plastic deformation and texture development of polycrystals: Application to zirconium alloys, Acta Metall. Mater. 41 (1993) 2611–2624.

[73] M.C. Shaw, G.J. DeSalvo, On the Plastic Flow Beneath a Blunt Axisymmetric Indenter, J. Eng. Ind. 92 (1970) 480.

[74] M.M. Chaudhri, Strain hardening around spherical indentations, Phys. Status Solidi Appl. Res. 182 (2000) 641–652.

[75] R. Vaidyanathan, M. Dao, G. Ravichandran, S. Suresh, Study of mechanical deformation in bulk metallic glass through instrumented indentation, Acta Mater. 49 (2001) 3781–3789.

[76] T.G. Murthy, C. Huang, S. Chandrasekar, Characterization of deformation field in plane-strain indentation of metals, J. Phys. D. Appl. Phys. 41 (2008) 074026.

[77] N. Sundaram, Y. Guo, T.G. Murthy, C. Saldana, S. Chandrasekar, Rotation field in wedge indentation of metals, J. Mater. Res. 27 (2012) 284–293.

[78] W. Yu, J.P. Blanchard, An elastic-plastic indentation model and its solutions, J. Mater. Res. 11 (1996) 2358–2367.

[79] K.L. Johnson, The correlation of indentation experiments, J. Mech. Phys. Solids. 18 (1970) 115–126.

[80] X.L. Gao, An expanding cavity model incorporating strain-hardening and indentation size effects, Int. J. Solids Struct. 43 (2006) 6615–6629.

[81] L.E. Samuels, T.O. Mulhearn, An experimental investigation of the deformed zone associated with indentation hardness impressions, J. Mech. Phys. Solids. 5 (1957) 125–134.

[82] R. Hill, E.H. Lee, S.J. Tupper, The Theory of Wedge Indentation of Ductile Materials, Proc. R. Soc. A Math. Phys. Eng. Sci. 188 (1947) 273–289.

[83] Rodney Hill, The mathematical Theory of Plasticity, Oxford university press, 1950.

[84] S.K. Kang, Y.C. Kim, K.H. Kim, J.Y. Kim, D. Kwon, Extended expanding cavity model for measurement of flow properties using instrumented spherical indentation, Int. J. Plast. 49 (2013) 1–15.

[85] M. Mata, O. Casals, J. Alcalá, The plastic zone size in indentation experiments: The analogy with the expansion of a spherical cavity, Int. J. Solids Struct. 43 (2006) 5994–6013.

[86] S. Yadav, C. Saldana, T.G. Murthy, Deformation field evolution in indentation of a porous brittle solid, Int. J. Solids Struct. 66 (2015) 35–45.

[87] K. Ai, L.H. Dai, A new modified expanding cavity model for characterizing the spherical indentation behavior of bulk metallic glass with pile-up, Scr. Mater. 56 (2007) 761–764.

[88] R. Narasimhan, Analysis of indentation of pressure sensitive plastic solids using the expanding cavity model, Mech. Mater. 36 (2004) 633–645.

[89] X. Hernot, O. Bartier, An expanding cavity model incorporating pile-up and sink-in effects, J. Mater. Res. 27 (2012) 132–140.

[90] P. Jiang, T. Zhang, Y. Feng, R. Yang, N. Liang, Determination of plastic properties by instrumented spherical indentation: Expanding cavity modei and similarity solution approach, J. Mater. Res. 24 (2009) 1045–1053.

[91] M.A. Meyers, G. Subhash, B.K. Kad, L. Prasad, Evolution of microstructure and shear-band formation in α-hcp titanium, Mech. Mater. 17 (1994) 175–193.

[92] S. Pathak, S.R. Kalidindi, Spherical nanoindentation stress-strain curves, Mater. Sci. Eng. R Reports. 91 (2015) 1–36.

[93] X.L. Gao, X.N. Jing, G. Subhash, Two new expanding cavity models for indentation deformations of elastic strain-hardening materials, Int. J. Solids Struct. 43 (2006) 2193–2208.

[94] R. Sánchez-Martín, M.T. Pérez-Prado, J. Segurado, J. Bohlen, I. Gutiérrez-Urrutia, J. Llorca, J.M. Molina-Aldareguia, Measuring the critical resolved shear stresses in Mg alloys by instrumented nanoindentation, Acta Mater. 71 (2014) 283–292.

[95] C. Zambaldi, Y. Yang, T.R. Bieler, D. Raabe, Orientation informed nanoindentation of α-titanium: Indentation pileup in hexagonal metals deforming by prismatic slip, J. Mater. Res. 27 (2012) 356–367.

[96] Y. Wang, D. Raabe, C. Klüber, F. Roters, Orientation dependence of nanoindentation pile-up patterns and of nanoindentation microtextures in copper single crystals, Acta Mater. 52 (2004) 2229–2238.

[97] A. Yonezu, Y. Kuwahara, K. Yoneda, H. Hirakata, K. Minoshima, Estimation of the anisotropic plastic property using single spherical indentation-An FEM study, Comput. Mater. Sci. 47 (2009) 611–619.

[98] M. Mata, J. Alcalá, The role of friction on sharp indentation, J. Mech. Phys. Solids. 52 (2004) 145–165.

[99] D. Raabe, Y. Wang, F. Roters, Crystal plasticity simulation study on the influence of texture on earing in steel, Comput. Mater. Sci. 34 (2005) 221–234.

[100] J. Bohlen, M.R. Nürnberg, J.W. Senn, D. Letzig, S.R. Agnew, The texture and anisotropy of magnesium-zinc-rare earth alloy sheets, Acta Mater. 55 (2007) 2101–2112.

[101] A.B. Lopes, F. Barlat, J.J. Gracio, J.F. Ferreira Duarte, E.F. Rauch, Effect of texture and microstructure on strain hardening anisotropy for aluminum deformed in uniaxial tension and simple shear, Int. J. Plast. 19 (2003) 1–22.

[102] C.A. Bronkhorst, S.R. Kalidindi, L. Anand, Polycrystalline Plasticity and the Evolution of Crystallographic Texture in FCC Metals, Philos. Trans. R. Soc. A Math. Phys. Eng. Sci. 341 (1992) 443–477.

[103] A. Bolshakov, G.M. Pharr, Influences of pileup on the measurement of mechanical properties by load and depth sensing indentation techniques, J. Mater. Res. 13 (1998) 1049–1058.

[104] W. Johnson, Some slip-line fields for swaging or expanding, indenting, extruding and machining for tools with curved dies, Int. J. Mech. Sci. 4 (1962) 323–347.

[105] T.G. Murthy, C. Saldana, M. Hudspeth, R. M'Saoubi, Deformation field heterogeneity in punch indentation, Proc. R. Soc. A Math. Phys. Eng. Sci. 470 (2014) 20130807–20130807.

[106] Z. Wang, S. Basu, T.G. Murthy, C. Saldana, Modified cavity expansion formulation for circular indentation and experimental validation, Int. J. Solids Struct. 97–98 (2016) 129–136.

[107] N.A. Fleck, G.M. Muller, M.F. Ashby, J.W. Hutchinson, Strain gradient plasticity: Theory and experiment, Acta Metall. Mater. 42 (1994) 475–487.

[108] S. Abolghasem, S. Basu, M.R. Shankar, Quantifying the progression of dynamic recrystallization in severe shear deformation at high strain rates, J. Mater. Res. 28 (2013) 2056–2069.

[109] S. Abolghasem, S. Basu, S. Shekhar, J. Cai, M.R. Shankar, Mapping subgrain sizes resulting from severe simple shear deformation, Acta Mater. 60 (2012) 376–386.

[110] A. Mishra, B.K. Kad, F. Gregori, M.A. Meyers, Microstructural evolution in copper subjected to severe plastic deformation: Experiments and analysis, Acta Mater. 55 (2007) 13–28.

[111] A. Mahato, Y. Guo, N.K. Sundaram, S. Chandrasekar, Surface folding in metals: a mechanism for delamination wear in sliding, Proc. R. Soc. A Math. Phys. Eng. Sci. 470 (2014) 20140297–20140297.

[112] N.K. Sundaram, Y. Guo, S. Chandrasekar, Mesoscale folding, instability, and disruption of laminar flow in metal surfaces, Phys. Rev. Lett. 109 (2012).

[113] T. Miura, K. Fujii, K. Fukuya, K. Takashima, Influence of crystal orientation on hardness and nanoindentation deformation in ion-irradiated stainless steels, J. Nucl. Mater. 417 (2011) 984–987.

[114] L.L. Shaw, J.W. Tian, A.L. Ortiz, K. Dai, J.C. Villegas, P.K. Liaw, R. Ren, D.L. Klarstrom, A direct comparison in the fatigue resistance enhanced by surface severe plastic deformation and shot peening in a C-2000 superalloy, Mater. Sci. Eng. A. 527 (2010) 986–994.

[115] B.N. Mordyuk, O.P. Karasevskaya, G.I. Prokopenko, N.I. Khripta, Ultrafine-grained textured surface layer on Zr-1%Nb alloy produced by ultrasonic impact peening for enhanced corrosion resistance, Surf. Coatings Technol. 210 (2012) 54–61.

[116] N.R. Tao, M.L. Sui, J. Lu, K. Lua, Surface nanocrystallization of iron induced by ultrasonic shot peening, Nanostructured Mater. 11 (1999) 433–440.

[117] H.L. Chan, H.H. Ruan, A.Y. Chen, J. Lu, Optimization of the strain rate to achieve exceptional mechanical properties of 304 stainless steel using high speed ultrasonic surface mechanical attrition treatment, Acta Mater. 58 (2010) 5086–5096.

[118] X. Dai, J. Boll, M.E. Hayes, D.E. Aston, Adhesion of Cryptosporidium parvum and Giardia lamblia to solid surfaces: The role of surface charge and hydrophobicity, Colloids Surfaces B Biointerfaces. 34 (2004) 259–263.

[119] C. Bernal, A.M. Camacho, J.M. Arenas, E.M. Rubio Alvir, Analytical Procedure for Geometrical Evaluation of Flat Surfaces Formed by Multiple Indentation Processes, Appl. Mech. Mater. 217–219 (2012) 2351–2356.

[120] S. Bagherifard, R. Ghelichi, M. Guagliano, A numerical model of severe shot peening (SSP) to predict the generation of a nanostructured surface layer of material, Surf. Coatings Technol. 204 (2010) 4081–4090.

[121] L.E. Samuels, T.O. Mulhearn, An experimental investigation of the deformed zone

associated with indentation hardness impressions, J. Mech. Phys. Solids. 5 (1957) 125–134.

[122] S.A. Meguid, M.S. Klair, An examination of the relevance of co-indentation studies to incomplete coverage in shot-peening using the finite-element method, J. Mech. Work. Technol. 11 (1985) 87–104.

[123] S.A. Meguid, G. Shagal, J.C. Stranart, 3D FE analysis of peening of strain-rate sensitive materials using multiple impingement model, Int. J. Impact Eng. 27 (2002) 119–134.

[124] G.H. Majzoobi, R. Azizi, A. Alavi Nia, A three-dimensional simulation of shot peening process using multiple shot impacts, J. Mater. Process. Technol. 164–165 (2005) 1226–1234.

[125] C. Bernal, A.M. Camacho, M.M. Marín, B. de Agustina, Methodology for the evaluation of 3D surface topography in multiple indentation processes, Int. J. Adv. Manuf. Technol. 69 (2013) 2091–2098.

[126] S. Basu, Z. Wang, C. Saldana, Deformation heterogeneity and texture in surface severe plastic deformation of copper, Proc. R. Soc. London A Math. Phys. Eng. Sci. 472 (2016) 20150486.

[127] Z. Wang, S. Basu, T.G. Murthy, C. Saldana, ARTICLE Gradient microstructure and texture in wedge-based severe plastic burnishing of copper, (2018).

[128] G.H. Farrahi, J.L. Lebrijn, D. Couratin, Effect of Shot Peening on Residual Stress and Fatigue Life of a Spring Steel, Fatigue Fract. Eng. Mater. Struct. 18 (1995) 211–220.

[129] C. Guo, Z. Wang, D. Wang, S. Hu, Numerical analysis of the residual stress in ultrasonic impact treatment process with single-impact and two-impact models, Appl. Surf. Sci. 347 (2015) 596–601.

[130] S. Bagherifard, I. Fernandez-Pariente, R. Ghelichi, M. Guagliano, Effect of severe shot peening on microstructure and fatigue strength of cast iron, Int. J. Fatigue. 65 (2014) 64–70.

[131] G.M. Pharr, An improved technique for determining hardness and elastic modulus using load and displacement sensing indentation experiments, J. Mater. Res. 7 (1992) 1564–1583.

[132] S. Basu, Z. Wang, C. Saldana, Anomalous evolution of microstructure and crystallographic texture during indentation, Acta Mater. 105 (2016) 25–34.

[133] Y. Guo, C. Saldana, W. Dale Compton, S. Chandrasekar, Controlling deformation and microstructure on machined surfaces, Acta Mater. 59 (2011) 4538–4547.

[134] S. Shekhar, S. Abolghasem, S. Basu, J. Cai, M.R. Shankar, Effect of Severe Plastic Deformation in Machining Elucidated via Rate-Strain-Microstructure Mappings, J. Manuf. Sci. Eng. 134 (2012) 031008.

[135] E. Nes, Modelling of work hardening and stress saturation in FCC metals, Prog. Mater. Sci. 41 (1997) 129–193.

[136] S.Q. Deng, A. Godfrey, W. Liu, N. Hansen, A gradient nanostructure generated in pure copper by platen friction sliding deformation, Scr. Mater. 117 (2016) 41–45.

[137] Y. Guo, W.D. Compton, S. Chandrasekar, In situ analysis of flow dynamics and deformation fields in cutting and sliding of metals, Proc. R. Soc. A Math. Phys. Eng. Sci. 471 (2015) 20150194–20150194.

[138] S. Li, Comments on "Texture evolution by shear on two planes during ECAP of a high-strength aluminum alloy," Scr. Mater. 60 (2009) 356–358.

[139] I.J. Beyerlein, L.S. Tóth, Texture evolution in equal-channel angular extrusion, Prog. Mater. Sci. 54 (2009) 427–510.

[140] D. Sagapuram, M. Efe, W. Moscoso, S. Chandrasekar, K.P. Trumble, Controlling texture in magnesium alloy sheet by shear-based deformation processing, Acta Mater. 61 (2013) 6843–6856.

[141] N. Fang, Tool-chip friction in machining with a large negative rake angle tool, Wear. 258 (2005) 890–897.

[142] W. Polkowski, P. Jóźwik, M. Polański, Z. Bojar, Microstructure and texture evolution of copper processed by differential speed rolling with various speed asymmetry coefficient, Mater. Sci. Eng. A. 564 (2013) 289–297.

[143] W.N. Findley, R.M. Reed, The influence of extreme speeds and rake angles in metal cutting, Trans. ASME J. Engng Indust. 85 (1963) 49–67.

[144] W.H. Huang, L. Chang, P.W. Kao, C.P. Chang, Effect of die angle on deformation texture of copper processed by equal channel angular extrussion, Mater. Sci. Eng. A. 307 (2001) 113–118.

[145] H. Beladi, P. Cizek, P.D. Hodgson, Dynamic recrystallization of austenite in Ni-30 Pct Fe model alloy: Microstructure and texture evolution, Metall. Mater. Trans. A Phys. Metall. Mater. Sci. 40 (2009) 1175–1189.

[146] R. Hielscher, H. Schaeben, A novel pole figure inversion method: Specification of the MTEX algorithm, J. Appl. Crystallogr. 41 (2008) 1024–1037.

[147] P. Guo, K.F. Ehmann, An analysis of the surface generation mechanics of the elliptical vibration texturing process, Int. J. Mach. Tools Manuf. 64 (2013) 85–95.

[148] Z. Wang, S. Basu, T.G. Murthy, C. Saldana, Gradient microstructure and texture in wedge-based severe plastic burnishing of copper, J. Mater. Res. 33 (2018) 1046–1056.

[149] Z. Wang, S. Basu, C. Saldana, Understanding gradient nanostructure on the surface processed by dry orthogonal sliding process, in: Proc. ASME Manuf. Sci. Eng. Conf., 2017.

[150] S. Basu, Z. Wang, C. Saldana, Modeling evolution of microstructures beneath topographically textured surfaces produced using shear-based material removal, in: Proc. ASME Manuf. Sci. Eng. Conf., 2016.

[151] S. Basu, Z. Wang, C. Saldana, Crystallographic textures produced during sand blasting, in: Proc. ASME Manuf. Sci. Eng. Conf., 2015.

[152] Z. Wang, S. Basu, C. Saldana, Subsurface Deformation in Surface Mechanical Attrition Processes, in: Vol. 2 Mater. Biomanufacturing; Prop. Appl. Syst. Sustain. Manuf., ASME, 2015: p. V002T01A013.

[153] Z. Wang, S. Basu, C. Saldana, Quantifying the spread in crystallographic textures due to transients in strain path, Under Rev. (2018).

[154] Z. Wang, T.G. Murthy, C. Saldana, Deformation field in sequential circular indentation of a strain hardening material, Under Rev. (2018).

[155] Z. Wang, T.G. Murthy, C. Saldana, Graded microstructure in deformation by sequential circular indentation, Under Prep. (2018).